Atomic Layer Deposition of 2D Metal Dichalcogenides for Electronics, Catalysis, Energy Storage, and Beyond

Mattinen, Miika

2021-03

unspecified
acceptedVersion

Atomic Layer Deposition of Two-Dimensional Metal Dichalcogenides for Electronics, Catalysis, Energy Storage, and Beyond

Miika Mattinen, Markku Leskelä, Mikko Ritala*

Dr. M. Mattinen, Prof. M. Leskelä, Prof. M. Ritala
Department of Chemistry, University of Helsinki, P.O. Box 55, FI-00014, Finland
E-mail: mikko.ritala@helsinki.fi

Two-dimensional transition metal dichalcogenides (TMDCs) are among the most exciting materials of today. Their layered crystal structures result in unique and useful electronic, optical, catalytic, and quantum properties. To realize the technological potential of TMDCs, methods depositing uniform films of controlled thickness at low temperatures in a highly controllable, scalable, and repeatable manner are needed. Atomic layer deposition (ALD) is a chemical gas-phase thin film deposition method capable of meeting these challenges. In this review, the applications evaluated for ALD TMDCs are systematically examined, including electronics and optoelectonics, electrocatalysis and photocatalysis, energy storage, lubrication, plasmonics, solar cells, and photonics. The review focuses on understanding the interplay between ALD precursors and deposition conditions, the resulting film characteristics such as thickness, crystallinity, and morphology, and ultimately device performance. Through rational choice of precursors and conditions, ALD is observed to exhibit potential to meet the varying requirements of widely different applications. Beyond the current state of ALD TMDCs, the future prospects, opportunities, and challenges in different applications are discussed. The authors hope that the review aids in bringing together experts in the fields of ALD, TMDCs, and various applications to eventually realize industrial applications of ALD TMDCs.

1. Introduction

Two-dimensional (2D) materials have rapidly emerged from obscurity to some of the most actively studied materials within the last 15 years, although their history spans much longer. The layered crystal structure of transition metal dichalcogenides (TMDCs), a prominent group of 2D materials, was solved[1] in 1923 for naturally occurring semiconducting MoS_2, which then gained industrial applications as a lubricant[2,3] and hydrodesulfurization (HDS) catalyst[4] in the following decades. Most of the presently known TMDCs were found and characterized by 1960s in their bulk form.[5,6] TMDC TiS_2 was the cathode material in the first commercial rechargeable lithium batteries in the 1970s,[7] although it was soon replaced by other materials. Research on the fundamental properties and preparation of TMDC monolayers in solution (1986),[8] on single-crystal substrates in ultra-high vacuum (2001),[9] and in an accessible way using mechanical exfoliation[10] (2005) followed.

It was the discovery of graphene in 2004[11] with its ever expanding list of unique and exciting properties, phenomena, and potential applications[12] that amassed broad attention to 2D materials and resulted in the 2010 Nobel Prize in Physics awarded to Andre Geim and Konstantin Novoselov. Tremendous efforts have been put towards synthesis and applications of graphene, including the billion euro Graphene Flagship project funded by the European Union.[13,14] Graphene is a semimetal, however, and the need to have semiconducting materials for many crucial applications, in particular in electronics, has led researchers to search for other 2D materials.

The scientific community turned to TMDCs following breakthroughs in observation of unique thickness-dependent properties,[15,16] monolayer synthesis using chemical vapor deposition (CVD),[17,18] and demonstration of high-performance semiconductor devices[19–21] in 2010–2013 (**Figure 1**). Indeed, in 2013 the number of scientific publications on TMDCs, in particular MoS_2, nearly tripled over 2012, and the strong growth has continued to date, fueled by advances in synthesis, new devices, and exciting physical phenomena. The explosive growth in MoS_2

research has also expanded to other TMDCs,[22] resulting in yet new phenomena and potential

applications being found.[23–26]
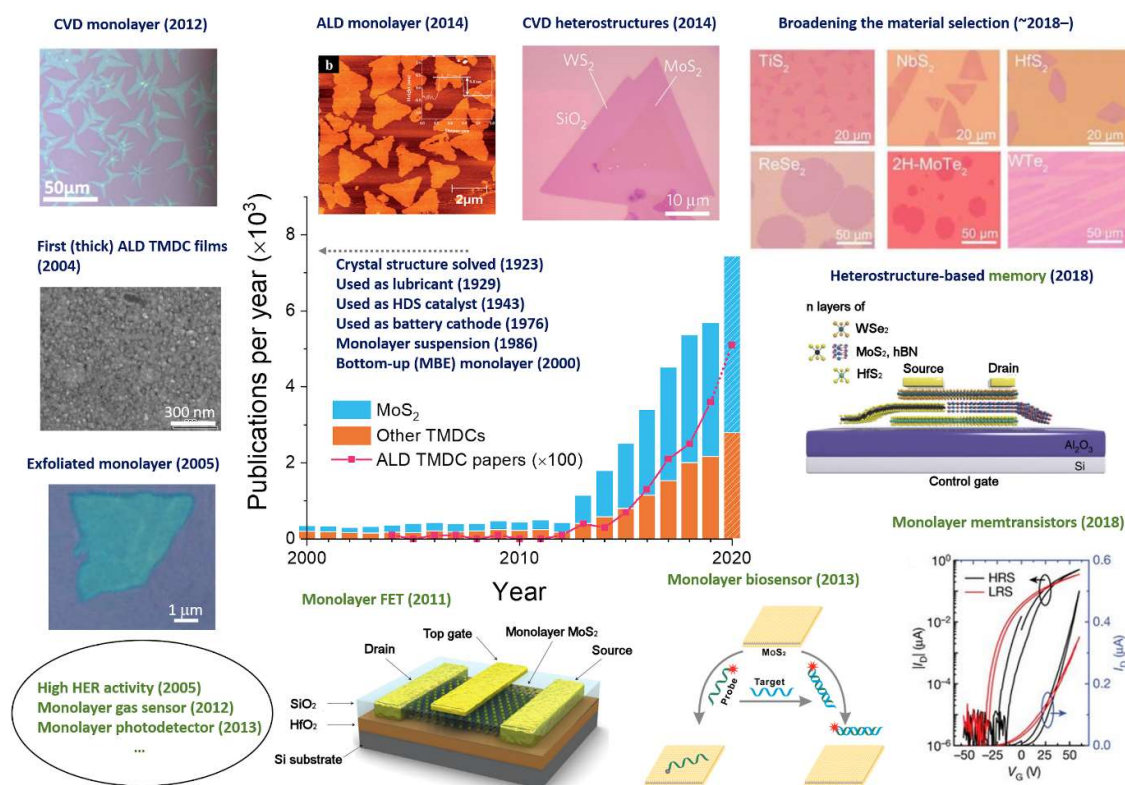
Figure 1. Evolution of TMDC publications from 2000 to 2020 and selected highlights in synthesis (dark blue) and applications (green). All of the values for 2020 are extrapolated (linearly) for the full year based on the numbers obtained on 29 April 2020. The MoS₂ (TITLE-ABS-KEY: MoS₂ AND molybdenum disulfide) and TMDC (similar search including all layered TMDCs according to definition of Figure 2) numbers were searched using Scopus. The numbers of ALD TMDC publications (multiplied by a factor of 100) are from Table 2 and 3. References: Crystal structure solved,[1] used as lubricant,[2,3] used as HDS catalyst,[4] used as battery cathode,[7] monolayer suspension,[8] bottom-up (MBE, molecular beam epitaxy) monolayer,[9] high hydrogen evolution reaction (HER) activity,[27] monolayer gas sensor,[21] and monolayer photodetector.[20] Figures reproduced (adapted) with permission. Exfoliated monolayer:[10] Copyright 2005, National Academy of Sciences. First ALD TMDC films:[28] Copyright 2004, Cambridge University Press. CVD Monolayer:[17] Copyright 2012, WILEY-VCH Verlag GmbH. ALD monolayer:[29] Copyright 2014, The Royal Society of Chemistry. CVD heterostructures:[30] Copyright 2014, Macmillan Publishers Limited, part of Springer Nature. Broadening the material selection:[22] Copyright 2018, Macmillan Publishers Limited, part of Springer Nature. Heterostructure-based memory:[31] Copyright 2018, Macmillan Publishers Limited, part of Springer Nature. Monolayer memtransistors:[32] Copyright 2018, Macmillan Publishers Limited, part of Springer Nature. Monolayer biosensor:[33] Copyright 2013, American Chemical Society. Monolayer field-effect transistor (FET):[19] Copyright 2011, Macmillan Publishers Limited, part of Springer Nature.

It is now clear that TMDCs are remarkable in many ways. Their layered crystal structure gives rise to fundamental physics not seen in three-dimensional (3D) materials, which enables novel devices and applications.[25,26,32,34–36] The layered structure also gives TMDCs their highly anisotropic properties, extremely high specific surface areas, possibility to intercalate different species between the layers, and stability as ultrathin sheets down to three atomic layers thick. The TMDC family contains dozens of different materials from semiconductors to semimetals, metals, and even superconductors.[5,22,25,34]

However, TMDC research is still mostly in the early discovery stages and the investigations of TMDCs largely continue using flakes produced by mechanical exfoliation of bulk crystals.[10,26] Unfortunately, this method cannot be scaled up for practical applications. Therefore, it is imperative to focus on techniques that can be used to deposit TMDC films of controllable thickness on large areas as well as complex (nano)structures. Preparation of TMDCs at reasonable cost requires deposition methods that are scalable, repeatable, and integrable into production lines. Despite major improvements in CVD, including deposition of wafer-scale monolayers using metal-organic CVD (MOCVD)[37,38] and controlled preparation of heterostructures,[30,39] higher quality, increased control, and milder synthesis conditions still need to be achieved for large-scale applications.

Atomic layer deposition (ALD) is an advanced method used for deposition of thin films of various materials from gas phase precursors in a very controllable manner.[40–43] ALD has been used in industrial production since the early 1980s and in the last two decades many new industrial applications of ALD have emerged in different fields.[44–46] ALD is now one of the leading thin film deposition techniques and has potential to enable industrial production of 2D materials. The first example of a TMDC ALD process dates to 2004,[28] although in that case only thick WS_2 films were examined. Research on ultrathin ALD TMDCs began in 2014,[29] and a few years later started to expand rapidly. At present, ALD of TMDCs is a very active and rapidly growing field of research.

Deposition of TMDCs by ALD and their optoelectronic applications reported up to November 2018 have been reviewed by the authors.[47] Furthermore, Hao et al.[48] have provided an extensive review on ALD of 2D materials up to early 2018, whereas Huang et al.[49] have reviewed deposition of MoS_2 by ALD. In early 2020, Cai et al.[50] published another broad review concerning deposition of 2D materials by ALD. The reader is referred to these reviews for more detailed discussion on the ALD processes of 2D materials. In this review, we focus on the application potential of the ALD TMDCs that has not yet been reviewed and emphasize the connection between deposition chemistry, film properties, and performance in applications. Due to the high activity in the rapidly advancing field of ALD TMDCs, a comprehensive table on ALD processes of TMDCs up to August 2020 is also provided.

The review begins with a brief introduction to the TMDC family including their structures and properties in Section 2. The concept of ALD is introduced in Section 3.1. We then discuss specialties in applying ALD to 2D materials in Section 3.2, followed by evaluation of the main strengths and challenges of ALD and its comparison to other TMDC deposition methods in Section 3.3. In Section 3.4, deposition chemistry of ALD TMDCs is briefly discussed with comprehensive tables provided. In Section 4, we discuss the evaluated applications of ALD TMDCs. The applications are divided into electronics and optoelectronics (Section 4.1), electrocatalysis and photocatalysis (Section 4.2), energy storage (Section 4.3), and other applications (Section 4.4). The performance of ALD TMDCs in the most actively studied applications is tabulated in each section for easy reference and comparison. We identify the suitability of different thicknesses and levels of crystalline quality resulting from the use of different precursors and deposition conditions for different applications. Throughout the section, the performance of ALD TMDCs is compared to the TMDC literature and opportunities and challenges for ALD in different applications are discussed. Finally, in Section 5, we summarize the most important observations and general trends to date and discuss future outlook and possible new areas for ALD TMDCs.

2. The Two-Dimensional Metal Dichalcogenide Family

The TMDC family contains some 70 unique MX_2 (M = transition metal or Sn; X = S, Se, Te) compositions, of which approximately half have a layered structure (**Figure 2**a,b).[5,25,34] The layered TMDCs form infinite chalcogen-metal-chalcogen layers that are held together with covalent bonds. One such three-atom (~6 Å) thick unit is commonly denoted a monolayer (ML). There are only weak van der Waals (vdW) forces between two MLs and the space between them is commonly called a vdW gap. Although ALD studies have so far focused on only a handful of TMDCs (marked in Figure 2b), we give a brief overview of all 2D TMDCs in this section in hopes to stimulate ALD studies on a broader selection of TMDC materials.
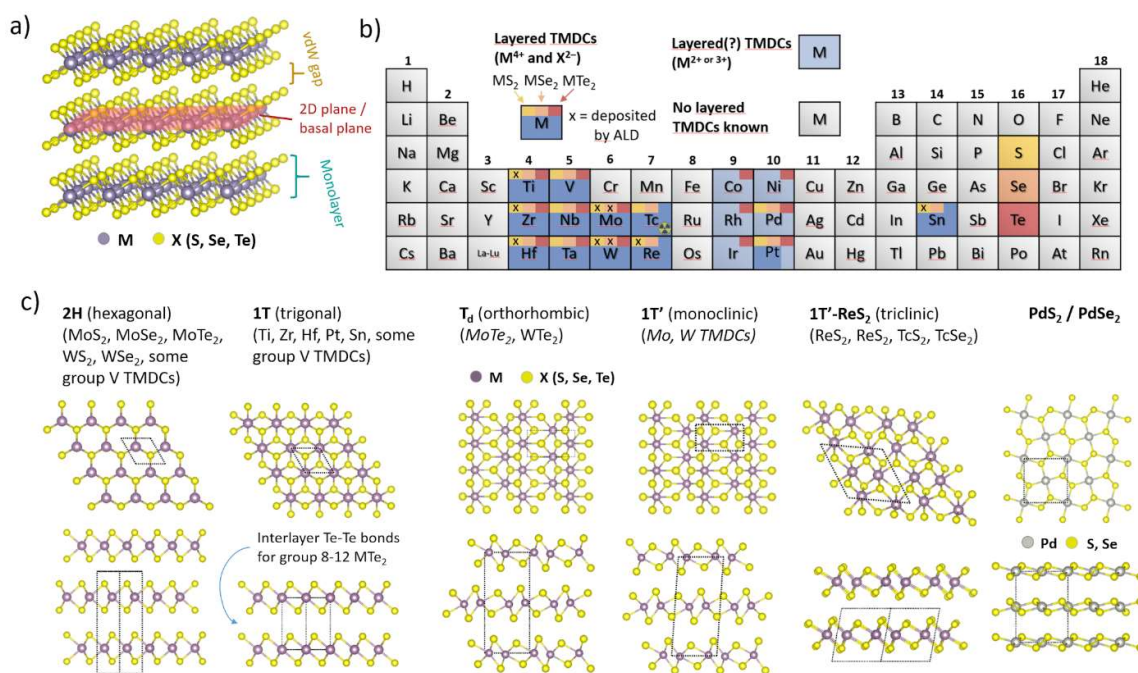
Figure 2. a) Layered structure of TMDCs exemplified by the 1T phase and terminology used to describe the structure. b) Periodic table highlighting metals that form layered TMDCs (MS_2, MSe_2, and MTe_2 in different colors). Dark blue shading corresponds to metals forming typical layered TMDCs with M^{4+} and X^{2-} ions, while light blue corresponds to partially layered structures containing M^{2+} or M^{3+} ions. TMDCs deposited by ALD are marked with an x. c) Top (top row) and side (bottom row) views of crystal structures of the different TMDC phases and examples of materials crystallizing in each structure. Metastable phases are written in *italic*. The structures were drawn with VESTA[51] using data from the Inorganic Crystal Structure Database.[52]

First of all, although all of the transition metals from groups 4 to 10 and even some group 11 (Cu) and 12 (Zn, Cd) metals form MX_2 compounds (X = S, Se, Te),[5,53] not all of them are layered (2D). The metals shaded blue (a main group metal Sn is also included as it forms similar layered compounds) in Figure 2b form "typical" layered TMDCs with oxidation states of the metal and chalcogen ions of +4 and –2, respectively. PdS_2 and $PdSe_2$ crystallize in an orthorhombic layered structure containing Pd^{2+} and S_2^{2-} ions that is very different to all other TMDCs (Figure 2c).[54] The ditellurides of the late transition metals (shaded light blue) exhibit some Te-Te bonding between the layers due to the average M and Te oxidation states ranging from +2 to +3 and –1 to –1.5, respectively.[53] Therefore, these ditellurides can be considered borderline 2D/3D materials. To the best of our knowledge, TMDCs not shaded in Figure 2b crystallize in three-dimensional structures.[5,6,55]

TMDCs can crystallize in a variety of related layered structures (Figure 2c). The most common TMDC phases are the hexagonal 2H phase with trigonal prismatic coordination, and the trigonal 1T phase with octahedral coordination around the metal. Distorted variants of the 1T structure include the monoclinic, orthorhombic, and triclinic phases, which are here denoted 1T', T_d, and 1T'-ReS_2, respectively. Unfortunately, in the literature all of these are often denoted 1T'. Different stacking arrangements (polytypes), such as the rhombohedral 3R phase can also form – although obviously only in films thicker than a single ML.

Electronically, TMDCs exhibit diverse characteristics. Group 4 sulfides and selenides that crystallize in the 1T phase are semiconducting,[56,57] with a possible exception of TiS_2, the nature of which is still debated in the literature.[58] Group 4 tellurides (1T) and all group 5 TMDCs are metallic or semimetallic.[36,56,59,60] Group 5 sulfides and selenides exhibit either the 1T, 2H, or 3R phases depending on the metal and preparation conditions, whereas the group 5 tellurides usually adopt the the 1T' phase.[36,60,61] Many of the group 5 TMDCs also exhibit special charge density wave (CDW) phases,[36,60] and some are superconducting at relatively low temperatures (<10 K).[36]

Group 6 TMDCs (excluding WTe$_2$) in the thermodynamically stable 2H phase are semiconducting with indirect (optical) band gaps of 1.1–1.4 eV in bulk form and direct band gaps of 1.6–2.0 eV as monolayers.[16,25,26,62] In contrast, their metastable 1T' phases are (semi)metallic (the often claimed 1T phase tends to spontaneously transform to 1T').[25,26,63,64] The stable T$_d$-WTe$_2$ has been suggested to be a topological semimetal.[65] The triclinic 1T'-ReS$_2$ structure is characteristic to the semiconducting disulfides and diselenides of group 7 elements Re and radioactive Tc.[66,67] PtS$_2$, PtSe$_2$, SnS$_2$, and SnSe$_2$ crystallize in the 1T phase and are semiconducting in bulk except for the semimetallic PtSe$_2$.[25,56,68,69] A more detailed survey of the properties of different TMDC materials and phases can be found in Ref. [70]

Thickness or the number of MLs affects the properties of TMDCs, especially at thicknesses below 5 MLs. For example, the band gaps of the semiconducting group 6 TMDCs are indirect in bulk but become direct in the monolayer form while also increasing in magnitude.[16,25,26,62] The thickness-dependency results from the interactions between the MLs. For ReS$_2$, the interlayer coupling is weak compared to group 6 TMDCs. Therefore, the direct band gap of ReS$_2$ is almost unchanged from bulk to a monolayer (**Figure 3**a).[71] ReS$_2$ may thus be viewed as an "ideal" 2D material, where individual monolayers act as individual 2D layers even in bulk material. On the other hand, PtS$_2$ displays much stronger interlayer coupling: the small optical band gap of bulk PtS$_2$ of 0.25 eV increases to approximately 1.0 eV for 5 ML and as large as 1.6 eV for a single ML.[72]

When several structures are possible for a given material, controlling the structure during synthesis or use opens an avenue for controlling its properties.[35] For example, for MoTe$_2$ the semimetallic 1T' phase is a high-temperature phase, whereas the semiconducting 2H phase is observed at lower temperatures or after slow cooling.[73] The orthorhombic T$_d$ phase that exhibits exciting topological and superconducting phenomena can be obtained by cooling the 1T' phase rapidly below 250 K.[74] In other cases, phase transitions may be induced by pressure, strain, chemical treatments, light, and electric or magnetic fields.[35,75,76]
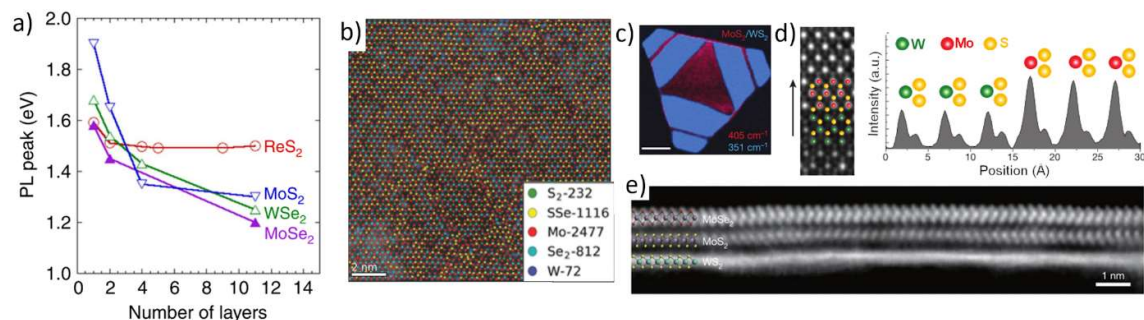
Figure 3. a) Photoluminescence peak position (optical band gap) of ReS_2 and some group 6 TMDCs as a function of thickness (number of layers). b) Plan-view high-angle annular dark-field scanning transmission electron microscope (HAADF-STEM) image of a quaternary $Mo_xW_{1-x}S_{2y}Se_{2(1-y)}$ monolayer alloy with different atoms shown in different colors. c) Raman map (MoS_2 and WS_2 shown in red and blue) and d) plan-view HAADF-STEM image and intensity profile of an atomically sharp MoS_2/WS_2 lateral heterostructure. e) Cross-sectional HAADF-STEM image of a vertical $WS_2/MoS_2/MoSe_2$ heterostructure (layers listed from bottom/substrate to top). a) Reproduced with permission.[71] Copyright 2014, Macmillan Publishers Limited, part of Springer Nature. b) Adapted with permission.[77] Copyright 2017, WILEY-VCH Verlag GmbH. c,d) Adapted with permission.[39] Copyright 2018, Macmillan Publishers Limited, part of Springer Nature. e) Reproduced with permission.[78] Copyright 2017, Macmillan Publishers Limited, part of Springer Nature.

Due to the similar crystal structures of layered TMDCs, alloying easily occurs and can be used to tune their properties (Figure 3b). For example, quaternary $Mo_xW_{1-x}S_{2y}Se_{2(1-y)}$ alloys enable band gap tuning from 1.6 to 2.0 eV in the monolayer form.[77] Mixing 2H-$MoTe_2$ and 1T'-WTe_2 into a ternary $Mo_{1-x}W_xTe_2$ alloy results in a phase transformation at x = 0.08 accompanied by a semiconductor-semimetal transition.[79] Substitutional doping as well as chemical doping by surface adsorbants are also promising methods to modify the properties of TMDCs.[80,81]

TMDCs – and other 2D materials – may be combined together to form heterostructures, either vertically or laterally.[82–86] Growth of a TMDC from an edge of another TMDC crystal forms a lateral (in-plane) heterostructure with ideally an atomically sharp, seamless junction (Figure 3c–d). In vertical heterostructures, (a few) monolayers of different TMDCs are grown or transferred on top of each other (Figure 3e). The interlayer interactions between the MLs of different materials separated by vdW gaps modify the properties of the heterostructures.[87] Considering the large variety of properties displayed by TMDCs and other 2D materials,

heterostructures enable formation of high-quality metal-insulator, metal-semiconductor, and p-n junctions, among others, offering great potential for both conventional and novel devices.

Due to the layered crystal structure, TMDCs display large anisotropicity between the in-plane and out-of-plane properties. For example, the in-plane electrical and thermal conductivities of MoS_2 are approximately 1000 and 50 times larger, respectively, compared to the out-of-plane direction.[88,89] The anisotropicity enables tuning properties of TMDC films by their morphology. The anisotropicity is also displayed in reactivity of TMDCs, which is important for their growth and applications, as well as ambient stability. TMDCs, especially in the monolayer form, expose a very large portion of their atoms on the surface. The lack of dangling bonds stabilizes the basal planes of TMDCs in ambient conditions so that oxidation and other reactions preferentially occur at defect and edge sites. Therefore, the stability of TMDCs – as well as their performance in applications – is highly dependent on their morphology and quality, and therefore preparation conditions.[90–93]

High-quality MoS_2 monolayers have been reported to be stable in the atmosphere for at least 18 months.[94] Typically, the tendency toward oxidation increases when going from sulfides to selenides and tellurides, and, in many cases, when going down a group of metals (e.g. from Mo to W and from Ti to Hf).[93,95] Group 4 and 5 TMDCs appear to oxidize on the surface within minutes to hours in air.[95–98] Encapsulation with polymers, transferred flakes of hBN, and ALD-grown oxide layers has been found effective in protecting TMDCs from oxidation in the atmosphere.[93]

3. Atomic Layer Deposition of Two-Dimensional Metal Dichalcogenides

3.1. Concept of Atomic Layer Deposition

ALD is a gas-phase thin film deposition technique. Often considered an advanced modification of CVD, ALD relies on spatially or temporally separated, saturative surface reactions of gas-phase precursors.[40–44] Once pulsed onto the surface, the first (metal) precursor adsorbs and reacts with the surface groups (e.g. –SH) until all of the available reaction sites are consumed or sterically blocked by neighboring precursor molecules (step i in **Figure 4**a). The excess precursor and reaction byproducts are then purged or pumped away (step ii). Next, the second (nonmetal) precursor is pulsed to replace the remaining ligands of the first precursor with reactive groups that contain the nonmetal element of the film (e.g. –SH, step iii). After the second purge/pump step (step iv), the ALD cycle is started again and repeated as many times as needed to reach the desired film thickness.
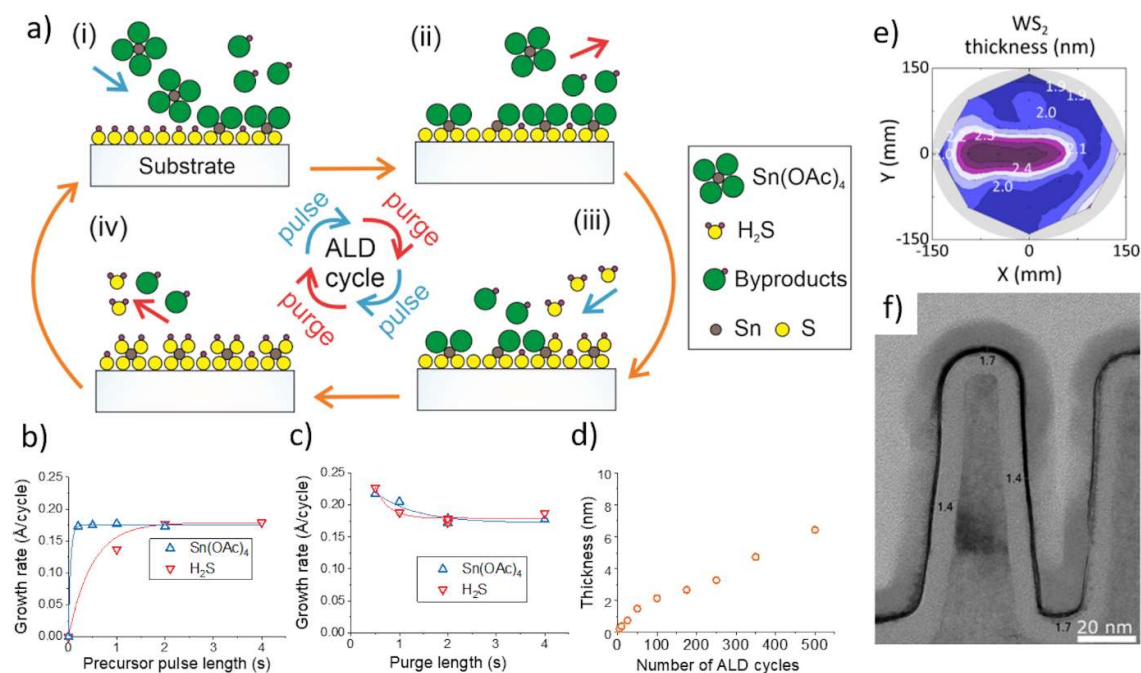
Figure 4. a) Schematic, simplified illustration of an ALD cycle for SnS_2 using $Sn(OAc)_4$ (OAc = acetato) and H_2S as precursors. ALD growth characteristics of the same SnS_2 process with varying b) precursor pulses, c) nitrogen purges, and d) number of ALD cycles. Examples of the e) excellent large-area uniformity (thickness between 1.9 to 2.4 nm on a 300 mm wafer) and f) conformality (thickness 1.4 to 1.7 nm on nanoscale trenches) of ALD WS_2 films. b–d) Reproduced with permission.[99] Copyright 2018, WILEY-VCH Verlag GmbH. e) Reproduced

Even though ALD films are often considered to grow layer-by-layer, in most cases each cycle deposits less than a monolayer of the film material. Experimentally, the saturative nature of the surface reactions is usually verified by increasing the precursor dose (pulse length), which should lead to a constant, saturated growth rate (also denoted growth per cycle) once a sufficient precursor dose is supplied (Figure 4b). In a similar manner, the length of purge or evacuation steps is increased until a constant growth rate is reached, which indicates complete removal of precursors and byproducts from the reactor (Figure 4c). This saturative behavior is a prerequisite for the excellent characteristics of ALD and should thus be studied for each precursor combination. The growth rate can, however, vary with the reaction temperature due to changes in reactivity, density of reactive sites, and growth mechanisms – or non-idealities such as precursor decomposition and condensation. In many cases, films deposited at low temperatures are amorphous and crystallization occurs when the deposition temperature is increased. Crystallization can affect the growth behavior and rate – not the least in the case of 2D materials due to their unique crystal structures.

The self-limiting, alternating nature of surface reactions gives ALD its unique advantages: excellent reproducibility, accurate control of thickness (Figure 4d) and composition, good scalability, and unbeatable uniformity (Figure 4e) and conformality (Figure 4f) on both large and complex shaped substrates. ALD reactions usually proceed at relatively low temperatures, from room temperature up to about 500 °C, which enables use of ALD in different applications.[44–46] The success of ALD relies on identifying precursors that fulfill a strict set of requirements including volatility, thermal stability, and reactivity.[40,41] Most research on ALD chemistry has focused on tuning the properties of the metal precursors through the use of different ligands, whereas simple hydrides, such as H_2O and H_2S are often used as non-metal precursors (also called reactants).[101–103] Nevertheless, more complicated molecules, such as

alkylsilyl compounds of selenium and tellurium as well as plasma-activated reactants are increasingly used to improve film properties and access new film compositions.[104–107]

3.2. Specialties in the Atomic Layer Deposition of Two-Dimensional Materials

Although ALD is often used to deposit ultrathin films, the extreme thinness and anisotropy of TMDCs means that adjustments to the common ALD picture are necessary. The growth behavior and mechanisms during the ALD of 2D materials may be expected to differ from the growth of conventional materials with 3D crystal structures.

It is important to keep in mind, especially for TMDC films only a (few) monolayer(s) thick, that during the first ALD cycles the film growth occurs on the substrate (part i in **Figure 5**a), which can lead to a different growth rate and mechanism compared to the film-on-film growth during later ALD cycles.[108] The nucleation phase has a strong effect on film characteristics, such as grain size, as will be discussed below. Even though ALD excels in film thickness control, it may be difficult to obtain films without local thickness variations of a few monolayers between adjacent crystallites (ii). Thickness variations may arise, for example, from different orientations of the crystallites, which can affect the growth rate, or local variations in nucleation delay. Such variation can be detrimental when aiming for few layer or even monolayer TMDC films of uniform thickness.

It seems naïve to think that the 2D materials would always grow in a perfect layer-by-layer manner by ALD – especially because the growth per cycle values are often one or even two orders of magnitude lower compared to a TMDC monolayer thickness. The edges of TMDC crystals are reactive (iii), whereas the basal planes should be rather inert toward precursors (iv) except for defect sites (v). Anisotropic growth mainly occurring on the edges of TMDC crystals may explain the low growth rates and high lateral grain sizes of TMDCs that are usually larger compared to ALD films of most other materials at similar thicknesses. Defects on basal planes may contribute to local thickness variations. If the basal planes were perfectly inert and oriented

parallel to the substrate, the anisotropic reactivity would result in very smooth and uniform films as is indeed sometimes observed for very thin ALD TMDC films of only a few MLs in thickness.

It is not clear how additional TMDC monolayers form on top of the first one, but this does occur in most of the ALD TMDC processes excluding some processes operating at very high temperatures. One possibility is that vdW interactions may allow precursors to adsorb on the basal planes.[109] Another open question is the importance or even existence of –XH (X = S, Se, Te) surface groups in the growth of TMDCs (on the edges or even on basal planes) analogous to –OH groups in the ALD of oxides (vi), as the former appear to be much more unstable.[4] Enhancing the inertness of the basal planes and therefore inhibiting growth of additional layers on top may be an interesting approach to yield uniform monolayer ALD TMDC films, which so far has been challenging.

Diffusion processes, on the surface and even in the "bulk" of the TMDC films, can aid in placing the TMDC constituent atoms into correct sites of the layered structure. For example, atoms may end up in "incorrect" sites if a metal precursor adsorbs onto a chalcogen vacancy, or even on top of a chalcogen-terminated TMDC monolayer (vii). Surface diffusion has been shown to be especially important when growing mobile materials on inert surfaces, for example ALD Pt on graphene.[110] A complete TMDC monolayer may also be regarded as an inert material.
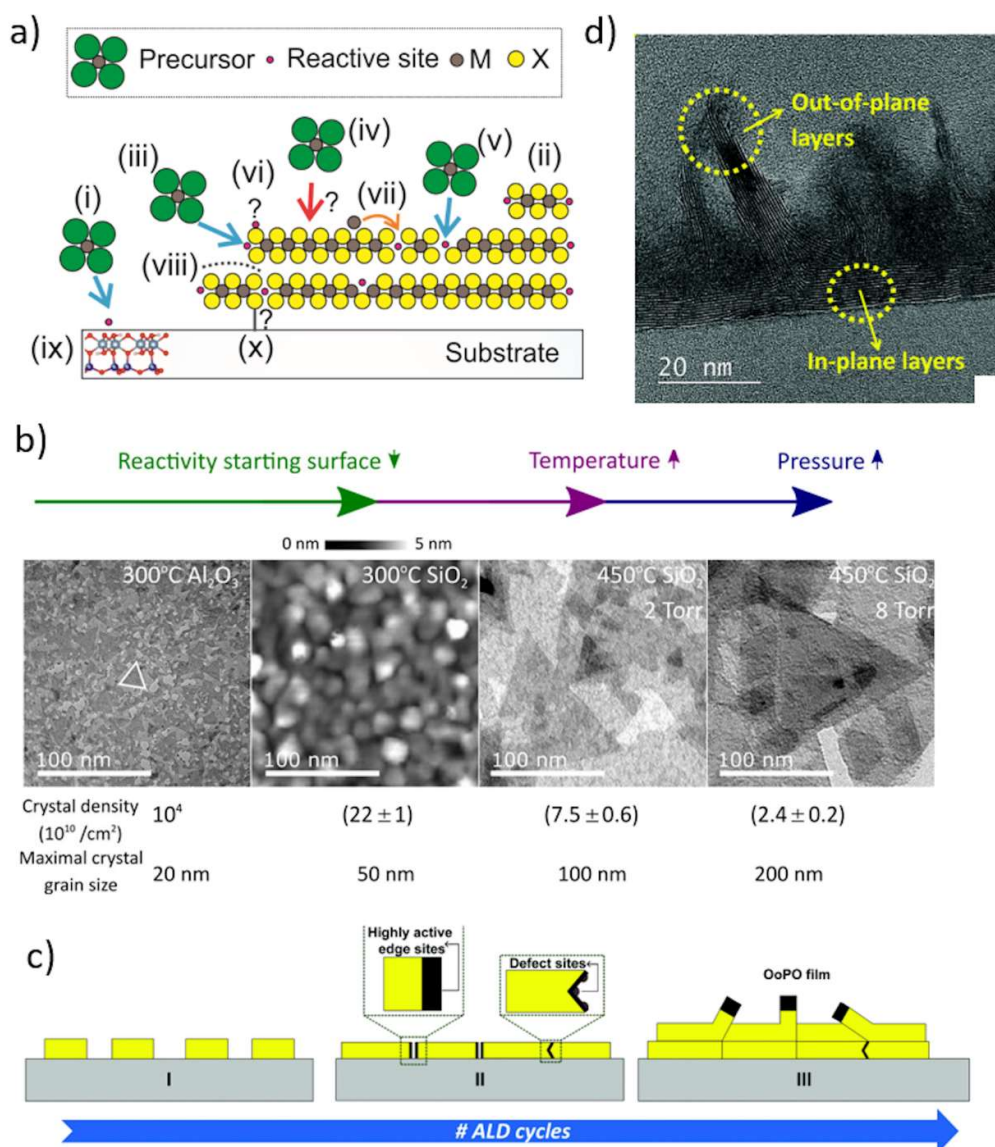
Figure 5. a) Schematic illustration of some specialties in ALD of TMDCs: i) precursor chemisorption onto substrate, ii) local thickness variations, iii) chemisorption onto TMDC edges, iv) possible (lack of) chemisorption on basal planes, v) chemisorption onto defects, vi) possible existence of reactive groups on the basal planes, vii) surface diffusion, viii) grain boundary, ix) effect of substrate structure, and x) bonding between the film and substrate. b) Plan-view transmission electron microscopy (TEM) and atomic force microscopy (AFM) images illustrating increase of grain size of ALD WS2 by decrease of nucleation density, which was achieved by changing the substrate and deposition conditions. Reproduced with permission.[111] Copyright 2018, American Chemical Society. c) Schematic and d) cross-sectional TEM image of formation of randomly oriented MoS2 flakes with increasing film thickness (OoPO = out-of-plane oriented). Reproduced with permission.[105] Copyright 2018, Royal Society of Chemistry.

Compared to the most common ALD materials, oxides, cation diffusion in ALD sulfides has generally been observed to be much faster. Thus, even bulk and grain boundary diffusion processes may become important in ALD of TMDCs. One reason for this may be the often lower melting points of chalcogenides compared to oxides, which increases diffusion rates if the temperature is kept constant.[112–114] Because an increase of temperature increases diffusion rates as well as the reactivity of precursors, it can be postulated that the deposition temperature should be as high as allowed by the precursors and underlying layers to facilitate formation of high-quality TMDCs. Also, it may be easier to deposit high-quality films of TMDC materials with low melting points such as SnS_2 (melting point 865 °C) compared to the TMDCs of refractory metals, such as MoS_2 (melting point 1750 °C).

Diffusion processes offer a possible route to control (increase) the grain size, which is an important topic in TMDC research due to the often detrimental effects of grain boundaries (viii). Nucleation density also affects the grain size. Typically, in ALD it is preferred to have as high a nucleation density as possible in order to obtain a closed film at a small thickness. On the contrary, in the 2D CVD community, very low nucleation densities are sought for in order to obtain large grain sizes.[115–117] In an extreme, and perhaps the ideal case, a nucleation density as low as one nuclei per substrate has been achieved using CVD.[115] However, rapid lateral growth and suppression of vertical growth are then required in order to form thin continuous films. Whether this approach can be applied to ALD-like conditions in a practical manner remains to be seen.

Some of the first studies on nucleation and diffusion control have shown up to an order of magnitude increase in the grain size of ALD TMDCs by decreasing the nucleation density and promoting diffusion (Figure 5b).[111,118,119] As a trade-off, however, the formation of a continuous film is then delayed and the thickness variations between adjacent crystallites may become more pronounced. Another approach could be to passivate the substrate surface perhaps followed by formation of nucleation sites only in controlled locations (partial passivation has

already been shown to increase grain size of MoS_2).[118] However, this approach might suffer from difficulties in defect-free passivation similar to most of the existing area-selective ALD processes,[120,121] and would ideally still require hindering of vertical growth. Recently, first investigations into area-selective ALD of TMDCs based on both inherent material selectivity[122–124] and area-selective passivation[121,125] have been reported, although these studies have not focused on increasing the grain size. Nevertheless, it is clear that controlling nucleation and diffusion is a powerful approach to tailor growth of ALD TMDCs that should be further examined.

The substrate always plays an important role in ALD and is particularly important for 2D materials (ix).[99,111,123,126–128] The substrate affects the nucleation, diffusion, and crystallite orientation, for example. In epitaxial films, all of the nuclei ideally orient in the same way due to the matching structures of the film and substrate, which allows the growing nuclei to eventually merge together into a large monocrystalline film. For 2D materials, a special case of epitaxy called van der Waals (vdW) epitaxy is possible, which circumvents many limitations of conventional epitaxy including the need of precisely matching structures and lattice parameters.[129,130] The possibility of vdW epitaxy of ALD TMDCs has been presented, but needs further improvement to fully utilize its potential.[126,128,131]

One important issue related to the substrate is whether the ALD-grown TMDCs bond covalently to the substrate (x). In an ideal case, an interface with only vdW bonds between the film and the substrate would be formed. However, with typical substrates that contain dangling bonds, such as SiO_2, formation of covalent bonds and therefore an interlayer between the substrate and TMDC seems likely and is also supported by theoretical studies.[132,133]

All of the abovementioned factors affect the resulting morphology of ALD TMDC films. Furthermore, it is often observed that in the beginning of the film growth, very thin ALD TMDC films are smooth. In thicker films, however, grains start to grow at random angles with respect to the substrate, which results in rough films. For some MoS_2 and WS_2 PEALD processes, the

randomly oriented flakes have been observed to originate from grain boundaries that form upon coalescence of initially formed nuclei (Figure 5c,d).[105,107] Interestingly, it has been shown that such randomly oriented flakes can be suppressed by additional H_2 or Ar plasma steps.[107]

The discussion above mostly concerns deposition of crystalline TMDCs. However, as will be discussed later, many ALD TMDCs are amorphous as-deposited and may be of non-ideal stoichiometry. Deposition of amorphous TMDC films can be more straightforward, as it avoids the effects of their unique crystal structures on the growth behavior. While amorphous TMDC films are sometimes preferred for some applications, in many cases post-deposition annealing is used to crystallize the films. It appears that deposition of amorphous films followed by post-deposition crystallization is a promising approach to obtain smooth, crystalline films.[99,134,135] Furthermore, the grain size may then be controlled by the annealing step instead of the first ALD cycles. Conversion of other ALD-grown materials, such as oxides, to TMDCs also bypasses many of the unique challenges related to the deposition of crystalline TMDCs, but often requires high temperatures.

3.3. Comparison of Atomic Layer Deposition to Other Methods

For practical industrial applications, TMDCs need to be deposited uniformly on large substrates as continuous, high quality films of accurately controlled thickness. The deposition conditions, especially temperature, have to be compatible with the target substrates and device structures, and the processes should ideally be easily scalable.[136,137] Large selection of materials and ability to tune film properties and growth conditions are additional assets toward use in different applications that benefit from different materials, film thicknesses, morphologies, defect densities, and so forth. Ultimately, the choice of the deposition method comes down to the requirements set by a particular application, and it is unlikely that a single method ideal for all applications can be found.

In order to place ALD into context, we compare ALD to other methods used to deposit TMDCs (**Figure 6** and **Table 1**). The investigations into TMDCs began and largely continue using mechanical exfoliation (Figure 6c) of bulk crystals.[10,26] Unfortunately, mechanical exfoliation cannot be scaled up. Another top-down method, liquid exfoliation is scalable, but tends to result in ill-defined films when the exfoliated flakes are deposited onto a substrate.[26,138] Herein, we focus on bottom-up gas-phase methods used to grow TMDCs, which offer the highest level of control.
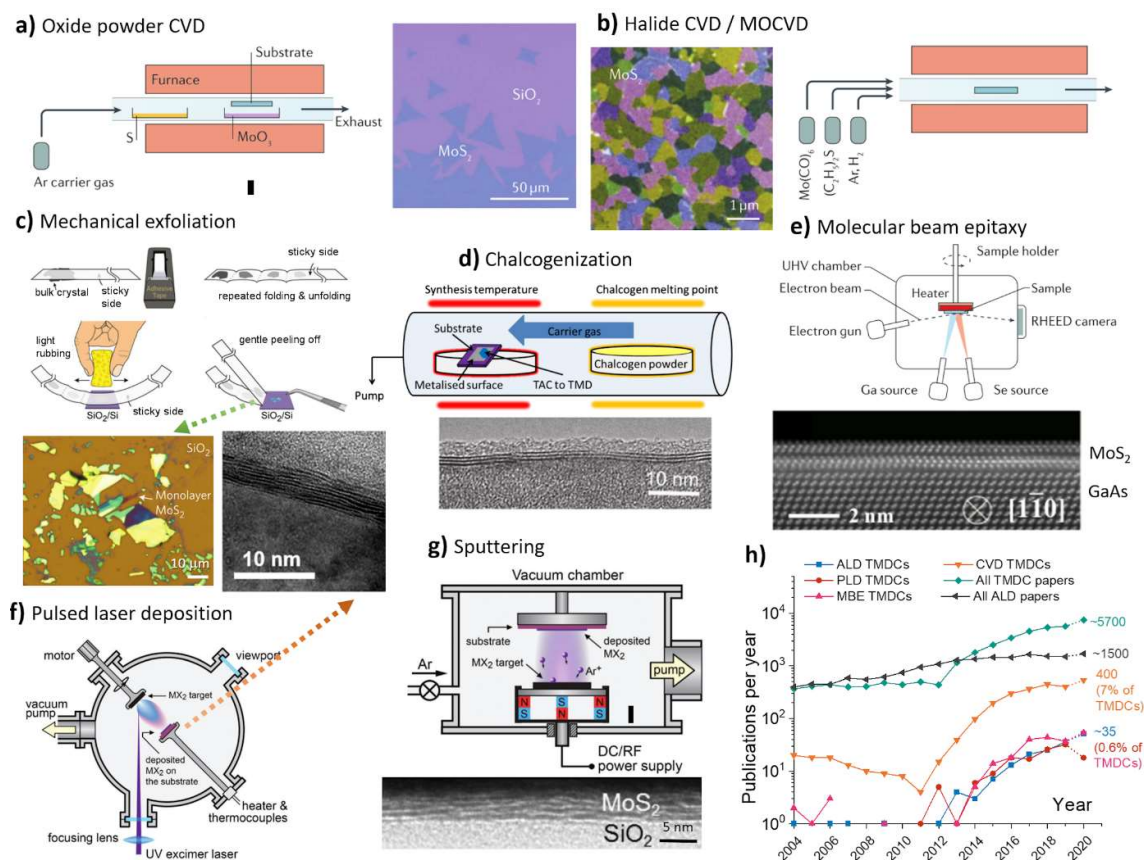
Figure 6. a–g) Illustration of different methods used to deposit TMDCs from gas phase and microscope images of representative films produced (optical microscopy in a) and c); plan-view TEM in b), cross-sectional TEM in d–g). Mechanical exfoliation is shown for comparison. h) Popularity of selected methods in deposition of TMDCs. For comparison, the total number of publications on TMDCs and ALD are also shown. The numbers refer to publications in 2019. The values for 2020 are extrapolated based on the numbers obtained using Scopus on 29 April 2020. a) Optical image: Reproduced with permission.[139] Copyright 2014, American Chemical Society. a,b,e) Schematics: Reproduced with permission.[25] Copyright 2017, Macmillan Publishers Limited, part of Springer Nature. b) TEM image: Reproduced with permission.[37] Copyright 2015, Macmillan Publishers Limited, part of Springer Nature. c) Optical image: Reproduced with permission.[20] Copyright 2013, Macmillan Publishers Limited, part of Springer Nature. c,f,g) Schematics: Reproduced with permission.[26] Copyright 2018, The

Royal Society of Chemistry. d) TEM image: Reproduced with permission.[18] Copyright 2012, WILEY-VCH Verlag GmbH. Schematic: Reproduced with permission.[140] Copyright 2016, Elsevier. e) TEM image: Reproduced with permission.[141] Copyright 2016, The Japan Society of Applied Physics. f) TEM image: Reproduced with permission.[142] Copyright 2016, American Chemical Society. g) TEM image: Reproduced with permission.[143] Copyright 2014, AIP Publishing.

Oxide powder precursor CVD employing solid MO_3 (M = Mo, W) and elemental X (X = S, Se, Te) precursors is one of the most commonly used TMDC deposition methods. This method, for which different names are used in the literature, can produce large single crystals up to hundreds of micrometers in width. However, continuous films are difficult to obtain, and high temperatures of 600–1000 °C are required for oxide powder precursor CVD (Figure 6a). Use of halide or metal-organic precursors in CVD allows for improved scalability for wafer-scale deposition and often lower deposition temperatures compared to oxide precursors, even below 500 °C, although the best films are deposited at temperatures closer to 1000 °C. In addition, the grain size of the resulting films tends to be smaller compared to the oxide powder precursor CVD (Figure 6b). Chalcogenization of metal or metal oxide "precursor" films deposited using methods such as ALD, CVD, evaporation, or sputtering, is another common method, which requires high temperatures similar to CVD and results in nanocrystalline films (Figure 6d). We will include chalcogenized ALD films in discussions throughout this review.

Different physical vapor deposition (PVD) techniques have also been applied to the growth of TMDCs. These methods typically use MX_2 compounds or elemental M and X as precursors. Molecular beam epitaxy (MBE) has been used to grow films of several selenides and tellurides rarely deposited by other methods, whereas MBE-grown sulfides are less common. MBE requires expensive ultra-high vacuum (UHV) equipment, but it can be scaled up. MBE produces high quality films with a good control over film thickness and composition – especially when a suitable single crystal substrate allowing epitaxial growth is used (Figure 6e). Pulsed laser deposition (PLD) has also been used to grow selected TMDC materials (Figure 6f). Sputtering is a widely used thin film deposition method and can be scaled up to very large substrates,

although its use for TMDCs is still in its infancy (Figure 6g). More rarely, reactive evaporation of metals at approximately 500 °C in high vacuum under a chalcogen atmosphere[144–146] or physical vapor transport (PVT) of MX_2 powders evaporated at 900–1200 °C in low vacuum or atmospheric pressure[147,148] have been used. Both of these methods have been mainly used to prepare monolayer islands and they do not seem to offer obvious benefits over oxide powder precursor CVD, for example.

Compared to the other methods, some of the main assets of ALD are its scalability and ability to produce uniform and continuous films on large areas – even if deposition of a monolayer ALD TMDC film is no trivial task. ALD can be scaled up for industrial use in a straightforward manner, which is very difficult for the oxide powder precursor CVD due to its sensitivity to the precursor doses that are usually poorly and irreproducibly controlled,[149] not to mention mechanical exfoliation. The relatively low temperatures in ALD are also highly advantageous regarding both cost and process compatibility. The excellent conformality of ALD further broadens the scope of possible applications and substrates to be coated. In contrast, PVD methods cannot usually coat nanostructured substrates, which are increasingly used in different applications from electronics to energy storage and energy production. The facile composition control of ALD enables deposition of solid solutions as well as heterostructures of TMDCs. Supported by the ability to deposit films from a (few) monolayer(s) to tens of nanometers thick with only a change of the number of ALD cycles, it is clear that flexibility is one of the main advantages of ALD. The flexibility can also be observed from the wide range of possible applications already explored for ALD TMDCs. In many cases, ALD TMDCs have shown performance comparable to some of the best films deposited using other methods as will be discussed in this review. However, at present ALD is not able to match CVD in deposition of monolayer flakes and films with large grain sizes.

It is interesting to note that the use of ALD for the deposition of TMDCs currently seems to be on a similar level with PLD and MBE, each accounting for approximately 0.6% of TMDC

papers published in 2019. In comparison, approximately ten times more papers were published

using CVD-grown TMDCs (Figure 6h; the CVD number also includes many publications on

chalcogenization). Although in this respect ALD currently seems to be lagging behind CVD, it

will be interesting to see how the numbers evolve as a large portion of the CVD papers use

oxide powder precursors that seem unlikely to make it from labs to production.

Table 1. Comparison of ALD and other methods used to deposit TMDC flakes and films (methods producing dispersions etc. are excluded, see Refs. [26,150,151]). Methods are evaluated on a three-point "poor-fair-high" scale. GS = grain size.

	ALD	Mechanical exfoliation	Oxide powder precursor CVD	Halide CVD, MOCVD	Chalcogenization of M/MO$_x$ film	Sputtering, PLD	MBE
Typical conditions	T = 50–500 °C $p \approx 1$ mbar N$_2$	(Inert) ambient conditions	T = 600–1000 °C $p \approx 1$–1000 mbar N$_2$/Ar (+ H$_2$)	T = 400–1000 °C $p \approx 1$–1000 mbar N$_2$/Ar (+ H$_2$)	T = 600–1000 °C $p \approx 1$–1000 mbar N$_2$/Ar + S/Se/Te	T = 400–800 °C $p \approx 10^{-4}$–10^{-7} (PLD), 10^{-2} mbar (sputt.)	T = 200–800 °C $p \approx 10^{-7}$–10^{-10} mbar
Quality (grain size)	Poor to Fair (amorphous to ~100 nm GS)	High (depends on bulk crystal, GS ≈ 10 μm)	High (GS ≈ 1–100 μm)	Fair to High (GS ≈ 10 nm –10 μm)	Poor to Fair (GS <10–100 nm)	Fair (GS ≈ 10–100 nm)	Fair to High (GS ≈ 10–100 nm, often epitaxial)
Continuity	Fair to High (monolayer difficult)	Poor (flakes)	Fair (possible in a limited area)	High	Fair (monolayer difficult)	High	Fair (monolayer difficult)
Uniformity	High	Poor	Poor	High	Fair to High	Fair to High	Fair to High
Scalability	High	Poor	Poor	High	High	Fair to High	Fair
Thickness control	High	Poor	Fair	Fair	High	High	High
Conformality	High	Poor	Poor	Fair	Depends on how "precursor" film is prepared	Poor	Poor
Current material selection	Fair (HfS$_2$, MoS$_2$, MoSe$_2$, ReS$_2$, SnS$_2$, TiS$_2$, WS$_2$, WSe$_2$, ZrS$_2$)	High (~all TMDCs)	High (most TMDCs)	Fair (HfS$_2$, HfSe$_2$, MoS$_2$, MoSe$_2$, NbS$_2$, SnS$_2$, TaS$_2$, WS$_2$, WSe$_2$, ZrS$_2$, ZrSe$_2$)	Fair (Mo, W, Pt based TMDCs)	Fair (MoS$_2$, MoTe$_2$, ReS$_2$, SnSe$_2$, ZrS$_2$, WS$_2$, WSe$_2$, WTe$_2$)	High (most selenides and tellurides, some sulfides)
Ref.	[47–50], this work	[10,26,152]	[22,26,153–156]	[26,37,38,56,157–160]	[26,154,156,161,162]	[26,163–170]	[130,171,172]

3.4. Atomic Layer Deposition Processes for Two-Dimensional Metal Dichalcogenides

Herein, we give a brief overview of ALD TMDC materials, precursors, and applications studied. For more details on deposition chemistry and processes, the reader is referred to earlier reviews.[47–50] In **Table 2**, we provide a list of ALD TMDC papers until the end of August 2020 including the precursors, deposition and post-treatment temperatures, examined film thicknesses, crystallinity and grain size, and applications. In **Table 3**, analogous information is provided for TMDC films produced by conversion (chalcogenization) of ALD grown films.

In the ALD community, MoS_2 has been by far the most studied TMDC, accounting for nearly half of the published papers (**Figure 7**a). There has also been notable and constant activity on SnS_2 and WS_2 over the years, which together with MoS_2 constitute nearly four out of five published papers. A few reports on selenides $MoSe_2$ and WSe_2 have been published, too. In addition to the recent processes for semiconducting HfS_2, ZrS_2, and ReS_2, a few studies have also been published on TiS_2 with metallic conductivity.
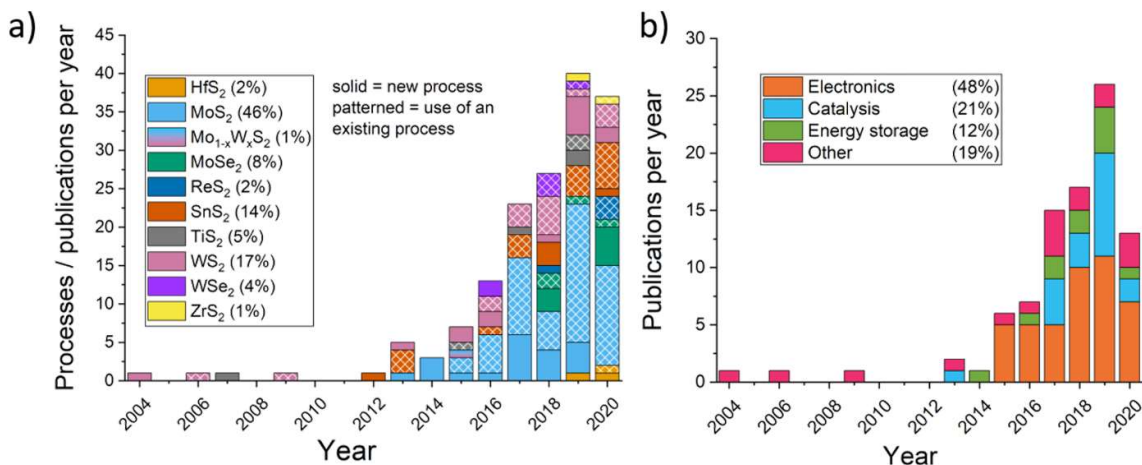
Figure 7. Evolution of ALD TMDC publications by a) material, and b) studied applications. In a), solid bars refer to new processes and patterned bars to further studies on established processes. Note that a single publication may be counted multiple times, if several processes or applications were examined. Data for 2020 are up to 31 August 2020 (not extrapolated).

There is still plenty of room to broaden both the precursor and material selection of ALD TMDCs. For example, metallic group 5 sulfides (VS_2, NbS_2, and TaS_2), many selenides, and all tellurides await to be deposited. ALD should also be well suited for the deposition of TMDC alloys, yet only a single

report exists so far. On the other hand, there is still a need for even new MoS$_2$ processes with good ALD characteristics that produce smooth, high-quality films at low temperatures, for example.

It is apparent that in the future, stronger emphasis should be placed on studying the ALD characteristics of the reported processes, as many of the explored precursor systems lack verification of the self-limiting nature of the surface reactions. Due to the unfortunate lack of this information, we have included all processes denoted as ALD in this review, even if some of them may not behave as true ALD processes. The importance of self-limiting reactions in enabling the excellent uniformity, conformality, scalability, and repeatability of ALD as well as its industrial applications cannot be stressed enough.

Nearly half of the ALD TMDC papers exploring possible applications have examined the films for electronics and optoelectronics (including sensors), about one fifth for electrocatalysis and photocatalysis, and one eighth for energy storage with the remaining one fifth looking at other applications such as lubrication, plasmonics, and photonics (Figure 7b). Lubricating coatings dominated the first studies since 2004 and studies on the topic are still published. Electronics and related applications have been very actively studied since 2015. Since 2017, studies on catalysis have been growing particularly strongly. In energy storage, there has been relatively stable activity since 2014, if on a lower level compared to electronics and catalysis.

For the ALD TMDC processes, common metal halide precursors have been in active use (**Figure 8**). Although halides are often well behaving ALD precursors, possibility of etching reactions should be kept in mind for group 5 to 7 metals (see Chapter 5.2. in Ref. [70]). Metal carbonyls have seen widespread use for Mo and W and the use of nitrogen-bonded amido/imido ligands has been on the rise for a range of metals. Some compounds containing oxygen-coordinated ligands including Mo(thd)$_3$ (thd = 2,2,6,6-tetramethyl-3,5-heptanedionato), Sn(OAc)$_4$ (OAc = acetato), and Sn(dmamp)$_2$ (dmamp = 1-dimethylamino-2-methyl-2-propoxide) have also been used in ALD of TMDCs.
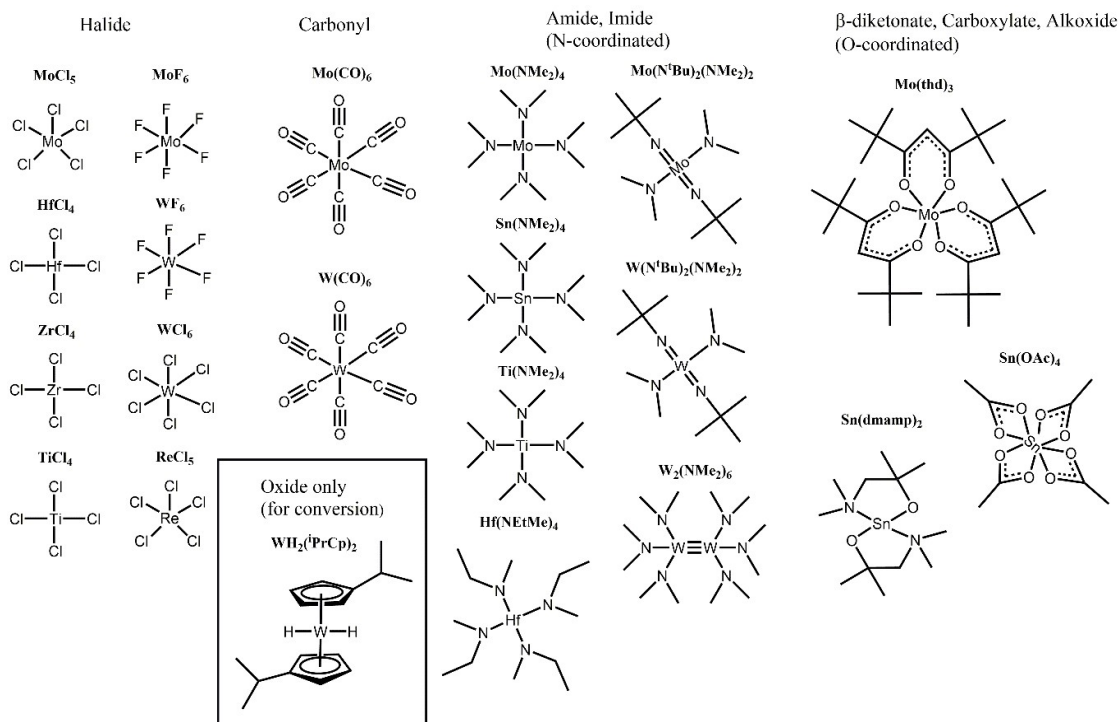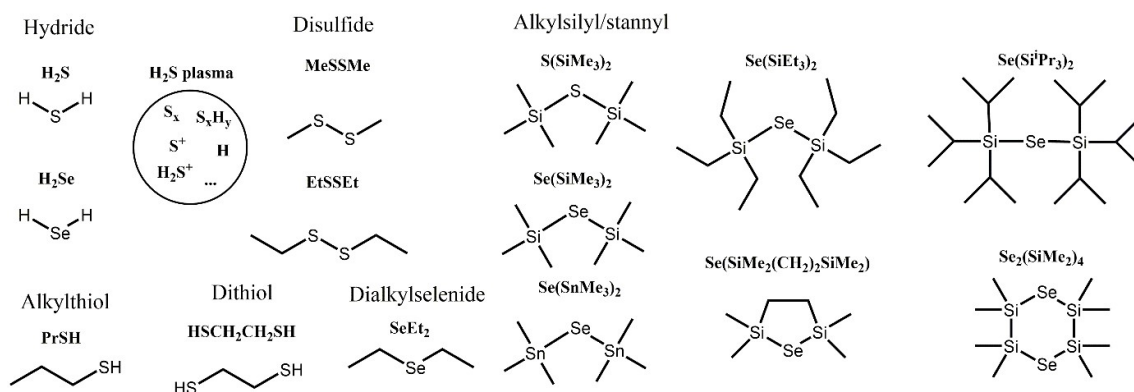
Figure 8. Structures of metal precursors used to deposit TMDCs by ALD. dmamp = 1-dimethylamino-2-methyl-2-propoxide, OAc = acetato, and thd = 2,2,6,6-tetramethyl-3,5-heptanedionato.

H_2S is by far the most commonly used sulfur precursor in ALD (**Figure 9**). H_2S plasma has been introduced as a more reactive alternative, in some cases with H_2 added to the plasma gas along with inert Ar. Disulfides MeSSMe (dimethyldisulfide) and EtSSEt (diethyldisulfide) have also been used and appear to perform adequately at least under low-temperature conditions. An alkylthiol PrSH (1-propanethiol) was recently introduced. A dithiol $HSCH_2CH_2SH$ (1,2-ethanedithiol) results in hybrid thiolate films. An alkylsilyl compound $S(SiMe_3)_2$ was also recently used to deposit MoS_2. A direct comparison of different sulfur precursors is yet to be performed, though.

Due to the limited availability of safe and reactive selenium precursors, until recently only a few studies on $MoSe_2$ and WSe_2 had been performed using either the highly toxic H_2Se gas or a rather inert alkyl $SeEt_2$. In 2018–2020, a range of alkylsilyl and alkylstannyl selenide precursors including $Se(SiMe_3)_2$, $Se(SiEt_3)_2$, $Se(Si^iPr_3)_2$, and $Se(SnMe_3)_2$ have been used to deposit $MoSe_2$. Furthermore, cyclic alkylsilyl precursors $Se(SiMe_2(CH_2)_2SiMe_2)$ and $Se_2(SiMe_2)_4$, which offer easier handling

compared to the alkylsilyl selenides were reported in 2020. Unfortunately, no ALD characteristics of any of the selenide processes have been reported.

Figure 9. Structures of chalcogen (sulfur and selenium) precursors used to deposit TMDCs by ALD.

Post-deposition annealing in either inert or chalcogen-containing atmospheres is often used to improve the crystallinity and grain size of as-deposited amorphous or nanocrystalline films. While annealing can improve the crystallinity substantially, the required temperatures are often so high that they hinder the use of annealing in practical applications.

Conversion (chalcogenization) of ALD metal, nitride, and oxide films into TMDCs can be considered a special case of post-deposition annealing. The conversion approach ideally retains most of the advantages of ALD, including conformality, uniformity, and thickness control. However, conversion usually requires high temperatures, thus limiting compatibility with different substrates, and tends to produce films with a small grain size. Furthermore, the potential volatility of the "precursor film" at the high temperatures required should be kept in mind. Especially MoO_3 becomes volatile at temperatures above 500 °C.[173] Therefore, the chalcogen species should be introduced at low enough temperatures to avoid the loss of the film uniformity and conformality. The processes used to deposit the ALD films, often oxides, as well as the chalcogenization conditions are listed in Table 3. In Section 4, the applications of the converted films will be discussed alongside directly grown ALD TMDCs.

Table 2. Summary of TMDC films deposited by ALD in alphabetical order (updated from Ref. [47]). Abbreviations: amorphous (amorp.), annealed (ann.), as-deposited (as-dep.), crystalline (cryst.), field-effect transistor (FET), hydrogen evolution reaction (HER), lithium ion battery (LIB), oxygen evolution reaction (OER), photocatalysis (PC), photoelectrocatalysis (PEC), sodium ion battery (NIB), supercapacitor (SC).

Precursors [a)	Deposition T [°C] (post-treatment T [°C], atmosphere) [b)	Thickness and morphology (estimated grain size) [c)	Applications	Year[Ref.] d)
		HfS_2		
$HfCl_4 + H_2S$	350–450	a few–tens of ML films (~10–30 nm)	photodetector	2019[174]
	400	10 nm film (cryst.)	–	2020[126]
$Hf(NEtMe)_4 + H_2S$ plasma	250–450	10–50 nm films (~10–30 nm)	–	2020[175]
		MoS_2		
$MoCl_5 + H_2S$	300 (800, S)	1 ML flakes, 1 ML to 10 nm films (as-dep. ~10 nm, ann. <2 μm)	–	2014[29]
	350–450	2 ML to 10 nm films (cryst.)	FET	2015[176]
	500–900	1–3 ML films (80–100 nm)	FET, p-n diode photodetector	2016[177] 2019[178]
	375–475 (600–900, S or H_2S)	a few ML films (cryst.)	–	2016[179]
	450	1–3 ML flakes (~100 nm) 4–10 ML films (~100 nm)	–	2017[180]
	420–490	10–50 nm films (20–100 nm)	–	2017[181]
	390–480	20–60 nm films (30–120 nm)	piezoelectric	2017[182]
	460	2.5–45 nm films (10–15 nm)	lubricant	2018[183]
	450	1–8 ML films (~15 nm)	lubricant	2019[184]
	430–480	1–10 ML films (cryst.)	lubricant	2020[185]
	460	1–5 ML films (~30–100 nm)	lubricant	2020[186]
	?	70 nm rough film (amorp.?)	lubricant, hydrophobic	2020[187]
	?	tens of nm rough film (cryst.)	biosensor	2020[188]
	400	tens of nm rough film (cryst.)	biosensor	2020[189]
	450	~5–50 nm rough films (~10–20 nm)	OER	2017[190]
	390–470	1–3 ML flakes (~50–400 nm) 4–5 ML films (~400 nm)	-	2019[119]
	250–325	20–70 nm rough films (10–100 nm)	HER	2017[191]
	150–300	5–50 nm rough films (10–300 nm)	LIB, NIB	2018[192]
	250–300	~5–70 nm rough films (10–50 nm)	PEC	2018[193]
	250	~20 nm rough film (~10–20 nm)	PEC	2019[194]
	250	~7–30 nm rough film (~10–30 nm)	PEC	2019[195]
	200–420	1–8 ML films (10–25 nm)	FET	2020[196]
$MoCl_5 + S(SiMe_3)_2$	375 (800, S)	8 ML film (as-dep. amorp., ann. cryst.)	FET	2019[197]

Precursors	Temperature	Film description	Application	Year
	300 (900, S)	5–8 ML films (as-dep. amorp., ann. cryst.)	FET	2019[198]
	300 (900, S)	5 nm film (ann. cryst.)	FET	2020[199]
	375 (500–700, N_2)	4 nm film (as-dep. amorp., ann. cryst.)	–	2019[200]
	375 (800, inert + 400, CS_2)	4 ML film (ann. cryst.)	FET	2019[201]
	300–350 (900, S)	4 ML film (as-dep. amorp., ann. cryst)	–	2020[122]
	350 (900, S)	4 ML film (as-dep. amorp., ann. cryst)	FET	2020[202]
MoF_6 + H_2S	200 (350, H_2)	~10–100 nm rough films (as-dep. amorp., ann. cryst.)	–	2018[203]
	200 (400 or 600, H_2 or H_2S)	~10 nm films (as-dep. amorp., ann. 4–10 nm)	–	2018[204]
	700	1–5 ML (cryst.)	FET, photodetector	2019[178]
$Mo(CO)_6$ + H_2S	155–170	10–50 nm films (amorp.?)	LIB	2014[205]
	120–175 (500–900, Ar or H_2S)	2 ML to 10 nm films (as-dep. amorp., ann. ~10 nm)	–	2016[206]
	200	? nm rough films (~5 nm)	OER	2017[207]
$Mo(CO)_6$ + H_2S plasma	175–225	5–30 nm rough films (15–20 nm)	–	2016[208]
	200	10–50 nm films (~5 nm)	SC	2017[209]
	200 (500–700, H_2S)	5–30 nm rough films (as-dep. 6–10 nm, ann. ~15 nm)	PEC	2017[210]
$Mo(CO)_6$ + $HS(CH_2)_2SH$	140–190 (350, H_2S/H_2)	~10 nm films (as-dep. amorp. hybrid thiolate, ann. ~5 nm)	HER	2018[211]
$Mo(CO)_6$ + EtSSEt	250 (450, Ar)	~5 ML films (100 nm)	FET	2017[118]
$Mo(CO)_6$ + MeSSMe	100 (900 , Ar)	5–10 nm films (as-dep. amorp., ann. 10 nm)	–	2014[212]
	100	2–10 nm films (amorp.)	HER	2015[213]
	100	2–15 nm films (<5 nm)	HER	2016[214]
	150 (650–700, Ar)	~5–50 nm films (as-dep. amorp., ann. cryst.)	photonic crystal	2017[215]
	150	~5 nm film (amorp.)	Li-O_2 battery	2019[216]
	98	3–16 nm film (amorp.)	solar cell electrode	2019[217]
$Mo(CO)_6$ + $S(SiMe_3)_2$	150 (800, S)	2–5 ML films (as-dep. amorp.?, ann. ~5–10 nm)	FET	2018[218]
$Mo(N^tBu)_2(NMe_2)_2$ + H_2S	275	a few ML islands to tens of nm films (~10–50 nm)	LIB	2019[219]
	275	a few ML islands (cryst.)	PEC, PC	2019[220]
	275	? nm islands (cryst.?)	LIB	2020[221]
$Mo(N^tBu)_2(NMe_2)_2$ + H_2/H_2S plasma	150–450	1 ML flakes to tens of nm rough films (10–50 nm)	HER	2018[105,222] 2019[223]
	450 (900, H_2S)	2 ML films to 40 nm rough films (cryst.)	-	2019[224]
$Mo(N^tBu)_2(NMe_2)_2$ + H_2S plasma	250 (750, S)	a few ML–10 nm films (ann. ~5–10 nm)	–	2019[127]
$Mo(N^tBu)_2(NMe_2)_2$ + PrSH	250–400	2 ML to 15 nm films (as-dep. amorp., ann. ~10 nm)	–	2019[225]
$Mo(NMe_2)_4$ + H_2S	60–120 (1000, S)	3–50 nm films (as-dep. amorp., ann. 100–200 nm)	FET	2017[226]

Precursors	Temp (°C)	Film description	Application	Year
	95	7.5–20 nm films (amorp.)	HER	2019[227]
	80 (300–800, S)	~10 nm films (as-dep. amorp., ann. ~5–10 nm)	HER	2020[228]
Mo(NMe$_2$)$_4$ + HS(CH$_2$)$_2$SH	50 (300, Ar or H$_2$; 450, H$_2$; or 800, Ar)	1–2 ML film (as-dep. amorp., ann. 10–20 nm)	–	2017[229]
Mo(thd)$_3$ + H$_2$S	250–350	~2–10 nm rough films (10–30 nm)	–	2017[123]
	270	~25 nm rough films (~20–50 nm)	–	2020[126]
MoSe$_2$				
Mo(CO)$_6$ + Se(SiMe$_3$)$_2$	167	1–10 nm films (amorp.)	PEC, PC	2018[230,231]
MoCl$_5$ + Se(SiMe$_3$)$_2$	300	>10 nm rough films (50–100 nm) ? nm rough films (cryst.)	– –	2018[230] 2020[232]
MoCl$_5$ + Se(SiEt$_3$)$_2$	300	? nm rough films (cryst.)	–	2020[232]
MoCl$_5$ + Se(Si^{i}Pr$_3$)$_2$	300	? nm rough films (cryst.)	–	2020[232]
MoCl$_5$ + Se(SnMe$_3$)$_2$	300	? nm rough films (cryst.)	–	2020[232]
MoCl$_5$ + Se(SiMe$_2$(CH$_2$)$_2$SiMe$_2$)	300	? nm rough films (~50–100 nm)	–	2020[233]
MoCl$_5$ + Se$_2$(SiMe$_2$)$_4$	300	? nm rough films (~20–50 nm)	–	2020[233]
ReS$_2$				
ReCl$_5$ + H$_2$S	120–500	~1–100+ nm rough films (10–300 nm)	–	2018[234]
	250–400	~10–20 nm rough films (~10–100 nm)	–	2020[126]
	400	tens of nm rough film (cryst.)	biosensor	2020[189]
	250–500 (700–900)	1–2 ML flakes 3–5 ML films (~50–100 nm)	–	2020[235]
SnS$_2$				
Sn(NMe$_2$)$_4$ + H$_2$S	135	~20 nm films (cryst. on Cu$_2$S)	–	2012[236] 2013[237]
	60–120 140–150 160–180	50 nm films (amorp. SnS$_2$) 50 nm films (~10 nm, SnS$_2$) 50 nm rough films (~15 nm, SnS)	–	2013[238]
	150	2–45 nm films (<10 nm films amorp., thicker cryst.)	–	2017[239]
	150 (250–350, S/H$_2$)	12 nm (as-dep. 15 nm, ann. 25 nm)	–	2016[135]
	150 °C (250–350, H$_2$S)	6 ML film (as-dep. partly cryst, ann. ~10 nm)	–	2017[240]
	150 (300, S/H$_2$)	12 nm film (as-dep. partly cryst, ann. cryst.)	FET	2017[241]
	150 (100 to 350 (multi-step), H$_2$S)	3–6 ML films (as-dep. partly cryst, ann. ~10–20 nm)	FET	2019[242]
	150 (100 to 350 (multi-step), H$_2$S)	7-10 ML films (as-dep. partly cryst, ann. ~10–20 nm)	FET	2019[243] 2020[244]
	150 (100 to 350 (multi-step), H$_2$S)	~50 nm rough films (~50 nm)	gas sensor	2019[245]
	150 (100 to 350 (multi-step), H$_2$S)	6 ML films (as-dep. ?, ann. ~10–20 nm)	–	2020[246]
	150	40 nm film (amorp.)	PEC	2020[247]
	90	~5–30 nm films (amorp.)	plasmonics	2013[248]

	60–140	25–100 nm films (amorp.)	PEC	2019[249]
	160	20–80 nm films (~10 nm)	SC	2019[250]
Sn(OAc)$_4$ + H$_2$S	150 (200–350, H$_2$S)	2–11 ML films (as-dep. amorp., ann. 20–30 nm)	–	2018[99]
	150–175 (250–300, H$_2$S)	~5 nm films (~10–70 nm)	–	2020[126]
	150–200 (200–350, H$_2$S)	<2–10 ML films (as-dep. amorp., ann. 15–70 nm)	–	2020[131]
Sn(dmamp)$_2$ + H$_2$S plasma	150–240 (300, H$_2$S)	~1–20 ML films to rough films (as-dep. partly cryst., ann ~10–30 nm)	FET	2020[251]
	180–240	? nm films (cryst.)	gas sensor	2020[252]
TiS$_2$				
TiCl$_4$ + H$_2$S	400–500	50–100 nm rough films (amorp. to 1 μm grains depending on substrate)	–	2007[253]
	75–250	3–50 nm films (partly cryst.)	solar cell absorber	2015[254]
	300	tens of nm rough films (50 nm)	LIB, NIB	2019[255]
Ti(NMe$_2$)$_4$ + H$_2$S	150–180	~5–100 nm films (amorp., oxidizes)	–	2019[256]
	100	~30 nm rough film (cryst.)	–	2019[257]
Ti(NMe$_2$)$_4$ + H$_2$S plasma	150–200	~30 nm rough film (~50–100 nm)	–	2019[257]
WS$_2$				
WCl$_6$ + H$_2$S [e)]	390	a few–10 ML (cryst.)	FET	2015[258]
WF$_6$ + H$_2$S	300 (500, vacuum)	~250 nm rough film (as-dep. ~10 nm, ann. ~30 nm)	lubricant	2004[28]
	300–350	10–400 nm rough films (5–100 nm)	lubricant	2006[259] 2009[260]
	300	1 ML film (<25 nm)	–	2018[124]
WF$_6$ + H$_2$ plasma + H$_2$S	250–450	2–5 ML films (~10 nm)	–	2015[261] 2017[100]
	300	2–5 ML films (5–20 nm)	–	2018[128]
	300	4–5 ML film (10–20 nm)	FET	2017[262]
	300–450	~1–5 ML flakes, ~2–5 ML films (tunable ~5–200 nm)	FET	2018[111]
W(CO)$_6$ + H$_2$S	165–205	20–40 nm (amorp.)	LIB	2016[263]
	400	175 nm rough films (~5 nm)	lubricant	2016[264] 2017[265]
W(CO)$_6$ + H$_2$S plasma	350	3–20 nm films (3–7 nm)	HER, NIB	2018[266]
	350	20–60 nm rough films (3–10 nm)	NIB	2019[267]
W(N^{t}Bu)$_2$(NMe$_2$)$_2$ + H$_2$S	300	~5–50 nm rough films (~10–30 nm)	HER	2019[268]
W(N^{t}Bu)$_2$(NMe$_2$)$_2$ + H$_2$S plasma	300	~8–65 nm rough films (~10–20 nm)	HER	2019[269]
	450	~6 nm rough films (14±1 nm)	–	2020[107]
	250 (450, H$_2$S)	~2–3 ML films (~10 nm)	–	2020[121]

W(N^{t}Bu)$_2$(NMe$_2$)$_2$ + H$_2$S plasma + Ar plasma	450	~6 nm rough films (24±2 nm)	–	2020[107]
W(N^{t}Bu)$_2$(NMe$_2$)$_2$ + H$_2$S plasma + H$_2$ plasma	450	~6 nm rough films (19±1 nm)	–	2020[107]
<u>W(N^{t}Bu)$_2$(NMe$_2$)$_2$ + H$_2$/H$_2$S plasma</u>	300	~8–65 nm rough films (~10–50 nm)	HER	2019[269]
<u>W$_2$(NMe$_2$)$_6$ + H$_2$S</u>	150 (400, H$_2$S)	~2–15 ML films (as-dep. amorp., ann. ~5–10 nm)	–	2019[134]
		WSe$_2$		
WCl$_6$ + H$_2$Se	390	~5 ML film (cryst.)	FET	2016[270] 2018[271]
WCl$_6$ + SeEt$_2$	600–800	1–5 ML films (200 nm)	FET	2016[272]
	700	3 ML film (cryst.)	gas sensor	2018[273]
	700	one to a few ML films (cryst.)	–	2019[178] 2018[274]
		ZrS$_2$		
<u>ZrCl$_4$ + H$_2$S</u>	350–450	a few–tens of ML films (~10–30 nm)	photodetector	2019[174]
	400	7 nm films (~10–40 nm)	–	2020[126]

a) Processes shown to have saturative reactions in at least one publication are <u>underlined</u>; b) For brevity, inert components (N$_2$, Ar) of reactive atmospheres are omitted; c) One TMDC monolayer (ML) corresponds to approximately 0.6 nm. Morphology is classified as flakes (discontinuous), films (continuous, smooth), or rough films. If the grain size was not indicated and could not be estimated from the provided information, the film is only denoted crystalline or amorphous; d) The year refers to the year the paper was assigned into an issue (if applicable); e) Claimed to be WCl$_5$ in the article, but is actually WCl$_6$ (R. Solanki, private communication).

Table 3. Summary of TMDC films produced by chalcogenization of ALD-grown films in alphabetical order. Abbreviations: amorphous (amorp.), annealed (ann.), as-deposited (as-dep.), crystalline (cryst.), field-effect transistor (FET), hydrogen evolution reaction (HER), photoelectrocatalysis (PEC), supercapacitor (SC).

Precursors [a]	Deposition T [°C] (post-treatment T [°C], atmosphere) [b]	Thickness and morphology (estimated grain size) [c]	Applications	Year[Ref.] [d]
$MoO_x \rightarrow MoS_2$				
$Mo(CO)_6 + O_3$	165 (600, S)	~10 nm rough films (cryst.)	HER	2013[275]
	160 (850, S)	3–4 ML film (~40 nm)	–	2016[276]
	140 (850, S)	~10 nm film (cryst.)	–	2019[277]
$Mo(CO)_6 + O_2$ plasma	200 (600 + 1000, H_2S)	1–5 ML films (~10–30 nm)	photodetector	2015[278]
	200 (200 + 600–1000, H_2S)	3–4 nm films (4–30 nm)	–	2020[279]
	165 (500–1000, S)	2 ML to 10 nm films (<10 nm at 500 °C to 50–200 nm at 1000 °C)	–	2019[280]
	155 (400, Ar + 500, S + 900, S)	1–4 ML films (~10 nm)	FET	2017[281]
	155 (400, Ar + 500, S + 900, S)	4 ML film	FET	2020[282]
	165 (200, H_2/H_2S)	~5 nm film	PEC	2019[283]
$Mo(N^tBu)_2(NMe_2)_2 + O_3$	300 (300 + 600 + 900–1000, S/H_2)	~5–10 nm films (cryst.)	–	2017[284]
$Mo(N^tBu)_2(NMe_2)_2 + O_2$ plasma	50 (900, H_2S)	1–8 ML films (~5–50 nm)	–	2020[125]
	150 (300 + 600 + 900–1000, S/H_2)	1 ML to 10 nm films (cryst.)	–	2017[284]
$Mo_{1-x}W_xOy \rightarrow Mo_{1-x}W_xS_2$				
$Mo(CO)_6 + O_2$ plasma & $WH_2(^iPrCp)_2 + O_2$ plasma	300 (600 + 1000, H_2S)	1–5 ML films (~10–30 nm)	photodetector	2015[278]
$MoO_x \rightarrow MoSe_2$				
$Mo(CO)_6 + O_2$ plasma	162 (820, Se/H_2)	2–8 ML films (~5–10 nm)	photodetector	2018[285]
	? (850, Se/H_2)	6 ML film (~5–10 nm)	photodetector	2019[286]
	162 (900, Se/H_2)	12–14 ML film (~5–10 nm)	photodetector	2018[287]
$SnO \rightarrow SnS_2$				
$Sn(dmamp)_2 + H_2O$	210 (350, H_2S + 350, H_2S plasma)	5 nm film (~a few tens of nm)	FET	2018[288]
$SnS \rightarrow SnS_2$				
$Sn(NMe_2)_4 + H_2S$	170 (450, H_2S)	20 and 40 nm films (ann. >40 nm)	FET	2018[289]
$TiN \rightarrow TiS_2$				
$Ti(NMe_2)_4 + N_2$ plasma	300 (300, S)	~75–120 nm films (~a few tens of nm)	SC	2017[290]

WOx → WS$_2$				
<u>WH$_2$(^{i}PrCp)$_2$ + O$_2$ plasma</u>	300 (1000, H$_2$S)	1–4 ML films (~10–20 nm)	FET	2013[291]
	300 (1000, H$_2$S)	1–4 ML films (cryst.)	gas sensor	2016[292]
<u>W(N^{t}Bu)$_2$(NMe$_2$)$_2$ + H$_2$O</u>	350 (500, S)	2–3 ML films (cryst.)	–	2019[200]
<u>W(N^{t}Bu)$_2$(NMe$_2$)$_2$ + O$_2$ plasma</u>	50 (900, H$_2$S)	~10 ML films (cryst.)	–	2020[125]
	150 (700, CS$_2$)	? (cryst.)	–	2016[293]
	160–220 (900, S/H$_2$)	1–4 ML films (cryst.)	FET	2018[294]
	40 or 300 (600 or 850, H$_2$S)	10–30 nm films (a few nm)	photonics	2018[295]

a) Processes shown to have saturative reactions in at least one publication are <u>underlined</u>; b) For brevity, inert components (N$_2$, Ar) of reactive atmospheres are omitted; c) One TMDC monolayer (ML) corresponds to approximately 0.6 nm. Morphology is classified as flakes (discontinuous), films (continuous, smooth), or rough films. If the grain size was not indicated and could not be estimated from the provided information, the film is only denoted crystalline or amorphous; d) The year refers to the year the paper was assigned into an issue (if applicable).

4. Applications of Atomic Layer Deposited Two-Dimensional Metal Dichalcogenides
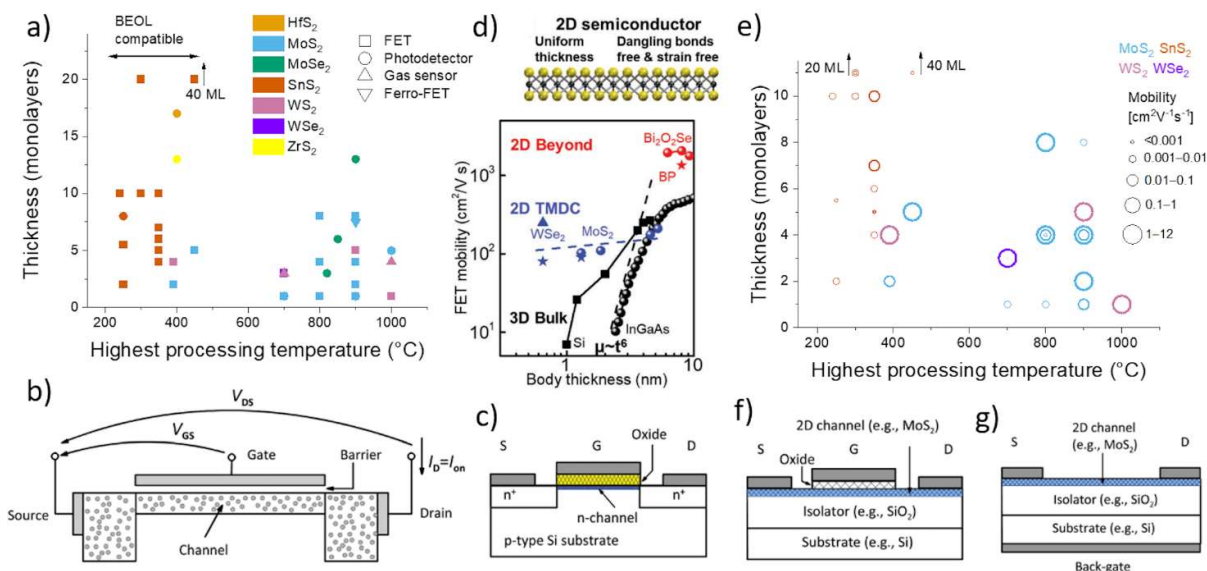
4.1. Electronics and Optoelectronics

Electronics and optoelectronics are among the most commonly studied applications of TMDCs due to their favorable properties as well as the importance of the microelectronics (semiconductor) industry. For (opto)electronic applications, typically only one to a few monolayers thick, continuous, high-quality TMDC films with a large grain size are preferred. Therefore, high deposition temperatures or high-temperature post-deposition annealing have often been used to prepare ALD TMDCs aimed for electronics (**Figure 10**a). Unfortunately, the high temperatures restrict compatibility with typical back-end-of-line (BEOL) semiconductor processing, for example, where temperatures should not exceed 400–500 °C. Thus, achieving high-quality TMDCs with large grain size, few defects, and little thickness variation between adjacent crystallites at low temperatures is the main challenge in electronics. In addition to often low deposition temperatures, the inherent conformality of ALD is an important asset in integrating ALD TMDCs into electronics.

If deposited at low enough temperatures, it is anticipated that TMDCs could be integrated onto existing silicon-based complementary metal oxide semiconductor (CMOS) platforms in BEOL for various functions, including transistors, photodetectors, lasers, and different gas, chemical, and biological sensors.[296] Therefore, these applications are also discussed here under electronics. In the emerging fields of flexible electronics and displays, the maximum temperature of polymer substrates range from below 100 to approximately 400 °C.[297–299]

Due to the lower melting point[114] and consequently higher diffusivity of SnS_2 compared to the sulfides of refractory metals MoS_2 and WS_2, for example, SnS_2 seems to be a promising material for electronic applications with a low thermal budget. There are also a few examples of well crystallized ALD MoS_2 and WS_2 films deposited at temperatures below 450 °C, and further efforts to this end are anticipated in the future.

For some applications or process flows in more distant future, such as possible replacement of silicon-based FETs, higher temperatures up to 1000 °C may be permitted. Furthermore, although a major

technological challenge, transfer of the TMDC films from the growth substrate to the target substrate is actively researched in the 2D community.[300,301] Nevertheless, even if the transfer process lifts the temperature restrictions, the high-temperature ALD processes will have to compete with more established (MO)CVD TMDC processes.

Figure 10. ALD TMDCs for FETs and other electronic applications. a) Overview of thickness and processing temperature of ALD TMDCs evaluated for electronic and optoelectronic applications (data from Table 2 and 3). b) Illustration of an FET (in on-state). c) Schematic structure of a conventional silicon FET. d) Illustration of the potential of 2D TMDCs for FETs with ultrathin channels (data points do not refer to ALD films, see Ref.[303] for more information and references). e) Mobility of ALD TMDC FETs (data from Table 4). Only studies where film thickness and processing temperature were indicated are included. Schematic structures of 2D FETs in f) top-gate and g) bottom-gate geometries. b,c,f,g) Reproduced under the terms of the CC-BY license.[302] Copyright 2015 Authors. Published by the Royal Society of Chemistry. d) Reproduced with permission.[303] Copyright 2018, The Royal Society of Chemistry.

4.1.1. Field-Effect Transistors

Overview:

FETs are perhaps the most important devices in commercial microelectronics, where the FET channel is usually silicon-based. An FET is a switch controlling the flow of current (either electrons or holes) between the source and drain electrodes by a voltage applied to a third, gate electrode (Figure 10b,c). The sizable band gaps of the semiconducting TMDCs enable efficient on-off switching of FETs.

Typical figures of merit used to assess the performance of FETs include field-effect charge carrier mobility μ and the ratio of the transistor on-state current to the off-state current I_{on}/I_{off}.[302,304] The off-current should be as low as possible for low power consumption, and the on-current and mobility as high as possible to enable fast switching.[304] While most TMDCs cannot reach as high mobilities as bulk silicon, their uniform structure free of dangling bonds means that they are less affected by decreases in channel length and thickness compared to 3D semiconductors such as silicon (Figure 10d). The shrinkage of channel dimensions (scaling) has been one of the main reasons behind the continuous improvements in the performance of microelectronics. TMDCs are considered among the candidates for continuing the scaling trend beyond silicon.

ALD MoS_2, SnS_2, WS_2, and WSe_2 films have been evaluated as FET channels, comprising the single most studied ALD TMDC application. The ALD TMDCs have, in the best cases, exhibited relatively high mobilities and very high I_{on}/I_{off} ratios (Figure 10e, **Table 4**). The rather good performance of the best reported devices is impressive considering the relatively small grain sizes of ALD TMDCs, as the grain size, or more specifically the grain boundary density, is often thought to be the main limiting factor for the TMDC transistor performance. Nevertheless, considering the gate length of only approximately 10 nm in the current state-of-art FETs,[302,305] it remains to be seen if large grain sizes are actually necessary for commercial highly scaled FETs. Excluding a report on ALD WSe_2 (Ref. [270]) with a mobility of several hundreds of $cm^2V^{-1}s^{-1}$, in the next best cases, mobilities on the order of 1–10 $cm^2V^{-1}s^{-1}$ have been achieved. Excellent I_{on}/I_{off} ratios up to 10^8 have been demonstrated for several ALD TMDC FETs, which are comparable to state-of-art TMDC FETs. However, achieving both good mobilities and large I_{on}/I_{off} ratios simultaneously has been relatively rare.

Most of the processes producing the best ALD TMDC FETs use high deposition or annealing temperatures of 700–1000 °C. High temperatures and post-deposition treatments in chalcogen atmosphere can considerably improve the film crystallinity, grain size, and stoichiometry, but such temperatures may not be permitted for many applications. Furthermore, at these high temperatures

ALD has to compete with many other methods. Therefore, the processes that result in high FET performance at temperatures below 500 °C deserve special attention and perhaps offer the best opportunities for ALD TMDC FETs. Low-temperature pre- and post-deposition treatments to improve performance form a promising approach deserving further study. Thickness also strongly affects the performance of TMDC FETs. It seems that for both ALD-grown (Table 4) and exfoliated TMDCs,[304] the highest on-currents and consequently mobilities are often obtained for layers thicker than a single monolayer, perhaps up to ten ML thick.

In addition to the TMDC grain size and thickness, the FET performance of ultrathin TMDCs is known to be sensitive to charge scattering at the interfaces with the substrate and dielectric layers, trap states, adsorbates, impurities and so forth.[306–308] Furthermore, contacting TMDCs is very difficult and typically Schottky contacts are formed due to Fermi level pinning.[309] Thus, the device geometry and structure are very important for the FET performance. One additional factor that complicates comparison between different studies is the lack of statistical data on device-to-device variation or yield in many studies.

In the device structure context, it is interesting to note that ALD is commonly used to deposit dielectric layers below and/or above the TMDC channel as both gate dielectric and encapsulation layers. The ALD-grown dielectrics have often been found to increase the mobility of the semiconducting channel.[310,311] ALD growth on TMDCs – a non-trivial process due to the inertness of TMDC basal planes – is beyond the topic of this review and has been reviewed previously.[312,313] Shang et al.[311] identified the improvement in mobility upon encapsulation to be due to a reduction of scattering by charged impurities (e.g. impurities, adsorbates, and interface traps), which often limit the mobility of TMDCs at room temperature. Such encapsulation can be provided by the gate dielectric for top-gate design (Figure 10f), but can also be beneficial for bottom-gate FETs (Figure 10g), where the encapsulation layer does not act as a gate dielectric.

With the discussion above in mind, we will go through the studied ALD TMDCs material by material, focusing on the observed correlations between the deposition conditions, material properties, and device structures with the FET performance.

MoS₂:

ALD MoS₂ films usually behave as n-type semiconductors, which means that they are turned on (off) by applying a positive (negative) gate voltage (the reverse is true for p-type semiconductors). The best ALD MoS₂ FET performance so far has been reported by Jeon et al.[118] for 5 ML MoS₂ films deposited using $Mo(CO)_6$ and EtSSEt at 250 °C followed by rapid thermal annealing in an Ar atmosphere at 450 °C for 30 s. Bottom gate FETs with an excellent mobility of 13.9 $cm^2V^{-1}s^{-1}$ (10.6±2.6 $cm^2V^{-1}s^{-1}$ over 9 devices) and a large I_{on}/I_{off} ratio of 10^8 were achieved by using an SEt_2 pretreatment dubbed inhibited ALD (iALD) to reduce the nucleation density (**Figure 11**a). In contrast, the conventional ALD process (cALD) without the pretreatment produced p-type films with inferior performance as shown in Figure 11b (mobility 0.004 $cm^2V^{-1}s^{-1}$, I_{on}/I_{off} 10^3). The difference was explained by the improvements in crystallinity and grain size in iALD films resulting from SEt_2 blocking some of the adsorption sites on the initial surface, which decreased the adsorption density of $Mo(CO)_6$ and consequently nucleation density of MoS₂ (Figure 11c,d). The achieved FET performance is remarkable for such a low deposition temperature and comparable to CVD MoS₂ deposited at 600 °C and above (see Ref. [314] and references therein). However, the process did not show ALD-like saturation, although uniform films and FET performance were achieved on 6" wafers.[118] Thus, it would be interesting to test such a surface-chemistry controlled iALD approach using a well-behaving ALD process.

In contrast to most other MoS₂ processes, Zhang et al.[218] deposited p-type MoS₂ films from $Mo(CO)_6$ and $S(SiMe_3)_2$ at 150 °C followed by annealing at 800 °C in a sulfur atmosphere. A rather high average (maximum) hole mobility of approximately 6 (11) $cm^2V^{-1}s^{-1}$ combined with a low I_{on}/I_{off}

ratio of 10^3 was measured for a 4 ML film. In the next study from the group, Wang et al.[197] used

$MoCl_5$ and $S(SiMe_3)_2$ precursors at 375 °C followed by annealing at 800 °C in a sulfur atmosphere,

resulting in n-type MoS_2 films. A good average mobility of 3.5 $cm^2V^{-1}s^{-1}$ but only a low I_{on}/I_{off} ratio

of 10^2 were achieved for a 8 ML MoS_2 film deposited on a GaN substrate, a substrate that necessitated

the top-gate FET design.
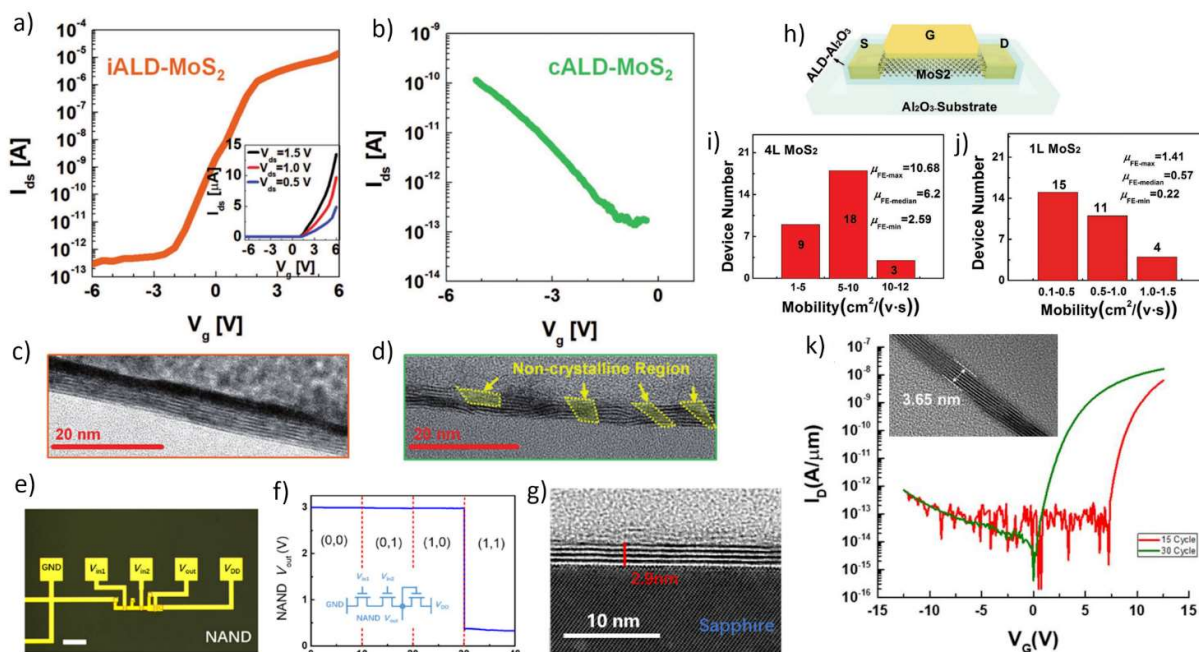
Figure 11. ALD MoS_2 FETs: drain current (I_{ds}) – gate voltage (V_g) plots of bottom-gate FETs using 5 ML a) iALD MoS_2 (drain-source voltage V_{ds} = 1.5 V) and b) cALD MoS_2 channel (V_{ds} = 10 V) and corresponding cross-sectional TEM images of c) iALD and d) cALD MoS_2 films. A logic NAND gate comprised of three ALD MoS_2 top-gate FETs: e) optical micrograph (scale bar 50 µm), f) output of the NAND gate (x axis in seconds), and g) cross-sectional TEM image of a 5 ML MoS_2 film used in the FETs. Top-gate FETs using a MoS_2 channel produced by sulfurization of an ALD MoO_x film with ALD-Al_2O_3 gate dielectric: h) schematic and mobility statistics of i) 4 ML and j) 1 ML MoS_2 devices. k) ALD SnS_2 FET: I_{ds}–V_g plots of bottom-gate FETs using 4 and 6 ML ALD SnS_2 channels deposited using 15 and 30 cycles with cross-sectional TEM image of the 6 ML SnS_2 film as an inset. a–d) Reproduced with permission.[118] Copyright 2017, WILEY-VCH Verlag GmbH. e–g) Reproduced with permission.[202] Copyright 2020, Tsinghua University Press and Springer-Verlag GmbH Germany, part of Springer Nature. h–j) Reproduced with permission.[281] Copyright 2017, WILEY-VCH Verlag GmbH. k) Reproduced with permission.[242] Copyright 2019, IOP Publishing Ltd.

In a follow-up work using the same $MoCl_5$+$S(SiMe_3)_2$ process, Liu et al.[202] produced both top-gate

FETs and different logic gates (Figure 11e,f) on sapphire. The authors observed that the annealing

time at 900 °C in sulfur atmosphere had a drastic effect on the FET performance. A 30 minute anneal resulted in a high mobility up to 10 $cm^2V^{-1}s^{-1}$ combined with a low I_{on}/I_{off} ratio of 10^3, which causes high power consumption. After a 120 minute annealing, the mobility decreased to 0.56 $cm^2V^{-1}s^{-1}$, but the I_{on}/I_{off} ratio increased to more than 10^6. A longer annealing time was found to improve the structural quality of the films (Figure 11g), which resulted in a decrease of both the on and off currents. This demonstrates that merely a high mobility is not sufficient for high performance FETs nor is it necessarily an indication of high film quality.

Using the same ALD process, Zhao et al.[199] deposited 5 nm thick MoS_2 films on SiO_2 of both planar and nanowire morphology. Top-gate transistors constructed on both substrates had comparable yet modest performance (mobility 0.01–0.02 $cm^2V^{-1}s^{-1}$ and I_{on}/I_{off} ratio of ~4×10^2), which is much lower compared to the aforementioned FETs on sapphire and GaN. This suggests that the substrate has a crucial effect during the growth and/or FET operation. Tian et al.[201] combined the same $MoCl_5$+$S(SiMe_3)_2$ process with a two-step annealing process, first in inert conditions at 800 °C to remove the chlorine left in the films followed by exposure to CS_2 at 400 °C in order to fill the sulfur vacancies. The CS_2 treatment improved the average mobility of the 4 ML MoS_2 films on sapphire from 0.009 to 0.48 $cm^2V^{-1}s^{-1}$ while the I_{on}/I_{off} ratio increased from approximately 5 to 500, which is still lower compared to the aforementioned results obtained using sulfur annealing.

The $MoCl_5$+$S(SiMe_3)_2$ process has thus been studied intensively for FETs and saturating growth characteristics of the process have recently been confirmed.[202] The successful demonstrations of inverters and logic NAND, AND, NOR, and OR gates using 2–5 MoS_2 FETs each show the potential of the process towards integrated circuits, although the high annealing temperature of 800–900 °C may limit its use.[198,202]

Browning et al.[176] used $MoCl_5$ and H_2S at 390 °C, reporting a mobility of 1 $cm^2V^{-1}s^{-1}$ for a 2 ML film on a SiO_2/Si bottom-gate structure. However, the I_{on}/I_{off} ratio was rather low at 10^3 and saturation of the ALD process was not demonstrated. Using the same precursors at a higher temperature of 800

41

°C, Kim et al.[177] achieved a mobility of 0.2 cm^{2}V^{-1}s^{-1} and a good I_{on}/I_{off} ratio of 10^8 for a 1 ML MoS$_2$ FET. In this case, the film thickness was observed to saturate to a single ML after a sufficient number of ALD cycles were applied. The authors denoted this mechanism self-limiting layer synthesis (SLS), which was explained to be due to the inert surface of TMDCs. Similar FET performance was later observed by the same group for a 1 ML MoS$_2$ film grown using MoF$_6$ and H$_2$S at 700 °C.[178] Interestingly, the MoF$_6$+H$_2$S process showed the typical saturative ALD characteristics in contrast to the SLS mechanism of the MoCl$_5$+H$_2$S process.

Shi et al.[281] sulfurized ALD MoO$_3$ films using a three-step procedure with steps at 400, 500, and 900 °C in Ar, S, and S atmospheres, respectively. The aim of the procedure was to maximize the crystallinity of the resulting MoS$_2$ films while preventing evaporation of MoO$_3$. The mobility of top-gate FETs fabricated on sapphire improved with increasing thickness from a median mobility of 0.57 cm^{2}V^{-1}s^{-1} for a single ML to 6.2 cm^{2}V^{-1}s^{-1} for 4 ML devices (Figure 11h–j). Moderate I_{on}/I_{off} ratios of approximately 10^4 and a rather small device-to-device variation were observed. Using an identical deposition and sulfurization procedure, Chen et al.[282] prepared both top- and bottom-gate FETs on a SiO$_2$/Si substrate and obtained average mobilities of 0.3 and 1.7 cm^{2}V^{-1}s^{-1}, respectively, using 4 ML MoS$_2$ films. The lower performance of the top-gate devices was attributed to the damage of the MoS$_2$ channel caused by H$_2$O used for the ALD Al$_2$O$_3$ gate dielectric.

SnS$_2$:

The reported performance of n-type ALD SnS$_2$ FETs is generally lower compared to MoS$_2$, especially in terms of mobility, although the latest studies have shown promise in improving the performance of SnS$_2$ FETs by pre- and post-treatments and use of a PEALD process. Advantageously, the temperatures used to prepare SnS$_2$ FETs are lower compared to most other TMDCs, from 250 to 450 °C, and good ALD characteristics have been confirmed for all of the processes. The limited mobility of ALD SnS$_2$ FETs seems somewhat surprising considering that exfoliated SnS$_2$ flakes have

shown performance comparable to MoS_2 (Ref. [315]) and because the ALD SnS_2 films appear to exhibit good crystallinity. Nevertheless, some of the ALD SnS_2 FETs have shown high I_{on}/I_{off} ratios, which combined with the low temperatures suggests them to be promising for flexible low-power electronics. Lee et al.[241] deposited a 12 nm (~20 ML) SnS_2 film by the most commonly used $Sn(NMe_2)_4$+H_2S process followed by annealing at 300 °C in a $S_2/H_2/Ar$ atmosphere to crystallize the films. The prepared FETs exhibited a modest I_{on}/I_{off} ratio of 390 and mobility of 0.0076 $cm^2V^{-1}s^{-1}$ on a SiO_2 substrate. However, the values increased to 6.4×10^3 and 0.06 $cm^2V^{-1}s^{-1}$, respectively, when the SnS_2 film was sandwiched between ALD-grown ZrO_2 layers. Choi et al.[289] observed that a 24 nm SnS_2 film produced by annealing a SnS film at 450 °C in a H_2S atmosphere exhibited a comparable I_{on}/I_{off} ratio (2×10^3) and mobility (0.014 $cm^2V^{-1}s^{-1}$).

More recently, Lee et al.[242] prepared thinner, 4 and 6 ML thick SnS_2 films using the $Sn(NMe_2)_4$+H_2S process combined with a lengthy multi-step annealing procedure in a H_2S/Ar atmosphere at 100 to 350 °C. The FETs exhibited high I_{on}/I_{off} ratios up to 8.3×10^6, whereas their mobilities were still relatively low, 0.06 and 0.08 $cm^2V^{-1}s^{-1}$ for the 4 and 6 ML films (Figure 11j). In a very recent study, Lee et al.[243] observed that a buffered oxide etch (BOE) treatment of SiO_2 substrates afforded slight improvements in the FET performance, i.e. a mobility of 0.31 $cm^2V^{-1}s^{-1}$ and an I_{on}/I_{off} ratio of 6.5×10^5 compared to 0.22 $cm^2V^{-1}s^{-1}$ and 2.9×10^5 on bare SiO_2. However, due to an increased growth rate, the film grown on BOE-treated SiO_2 was 10 ML thick compared to 7 ML on bare SiO_2, which can also affect its performance.

Mattinen et al.[99] deposited SnS_2 films using $Sn(OAc)_4$ and H_2S at 150 °C followed by H_2S/N_2 annealing at 250 °C. Despite large device-to-device variation, a clear improvement in performance with increasing film thickness from 2 to 5–6 ML was observed. The best 5–6 ML device with a mobility of 0.07 $cm^2V^{-1}s^{-1}$ and an I_{on}/I_{off} ratio of 4.8×10^7 was comparable to the films deposited by the $Sn(NMe_2)_4$+H_2S process.

Pyeon et al.[251] deposited SnS_2 films using $Sn(dmamp)_2$ and H_2S plasma at 150 to 240 °C. Although the film crystallinity improved with increasing deposition temperature, this was accompanied by transformation to rough, "flaky" morphology, which is unsuitable for FETs. The films deposited at 150 °C did not perform well as a FET either as-deposited or after post-deposition annealing at 240 °C. Therefore, to obtain well crystallized, smooth films, a two-step growth process was used: first, a nominally 1 ML thick SnS_2 seed layer was grown at 150 °C, onto which a thicker film was grown at 240 °C. Relatively good transistor performance was achieved (mobility 0.2 $cm^2V^{-1}s^{-1}$ and I_{on}/I_{off} ratio 2×10^6). A post-deposition annealing treatment at 300 °C increased the mobility to 0.8 $cm^2V^{-1}s^{-1}$ and decreased the I_{on}/I_{off} ratio to 10^6. Furthermore, as an important step towards use in flexible electronics, the authors prepared bottom-gate FETs on flexible polyimide substrates, which showed excellent uniformity with an average mobility of 0.57±0.02 $cm^2V^{-1}s^{-1}$ over 20 devices and a high I_{on}/I_{off} ratio of 10^6. The flexible devices remained operational after 2000 bending cycles to a radius of 17.5 mm. Pyeon et al.[288] also made SnS_2 films by sulfurization of ALD SnO at a rather low temperature of 350 °C. A thermal conversion using H_2S resulted in modest FET performance (mobility 0.0004 $cm^2V^{-1}s^{-1}$ and I_{on}/I_{off} ratio 10^3). Treating this film with a further H_2S plasma step improved the mobility and I_{on}/I_{off} ratio to 0.02 $cm^2V^{-1}s^{-1}$ and 10^5, respectively. Using only H_2S plasma without the preceding thermal conversion step resulted in a mixture of SnS and SnS_2. Furthermore, it was reported that SnO_2 films could not be effectively sulfurized. It is also worth noting that n-type SnS_2 can be rather easily transformed into p-type two-dimensional SnS and vice versa, which can be beneficial for fabrication of CMOS devices.[289,316,317]

WS₂:

WS_2 usually behaves as an n-type semiconductor that can display good FET performance as has also been observed for ALD WS_2 films. Browning et al.[258] reported n-type behavior with a mobility of 12 $cm^2V^{-1}s^{-1}$ for a 4 ML WS_2 film deposited using WCl_6 and H_2S at 390 °C. Multiple heterostructures

of alternating ALD n-type WS_2 (2.5 nm) and p-type SnS (4.5 nm) layers were also deposited. The heterostructures displayed ambipolar characteristics with hole and electron mobilities of 20 and 48 $cm^2V^{-1}s^{-1}$, respectively, and an I_{on}/I_{off} ratio of 10^5. While below the best exfoliated WS_2 flakes that exceed 200 $cm^2V^{-1}s^{-1}$ (Ref. [318]), the mobility values reported by Browning et al.[258] are on par with many reports of CVD WS_2 films and crystals deposited at high temperatures up to 1000 °C (see Ref. [319] and references therein).

ALD WS_2 films deposited by the WF_6+H_2 plasma+H_2S process have been integrated into a 300 mm BEOL compatible process flow at Imec.[128,262] Interestingly, in contrast to the usual n-type behavior of WS_2, the FETs were observed to be p-type. Extraction of mobility as well as a reliable estimation of the I_{on}/I_{off} ratio were prevented by back-gate leakage, although the latter was at least 10^5 for an optimized WS_2 film (thickness not reported). It is worth noting that this ALD process has been the subject of extensive studies focusing on the ALD growth and reaction mechanisms[100,261] as well as nucleation and grain growth.[111,124,128]

Song et al.[291] prepared top-gate FETs with a single ML thick WS_2 channel by sulfurization of ALD-grown WO_3 film at 1000 °C in a H_2S/Ar ambient. n-type behavior with a mobility of 3.9 $cm^2V^{-1}s^{-1}$ combined with a modest I_{on}/I_{off} ratio of 10^2–10^3 was observed in an early report from 2013. Later on, Zeng et al.[294] sulfurized ALD-grown WO_3 films at 900 °C to produce 5 ML thick WS_2 films, which exhibited a mobility of 4.4 $cm^2V^{-1}s^{-1}$ and an I_{on}/I_{off} ratio of 10^5.

WSe2:

WSe_2 is commonly reported to exhibit ambipolar behavior, i.e. it can be operated both as n- and p-type at positive and negative gate voltages, respectively, which is advantageous for use in CMOS chips. Browning et al.[270] grew few-layer ambipolar WSe_2 films using WCl_6 and H_2Se at 390 °C and achieved very high hole and electron mobilities of 354 and 531 $cm^2V^{-1}s^{-1}$ and an I_{on}/I_{off} ratio of 10^5. These mobility values exceed all previous reports of vapor-grown WSe_2 films and flakes (see Ref.

[38] and references therein) and even exfoliated flakes.[320] The highest mobilities were obtained using Pd contacts, whereas Au contacts resulted in slightly lower and Ti contacts in much lower mobilities (5 and 21 $cm^2V^{-1}s^{-1}$ for holes and electrons, respectively), which highlights the importance of optimizing TMDC contacts.[309] A further study by the same authors found the performance of the Pd-contacted devices to be in good agreement with DFT calculations.[271] Unfortunately, the ALD characteristics of the process have not been examined.

Table 4. FET performance of ALD-grown crystalline TMDCs. Abbreviations: BOE = buffered oxide etch, NW = nanowire, PI = polyimide.

Precursors	Deposition T [°C] (post-treatment T [°C], atmosphere) [a]	Device structure [b]	Thick.	Mobility [$cm^2V^{-1}s^{-1}$] [c]	n/p type	I_{on}/I_{off}	Year[Ref.]
		MoS₂					
MoCl₅ + H₂S	390	Ti/**MoS₂***/SiO₂/ Si(b)	2 ML	1	n	~10³	2015[176]
	800	(t)Au/Ti/Al₂O₃/**MoS₂***/SiO₂/Si	1 ML	0.2	n	10⁸	2016[177]
	420 (+900, Ar)	Au/Ti/**MoS₂***/Al₂O₃/SiO₂/Si(b)	2 ML	? ?	n n	~10 ~10⁴	2020[196]
MoCl₅ + S(SiMe₃)₂	375 (800, S)	(t)Au/Cr/Al₂O₃/**MoS₂***/GaN	8 ML	3.5 (2–4)	n	10²	2019[197]
	300 (900, S)	(t)Au/Cr/Al₂O₃/**MoS₂***/sapphire	5 ML	~3 (2.3–3.2)	n	~10³	2019[198]
	350 (900, S)	(t)Au/Cr/Al₂O₃/**MoS₂***/sapphire	4 ML	0.56 [d] 6.4 (~3–10) [e]	n n	>10⁶ 10³	2020[202]
	400 (900, S)	(t)Pt/Ti/HfO₂/Al₂O₃/**MoS₂***/SiO₂ NW (t)Pt/Ti/Al₂O₃/**MoS₂***/SiO₂/Si planar	~5 nm	0.02 0.01	n n	4.3×10² 3.5×10²	2020[199]
	375 (800, inert) (+ 400, CS₂)	(t)Pt/Cr/Al₂O₃/**MoS₂***/sapphire	4 ML	0.009 (0.002–0.014) 0.48 (0.12–0.75)	n n	~5 5×10²	2019[201]
MoF₆ + H₂S	700	Au/Ti/**MoS₂***/ SiO₂/Si(b)	1 ML	0.1	n	10⁶	2019[178]
Mo(CO)₆ + EtSSEt	250 (450, Ar)	Au/Ti/**MoS₂***/ SiO₂/Si(b)	5 ML	10.6±2.6 [f] 0.004 [g]	n p	10⁸ 10³	2017[118]
Mo(CO)₆ + S(SiMe₃)₂	150 (800, S)	(t)Au/Cr/Al₂O₃/**MoS₂***/sapphire	4 ML	~6 (2–11)	p	10³	2018[218]
Mo(NMe₂)₄ + H₂S	80 (1000, S)	?	?	0.23	n	10²	2017[226]
		MoO₃ →MoS₂					
Mo(CO)₆ + O₂ plasma	155 (400, Ar + 500, S + 900, S)	(t)Au/Cr/Al₂O₃/**MoS₂***/sapphire	1 ML 2 ML 4 ML	0.57 (0.22–1.41) 1.5 (0.7–2.4) 6.2 (2.6–10.7)	n n n	10⁴ 10⁴ 5×10³	2017[281]
	155 (400, Ar + 500, S + 900, S)	(t)Au/Cr/Al₂O₃/**MoS₂***/SiO₂/Si Au/Cr/**MoS₂***/ SiO₂/Si(b)	4 ML 4 ML	0.31 (0.09–0.84) 1.7 (0.25–5.6)	n n	10⁵ >10³	2020[282]
		SnS₂					
Sn(NMe₂)₄ + H₂S	150 (300, S/H₂)	Au/Ni/**SnS₂***/ SiO₂/Si(b) Au/Ni/**SnS₂***/ ZrO₂/SiO₂/Si(b)	12 nm	0.0076 0.011	n n	3.9×10² 6.2×10²	2017[241]

WILEY-VCH

Precursor	Temperature	Structure	Thickness	Mobility	Type	On/off	Year
		Au/Ni/ZrO$_2$*/ **SnS$_2$**/ZrO$_2$/ SiO$_2$/Si(b)		0.06	n	6.4×10^3	
	150 (100–350 (multi-step), H$_2$S)	Au/Ni/**SnS$_2$***/SiO$_2$/Si(b)	4 ML	0.06	n	10^5	2019[242]
			6 ML	0.08	n	8.3×10^6	
	150 (100–350 (multi-step), H$_2$S)	Au/Ni/**SnS$_2$***/SiO$_2$/Si(b)	7 ML	0.22	n	2.9×10^5	2019[243]
		Au/Ni/**SnS$_2$***/SiO$_2$/Si(b) (BOE-treated)	10 ML	0.31	n	6.5×10^5	
Sn(OAc)$_4$ + H$_2$S	150 (250, H$_2$S)	?/**SnS$_2$***/SiO$_2$/Si(b)	2 ML	0.009	n	7.5×10^5	2020[70]
			5–6 ML	0.07	n	4.8×10^7	
Sn(dmamp)$_2$ + H$_2$S plasma	150 + 240 (+ 300, H$_2$S)	Au/Ti/**SnS$_2$***/SiO$_2$/Si(b)	10 ML	0.2 [h]	n	2×10^6	2019[251]
				0.8 [i]	n	10^6	
		Au/Ti/Al$_2$O$_3$*/**SnS$_2$***/Al$_2$O$_3$*/PI/Ti/Au(b)	10 ML	0.57±0.02 [i]	n	10^6	

SnS →SnS$_2$

| Sn(NMe$_2$)$_4$ + H$_2$S | 170 (450, H$_2$S) | Au/Ni/**SnS$_2$***/SiO$_2$/Si(b) | 24 nm | 0.014 | n | 2×10^3 | 2018[289] |

SnO →SnS$_2$

| Sn(dmamp)$_2$ + H$_2$O | 120 (350, H$_2$S) (+350, H$_2$S plasma) | Au/Ti/**SnS$_2$***/Al$_2$O$_3$/SiO$_2$/Si(b) | 5 ML | 0.0004 | n | 10^3 | 2018[288] |
| | | | | 0.02 | n | 10^5 | |

WS$_2$

| WCl$_6$ + H$_2$S | 390 | Au/Ti/**WS$_2$***/SiO$_2$/Si(b) | 4 ML | 12 | n | ~10^4 | 2015[258] |
| WF$_6$ + H$_2$ plasma + H$_2$S | 450 | Mo/Al$_2$O$_3$/**WS$_2$***/SiO$_2$/Si(b) | ? | - | p | >10^5 | 2018[111] |

WO$_3$ → WS$_2$

| WH$_2$(^{i}PrCp)$_2$ + O$_2$ plasma | 300 (1000, H$_2$S) | (t)Au/Ti/HfO$_2$*/**WS$_2$***/SiO$_2$/Si | 1 ML | 3.9 | n | 10^2–10^3 | 2013[291] |
| W(N^{t}Bu)$_2$(NMe$_2$)$_2$ + O$_2$ plasma | 180 (900, S/H$_2$) | Au/**WS$_2$***/SiO$_2$/Si(b) | 5 ML | 4.5 | n | 10^5 | 2018[294] |

WSe$_2$

WCl$_6$ + H$_2$Se	390	Pd/**WSe$_2$***/SiO$_2$/Si(b)	?	354/531 [j]	p/n	10^5	2016[270]
		Ti/**WSe$_2$***/SiO$_2$/Si(b)		5/21 [j]	p/n		
WCl$_6$ + SEt$_2$	700	Pd/**WSe$_2$***/SiO$_2$/Si(b)	3 ML	2.2	p	10^5	2016[272]

[a] For brevity, inert components (N$_2$, Ar) of reactive atmospheres are omitted; [b] The structure is listed from top (electrodes) to bottom (substrate). The TMDC channel is **bolded** and ALD-grown layers are indicated by an asterisk (*). The gate is marked by t (top gate) or b (bottom gate); [c] The mobility values in parenthesis represent the device-to-device variation, if reported; [d] 120 min annealing; [e] 30 min annealing; [f] SEt$_2$ pretreatment; [g] No pretreatment; [h] As-deposited; [i] Annealed; [j] Hole/electron (p-type/n-type) mobility.

4.1.2. Photodetectors

ALD TMDCs have also been studied as photodetectors, which are important components for many modern and future technologies from biomedical imaging, digital cameras, and internet of things to optical communications.[321,322] Obviously, different end uses require photodetectors operating at different wavelengths and with different characteristics. Out of the many photodetector performance indicators, the most common is photoresponsivity (R), which is defined as the measured photocurrent (*I*) divided by the power of the incident light (*P*).[321,322] The response speed is also crucial and commonly quantified as the rise (decay) time defined as the time to reach 90% (10%) of the photocurrent after the light source is turned on (off).

There are different types of photodetectors, including photodiodes, photoresistors, phototransistors, photothermoelectrics, and bolometers depending on the structure and mechanism of operation.[322] The first two have been examined for ALD TMDCs (**Table 5**). Photodiodes, which can operate without an external bias, have been constructed using 1 ML thick MoS_2 films grown on a 2 ML WSe_2 flake[177] or on graphene[178], resulting in photoresponsivities of 33 and 241 mA W^{-1}, respectively.

Most of the examined devices are photoresistors (photoconductors), in which photogenerated charge carriers are separated by an external electric field applied between two electrodes, resulting in a measurable photocurrent.[321] Mattinen et al.[174] demonstrated photoresistors consisting of HfS_2 and ZrS_2 films capped with a protective $Al_xSi_yO_z$ layer (**Figure 12**a). Responsivity values of 0.18 and 50 mA W^{-1} for 405 nm light were observed for HfS_2 and ZrS_2 under typical measurement conditions. The use of a higher bias voltage and a lower laser power density increased the responsivity of ZrS_2 up to 1.25 A W^{-1}. Mattinen et al.[70] performed also preliminary studies using SnS_2 films as photoresistors. The photoresponsivity of the SnS_2 devices on soda lime glass was low (20–40 µA W^{-1} for 450 nm light).

Song et al.[278] constructed photoresistors using 5 ML thick MoS$_2$, WS$_2$ and Mo$_{1-x}$W$_x$S$_2$ alloy films with a vertically graded composition that were obtained by sulfurization of respective oxide films using a two-step H$_2$S-treatment at 600 and 800 °C. The highest responsivity for white light was obtained using the graded alloy, although no performance indicators were calculated.
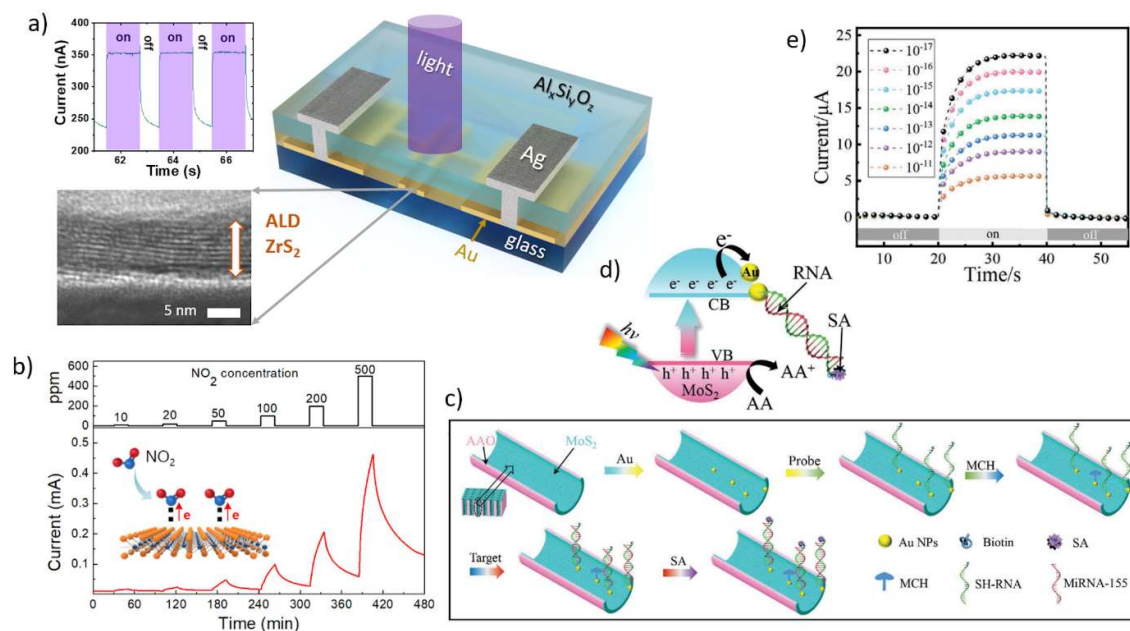
Figure 12. a) Photodetector with an 8 nm ALD ZrS$_2$ film including the photodetector output (current) and cross-sectional TEM image of the ZrS$_2$ film. b) Schematic and output of a NO$_2$ gas sensor based on a 3 ML ALD WSe$_2$ film. MoS$_2$-based biosensor: c) schematic of sensor fabrication (AAO = anodic aluminum oxide, MCH = 6-mercaptohexanol, SA = streptavidin), d) schematic of operation (AA = ascorbic acid, CB = conduction band, VB = valence band), and e) sensor response (current) to different concentrations of microRNA-155 under 450 nm illumination. a) Reproduced under the terms of the CC-BY license.[174] Copyright 2019 Authors. b) Reproduced with permission.[273] Copyright 2018, American Chemical Society. c–e) Reproduced with permission.[188] Copyright 2020, WILEY-VCH Verlag GmbH.

Dai and coworkers published a series of reports[285–287] on MoSe$_2$ photodetectors prepared by selenizing ALD-grown MoO$_3$ films at 820 to 900 °C in a Se/H$_2$/Ar atmosphere. While there were some differences in the selenization process, it seems that the main explanation for the different performance was the change in the film thickness. In comparable measurement conditions, the responsivity increased from 8.6 to 859 to 1300 mA W^{-1} with the thickness increasing from 3 to 6 to 13 ML. It should be noted that a much larger responsivity of 100 A

W^{-1} was also measured at a much lower incident power (0.026 versus 0.4 mW cm^{-2}). The observed increase of photoresponsivity with decreasing incident power is very strong even for a 2D material, for which such a phenomenon is typical. Often, the strong dependence of responsivity on incident power is attributed to presence of traps and defects in the films, which enable a very high responsivity at a low light intensity.[323,324]

Comparison of the performance of ALD TMDC photodetectors to each other as well as to the literature is complicated by the large variation in the literature results (e.g. for single ML MoS$_2$ photodetectors photoresponsivities from 10^{-3} to 10^4 A W^{-1} have been reported)[322] and measurement conditions, such as the incident light intensity and wavelength and the electric field between the electrodes. In general, it seems that the the photoresponsivities and response times of the ALD TMDC photodetectors lay around the middle range of values reported for 2D TMDC photodetectors.[321,322,325] There is therefore potential to further improve their performance, for example by increasing light absorbtion using thicker films or films of direct band gap material ReS$_2$ or perhaps three-dimensional substrates. Improvement of film quality should be pursued especially to obtain more quickly responding photodetectors. However, the presence of defects may even be beneficial to increase photoresponsivity at the cost of response time via a photogating mechanism.[323]

Table 5. Photodetector performance of ALD-grown TMDCs. All of the examined films were crystalline. Abbreviations: IDE = interdigitated electrode, R = photoresponsivity, SLG = soda lime glass.

Precursors	Deposition T [°C] (post-treatment T [°C], atmosphere) [a]	Device structure [b]	Thickness	R [mA W^{-1}]	Field [V m^{-1}] [c]	λ [nm] / P [mW cm^{-2}]	Rise / decay time [ms]	Year [Ref.]
			HfS$_2$					
HfCl$_4$ + H$_2$S	400	(r) Al$_x$Si$_y$O$_z$*/**HfS$_2$***/Au/SLG	10 nm	0.18	3.3×10^4	405 / 22	<100 / 300	2019[174]
			MoS$_2$					
MoCl$_5$ + H$_2$S	900	(d) Au/Ti/**MoS$_2$***/**WSe$_2$**/SiO$_2$/Si	1 ML	33	?	? / 1.4	?	2016[177]
MoF$_6$ + H$_2$S	700	(d) Au/Ti/**MoS$_2$***/**graphene**/SiO$_2$/Si	1 ML	241	2.5×10^4	650 / 4×10^5	?	2019[178]
			Mo$_{1-x}$W$_x$O$_y$ → Mo$_{1-x}$W$_x$S$_2$					
Mo(CO)$_6$ + O$_2$ plasma & WH$_2$(^{i}PrCp)$_2$ + O$_2$ plasma	300 (600 + 1000, H$_2$S)	(r) Au/Ti/**Mo$_{1-x}$W$_x$S$_2$***/SiO$_2$/Si	5 ML	?	5×10^4	white light	?	2015[278]
			MoO$_3$ → MoSe$_2$					
Mo(CO)$_6$ + O$_2$ plasma	162 (820, Se/H$_2$)	(r) Au/Ti/**MoSe$_2$***/SiO$_2$/Si	3 ML	8.6	10^6 (IDE)	638 / 40	50 / 50	2018[285]
	? (850, Se/H$_2$)	(r) Au/Ti/**MoSe$_2$***/SiO$_2$/Si	6 ML	859	10^6 (IDE)	638 / 40	40 / 38	2019[286]
	162 (900, Se/H$_2$)	(r) Au/Ti/**MoSe$_2$***/SiO$_2$/Si	13 ML	1×10^5 / 1.3×10^3	10^6 (IDE) / 10^6 (IDE)	638 / 0.026 / 638 / 40	40 / 22	2018[287]
			SnS$_2$					
Sn(OAc)$_4$ + H$_2$S	150 (250, H$_2$S)	(r) Au/**SnS$_2$***/SLG	5 nm	3×10^{-2}	1.7×10^5	450 / 22	?	2020[70]
			ZrS$_2$					
ZrCl$_4$ + H$_2$S	400	(r) Al$_x$Si$_y$O$_z$*/**ZrS$_2$***/Au/SLG	8 nm	50 / 1.25×10^3	3.3×10^4 / 1.7×10^5	405 / 22 / 405 / 0.087	35 / 230 / 840 / 840	2019[174]

[a] For brevity, inert components (N$_2$, Ar) of reactive atmospheres are omitted; [b] The structure is listed from top to bottom (substrate). The absorber layers are **bolded** and ALD-grown layers are indicated by an asterisk (*). Device type is indicated by r (photoresistor) or d (photodiode); [c] Field represents the electric field between electrodes calculated from the applied bias and electrode separation, which has a strong effect on photoresponsivity.

4.1.3. Gas sensors

In addition to FETs and photodetectors, ALD TMDCs have been studied as chemoresistive gas sensors (**Table 6**), which exhibit a change of resistance upon a change in the atmosphere and gases present. Most of the studies have focused on detection of NO_2, a toxic gas emitted to the atmosphere from combustion of fossil fuels that is harmful even at levels below 1 ppm.[326] An important part of gas sensor studies is to examine cross-sensitivity to other gases, which should ideally be low. In addition, useful gas sensors should respond and recover quickly during and after exposure to changes in atmosphere and should preferably be operated at low temperatures or even room temperature.

The change in conductivity in TMDC sensors is thought to be due to mainly charge transfer caused by physisorption of gas molecules. For example, on adsorption of electron-withdrawing (oxidizing) NO_2, electrons are transferred from the TMDC to NO_2, which increases the resistance of n-type semiconductors. Electron-donating (reducing) gases, such as acetone, decrease the resistance of n-type TMDCs. For p-type TMDCs, the situation is reversed. Therefore, the major carrier type of the sensor and the nature of the gases have to be taken into account when evaluating gas sensor characteristics, such as response (see Table 6 for both results and definitions). Advantageously, the low thickness and large surface area of TMDCs can result in extremely high sensitivity compared to conventional gas sensors.[327]

In the first demonstration of an ALD TMDC gas sensor, Ko et al.[292] prepared 1 to 4 ML thick WS_2 sensors by sulfurizing ALD WO_3 films at 1000 °C under an Ar/H_2S ambient. The 4 ML sensor exhibited the highest responses of 52% and –105% against 500 ppm NO_2 and 10 ppm acetone, respectively. The response to NO_2 increased 12-fold when the sensor was functionalized by silver nanowires, which was attributed to catalytic effects on adsorption of NO_2 on the nanowires, while the response to acetone decreased slightly.

In another study, Ko et al.[336] achieved a high response of 4140% against 500 ppm of NO_2 using a three-monolayer WSe_2 film deposited by the WCl_6+SEt_2 SLS process (Figure 12b). The

observed slow recovery (>85 min) of the sensor at room temperature was improved by either increasing the operation temperature from room temperature to 100 °C (21.5 min) or more dramatically by adding NH_3 in the purge gas (43 s), both of which accelerated removal of adsorbed NO_2. It is to be noted that the sensor also exhibited a strong response of opposite sign toward NH_3, namely –1750% against 500 ppm of NH_3.

Functionalization of TeO_2 nanowires by ALD SnS_2 has also been explored for gas sensors toward NO_2, H_2S, NH_3, and SO_2. However, in this case the SnS_2 coating led to a decrease of response compared to the pristine nanowires.[245] The decrease may be due to the p-type nature of TeO_2 in contrast to n-type SnS_2 (the overall sensor response toward NO_2 was p-type) and unfavorable energy alignment between TeO_2 and SnS_2, among other factors.

Pyeon et al.[252] used the $Sn(dmamp)_2$+H_2S plasma process to grow SnS_2 films that were used as flexible NO_2 sensors. Coating the polyimide substrate with ALD Al_2O_3 prior to the SnS_2 growth transformed the morphology of the SnS_2 films from smooth to rough. The rough films exhibited improved response compared to smoother films deposited at lower temperatures or directly on polyimide. Response as high as 30 900% against 1 ppm of NO_2 and an estimated limit of detection as low as 0.29 ppt were reached. The sensor exhibited excellent selectivity (low response) against several reducing gases.

The response of the SnS_2 sensor toward NO_2 was very high compared to the other sensors discussed here as well as other TMDC and metal oxide based NO_2 sensors reported in literature (Refs.[252,326] and references therein). However, although the response time was not studied in detail, it is apparent that the slow response of the ALD SnS_2 sensor as well as most of the other sensors discussed here needs to be improved in the future. Considering that many ALD TMDC processes produce rough films, ALD should be a promising method for preparing gas sensors. Testing more ALD films of different materials, thicknesses, and morphologies as gas sensors in the future is encouraged.

Table 6. Gas sensor performance of crystalline ALD-grown TMDCs. Abbreviations: IDE = interdigitated electrode, NW = nanowire, RT = room temperature.

Precursors	Deposition T [°C] (post-treatment T [°C], atmosphere) [a]	Structure [b]	Thick-ness	Gas, concentration [ppm]	Response [%] [c]	n/p, Oper-ating T [°C]	Year [Ref.]
			SnS$_2$				
Sn(dmamp)$_2$ + H$_2$S plasma	240	Au/Ti(IDE)/**SnS$_2$***/Al$_2$O$_3$*/PI	? nm	NO$_2$, 1	30 900	n, RT	2020[252]
				NO$_2$, 0.1	3 000		
				H$_2$, 1	−3		
				Acetone, 1	−9		
				Ethanol, 1	−8		
				NH$_3$, 1	−14		
				H$_2$S, 1	−41		
				CO, 10	0		
	210	Au/Ti(IDE)/**SnS$_2$***/Al$_2$O$_3$*/PI		NO$_2$, 1	10 900		
	180	Au/Ti(IDE)/**SnS$_2$***/Al$_2$O$_3$*/PI		NO$_2$, 1	4 100		
	240	Au/Ti(IDE)/**SnS$_2$***/PI		NO$_2$, 1	4 200		
Sn(NMe$_2$)$_4$ + H$_2$S	150 (350, H$_2$S)	Au/Ti(IDE)/**SnS$_2$***/TeO$_2$ NW/Si	~50 nm	NO$_2$, 10	1.8	p, 50	2019[245]
				H$_2$S, 10	~1		
				NH$_3$, 10	~1.5		
				SO$_2$, 10	~0.3		
		Au/Ti(IDE)/TeO$_2$ NW/Si		NO$_2$, 10	10.6		
			WO$_3$ → WS$_2$				
WH$_2$(iPrCp)$_2$ + O$_2$ plasma	300 (1000, H$_2$S)	Au/Cr/**WS$_2$***/SiO$_2$/Si	1 ML	NO$_2$, 500	16	p, 100	2016[292]
				Acetone, 10	−44		
			4 ML	NO$_2$, 500	52		
				Acetone, 10	−105		
		Au/Cr/Ag NW/**WS$_2$***/SiO$_2$/Si	4 ML	NO$_2$, 500	667		
				Acetone, 10	−54		
			WSe$_2$				
WCl$_6$ + SEt$_2$	700	Pd(IDE)/**WSe$_2$***/SiO$_2$/Si	3 ML	NO$_2$, 400	4140	p, RT	2018[273]
				NO$_2$, 10	162		
				NH$_3$, 500	−1750		
				CO$_2$, 500	−61		
				Acetone, 10	−20		
				NO$_2$, 400	~3000	100	

[a] For brevity, inert components (N$_2$, Ar) of reactive atmospheres are omitted; [b] The structure is listed from top (electrode) to bottom (substrate). The sensing layers are **bolded** and ALD-grown layers are indicated by an asterisk (*) in the structure; [c] The response of n-type sensors for oxidizing gases was defined as $((R_g–R_0)/R_0)\times100\%$ (alternately written as $((I_0–I_g)/I_g)\cdot100\%$) whereas the formula $((R_0–R_g)/R_g)\times100\%$ was used for reducing gases (R_g and R_0 represent the resistance upon exposure to the analyte gas and the baseline resistance, respectively). For p-type semiconductors, the first formula was used for reducing gases and the second for oxidizing ones.

4.1.3. Biosensors

TMDCs are promising materials for selective and sensitive detection of various biomolecules.

Different approaches including electrochemical, photoelectrochemical (PEC), FET-based, and

optical sensors have been reported in the 2D literature.[328,329] For ALD TMDCs, MoS$_2$ and

MoS$_2$-ReS$_2$ heterostructures were recently used as PEC biosensors to detect specific microRNA

molecules considered as biomarkers for cancer. The PEC biosensors can also be viewed as advanced photodetectors.

Taking advantage of the excellent conformality of ALD, Jiao et al.[188] prepared rough MoS_2 films on high-surface area anodic aluminum oxide (AAO) substrates using $MoCl_5$ and H_2S. In order to achieve sufficient sensitivity and selectivity, gold nanoparticles were evaporated on top of the MoS_2 films followed by addition of a thiol-terminated RNA probe (SH-RNA) that binds to Au from the thiol end and selectively interacts with the miRNA-155 analyte via complementary bases (Figure 12c). After exposure to the analyte, unreacted Au nanoparticles were capped with 6-mercaptohexanol (MCH) and the formed miRNA155-SH-RNA complementary RNA strands with streptavidin (SA) to prevent false positives. The amount of miRNA-155 could then be determined by measuring the photocurrent upon illumination by a 450 nm laser in a solution containing 0.1 M ascorbic acid (AA) and 0.1 M KCl. The photocurrent decreased due to the adsorbed miRNA-155, which can be understood by steric hindrance on the surface caused by the adsorbed macromolecules preventing AA from reaching the rough electrode surface (Figure 12d,e). Linear response (decrease of photocurrent) was achieved in the range of 0.01 fM to 0.01 nM of miRNA-155, while the detection limit was as low as 3 aM for the optimized device. These values are excellent compared to previously reported sensors.[188] The sensor was also shown to be highly selective even against a RNA strand where only one base was changed to a non-complementary one. Finally, successful quantitative detection of miRNA-155 from human serum was demonstrated, which is an important step toward practical applications.

In another report from the same group, Liu et al.[189] fabricated MoS_2-ReS_2 based biosensors on indium tin oxide substrates. Interestingly, despite pulsing both $MoCl_5$ and $ReCl_5$ during the same cycle at 400 °C, it was claimed that MoS_2-ReS_2 heterostructures were formed instead of $Mo_{2-x}Re_xS_2$ alloys. The formation of heterostructures was speculated to increase charge carrier lifetimes, which improves the sensitivity of the biosensor. Indeed, the photocurrent of the

optimized sample containing approximately 70% ReS_2 with 30% MoS_2 was 7 and 59 times higher compared to pure ReS_2 and MoS_2, respectively, before functionalization. Using a similar functionalization of the sensor described above but with a different probe strand, the biosensor was designed to be selective toward miRNA-21, which has three different bases compared to miRNA-155. A very broad linear range from 10 aM to 1 nM was achieved with a detection limit of 2.8 aM along with good selectivity against miRNA-155 and other related miRNA molecules.

4.2. Electrocatalysis and Photocatalysis

ALD TMDCs have been studied for electrocatalytic, photoelectrocatalytic (PEC), and photocatalytic applications (**Figure 13**a and **Table 7–9**). In most cases, films from a few to 50 nm thick that have been deposited at relatively low temperatures of 300 °C or less have been used. The low crystallinity or even amorphous nature of the films is often beneficial for catalytic applications. In many cases, the TMDC films have been deposited on high aspect ratio substrates to improve the catalyst performance. The excellent conformality and scalability of ALD are valuable assets for preparation of TMDC catalysts. ALD TMDCs also hold promise in producing cost-effective catalysts, although further efforts to this end are needed. Better understanding of process-structure-performance relations of ALD TMDC electrocatalysts is also necessary. The most studied catalytic application of ALD TMDCs has been the electrocatalytic water splitting with a smaller number of studies on photoelectrochemical catalysis (usually water splitting using TMDCs in combination with bulk semiconductors) as well as photocatalysis.
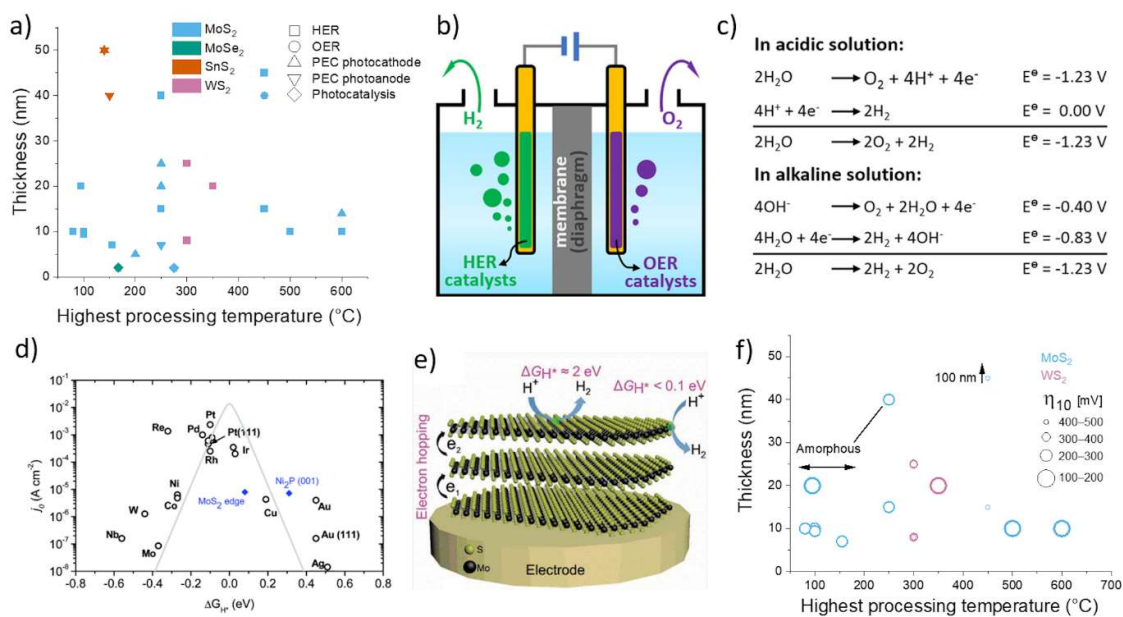
Figure 13. a) Overview of thickness and processing temperature of ALD TMDCs evaluated for electrocatalytic and photocatalytic applications (data from Table 2 and 3). b) Schematic of a conventional electrolytic water splitting device (electrolyzer). c) OER (top row), HER (middle row), and total (bottom row) water splitting reactions and the corresponding thermodynamic potentials (E^0, versus reversible hydrogen electrode RHE) in acidic and alkaline conditions.[330] d) HER volcano plot of exchange current density j_0 illustrating inherent catalytic activity of MoS_2 and several metals as a function of the DFT-calculated Gibbs free energy of adsorbed atomic hydrogen (ΔG_H).[331] e) Schematic of ΔG_H on basal planes and edges of MoS_2 and the required electron hopping between MoS_2 layers.[332] f) Overpotential η_{10} of ALD TMDC HER electrocatalysts (data from Table 7). Only studies where film thickness and processing temperature were reported are included. b,c) Reproduced with permission.[330] Copyright 2018, American Chemical Society. d) Reproduced with permission.[331] Copyright 2014, The Royal Society of Chemistry. e) Reproduced with permission.[332] Copyright 2020, WILEY-VCH Verlag GmbH.

4.2.1. Electrocatalytic Water Splitting: Hydrogen Evolution Reaction

In the electrocatalytic water splitting, water is broken down into hydrogen and oxygen gases (Figure 13b). The reduction of H^+ at the cathode is called hydrogen evolution reaction (HER), while the oxidation of O^{2-} at the anode is termed oxygen evolution reaction (OER). Highly conductive electrolytes are beneficial for electrolysis, so water splitting is usually performed in either strongly acidic or alkaline conditions, which affects the reactions taking place (Figure 13c). In early stage research, such as the studies discussed here, HER is usually performed in acidic conditions and OER in alkaline conditions, which results in integration challenges for practical applications.[330–334]

Hydrogen is by far the more valuable of the two gases produced. H_2 is currently mainly produced by natural gas reforming.[335] Hydrogen produced by electrolytic water splitting using renewable electricity, such as wind or solar electricity, has great potential to replace or at least supplement the hydrogen of fossil fuel origin for chemical industry. Furthermore, burning hydrogen in fuel cells ("water splitting in reverse") enables the use of H_2 as a clean fuel for transportation and to balance the intermittent electricity production from renewable sources.[333,335]

Effective electrocatalysts are required to improve the reaction kinetics of both HER and OER. An increased activity corresponds to a decrease of the overpotential η above the minimum thermodynamic potential of 1.23 V that needs to be applied in order to achieve a sufficient hydrogen/oxygen production rate (current density). The first step of HER is the reductive adsorption of a proton onto the catalyst (Volmer step), which is followed by either a reaction between the adsorbed hydrogen atom with a proton (Heyrovsky step) or between two adsorbed hydrogen atoms (Tafel step) producing H_2. It is commonly accepted that an ideal HER catalyst should have an atomic hydrogen adsorption energy (ΔG_H) that is close to zero, which results in a large exchange current density j_0 (current density at the thermodynamic potential). Using this metric, it can be seen that TMDCs such as MoS_2 are promising cost-effective alternatives to the platinum-group metals, which are the best known HER electrocatalysts (Figure 13d).[331,333,334,336]

Two additional figures of merit for HER that we will use in our discussion throughout the section are the overpotential η needed to reach a current density of 10 mA cm^{-2} (denoted η_{10}) as well as the Tafel slope, i.e. the increase in overpotential required to increase the current density by an order of magnitude. For high HER activity, the exchange current density should be as large as possible, whereas both the overpotential and Tafel slope should be as small as possible.[337]

For applications that require high current densities, such as current commercial electrolyzers ($1–10$ A cm^{-2}), the Tafel slope is the most important metric, whereas for low current density applications, including PEC HER ($\sim5–20$ mA cm^{-2}), a high j_0 is more important.[333] Obviously, the stability of the catalyst in the harsh operating conditions is also crucial and becomes even more important for OER that is run in strongly oxidizing conditions.[331,333] For TMDCs, the cost of the elements is generally not an issue unlike with the platinum group metals, yet cost-effective deposition methods are necessary.

The unsaturated edge sites, in particular metal atoms, of TMDCs have small ΔG_H and have been identified as the active sites for HER, whereas the basal planes have a large ΔG_H due to their inert nature and are usually inactive toward HER (Figure 13e).[27,331,338] Rough or porous and nanocrystalline, highly defective or even amorphous TMDC films generally exhibit the largest density of active sites and therefore the highest activity,[331,332,336,337,339] which is also apparent in the ALD TMDC studies (Figure 13f) that will be discussed in detail below. A high electrical conductivity minimizes the charge transfer losses in the films and favors metastable metallic 1T' and amorphous phases of MoS_2 and WS_2.[340] Metallic group 5 TMDCs have recently emerged as promising HER catalysts due to their high conductivity combined with the HER activity of their basal planes,[341,342] although ALD studies on these materials are still lacking.

The HER activity, conductivity, and surface area of the substrate should be taken into account when comparing different studies, especially when total electrode activity metrics such as overpotential and Tafel slope are used.[336] For example, certain substrates, such as transition metals (e.g. for Au $\eta_{10} = 220$ mV, Tafel slope 88 mV dec^{-1}), are active HER catalysts by themselves, which is especially important if the deposited film is non-continuous.[213] The substrate may also make an important contribution to the charge transfer losses if it is not highly conductive. Some substrates have large specific surface areas due to roughness or porosity, which is usually not taken into account when calculating the current density using the projected area of the electrode, resulting in a higher apparent performance.

MoS$_2$:

MoS$_2$ is a commonly studied and promising HER catalyst, in both crystalline and amorphous forms, although the amorphous form shows varying S/Mo stoichiometry and is not a 2D material.[343] In the first studies using ALD TMDC catalysts, approximately 10 nm thick MoS$_2$ films grown by the Mo(CO)$_6$+MeSSMe process at 100 °C were found to exhibit good HER activity on both high surface area carbon fiber paper (CFP; η_{10} = 250 mV, Tafel slope 56 mV dec^{-1})[214] and flat Au substrates (η_{10} = 280 mV, Tafel slope 47 mV dec^{-1}).[213] Interestingly, despite the identical preparation conditions, the films on Au were amorphous[213] whereas those on CFP were partially nanocrystalline.[214]

Ho et al.[191] grew MoS$_2$ films on a gold substrate from MoCl$_5$ and H$_2$S that crystallized in the metastable metallic 1T phase, which was stated as the reason for the high catalytic activity (η_{10} = 260 mV, Tafel slope 60 mV dec^{-1}). However, no saturation of the ALD reactions were shown and the films were non-uniform over the substrates, which suggests the presence of etching or other parasitic reactions.

Amorphous molybdenum thiolate hybrid films deposited on a gold substrate by MacIsaac et al.[211] from Mo(CO)$_6$ and HS(CH$_2$)$_2$SH were also shown to be highly active in HER, reaching an overpotential of 294 mV (**Figure 14**a) and a Tafel slope of 52 mV dec^{-1} (Figure 14b). The authors also determined turn-over frequency (TOF) of surface sites, which gives the HER activity of individual sites rather than that of the complete electrodes. The TOF of the thiolate films was found to be comparable to deliberately nanostructured forms of MoS$_2$ (Figure 14c). Crystalline MoS$_2$ films produced by annealing exhibited poorer activity compared to the hybrid thiolate films as shown in Figure 14a–c. Nevertheless, even the annealed films performed better than flat MoS$_2$ films measured for comparison.
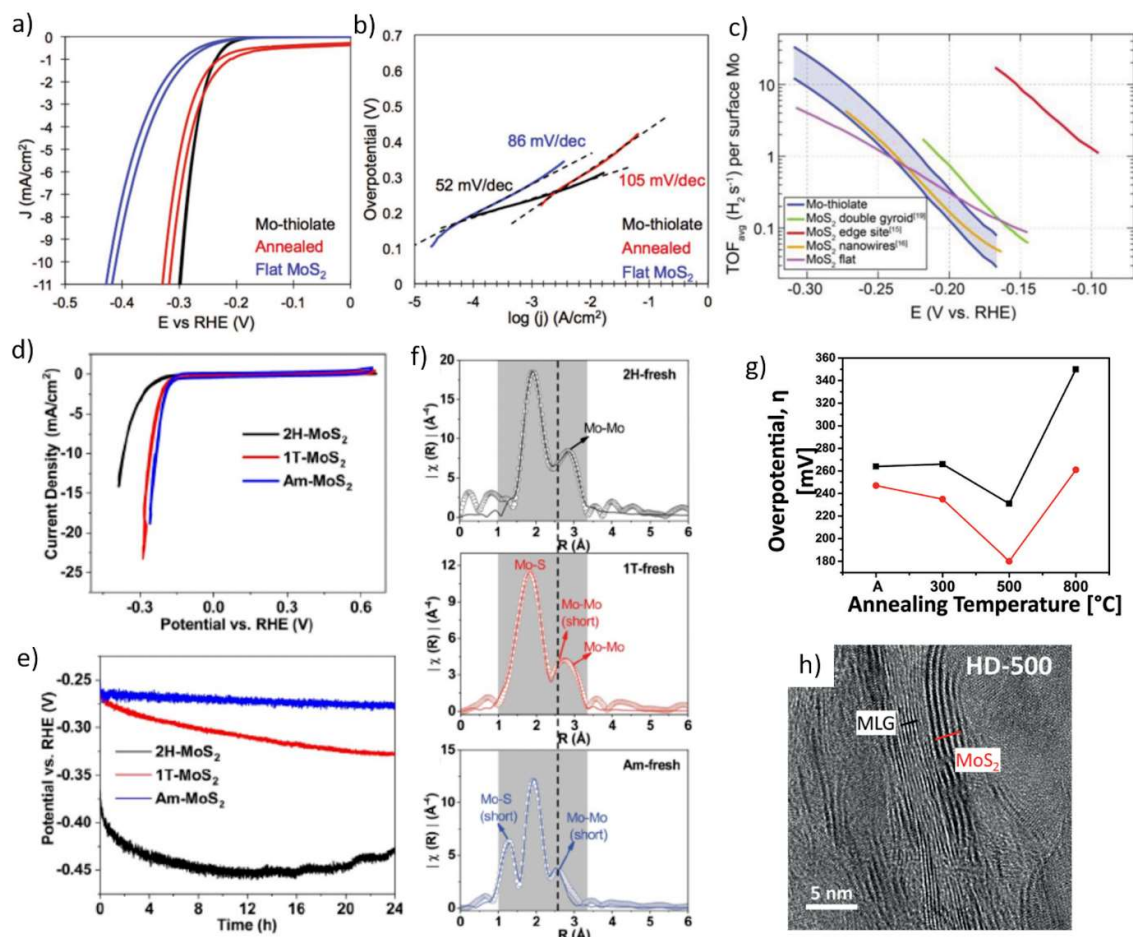
Figure 14. Electrochemical characterization of ALD MoS$_2$ and MoS$_2$ thiolate HER catalysts: a) cyclic voltammograms, b) Tafel plots, and c) turn-over frequency (TOF) plot of a Mo-thiolate film as-deposited (Mo(CO)$_6$+HS(CH$_2$)$_2$SH) and after annealing in a H$_2$S/H$_2$ ambient at 350 °C. A flat MoS$_2$ film and in c) different nanostructured forms of MoS$_2$ are included for comparison.[211] Characterization of MoS$_2$ films of different phases as HER catalysts: d) cyclic voltammograms, e) 24-hour chronopotentiometric response, and f) Mo K-edge Fourier transform extended X-ray absorption fine structure (EXAFS) of MoS$_2$ films showing bond lengths in different phases. Am = amorphous.[223] Effect of annealing temperature on HER activity of ALD MoS$_2$: g) overpotential η$_{10}$ versus annealing temperature (A = as-deposited, upper (black) and lower (red) curves represent MoS$_2$ on low-density and high-density graphene foam substrates, respectively) and h) cross-sectional TEM image of MoS$_2$ film deposited using Mo(NMe$_2$)$_4$ and H$_2$S at 100 °C after annealing at 500 °C (MLG = multilayer graphene).[228] a–c) Reproduced with permission.[211] Copyright 2018, WILEY-VCH Verlag GmbH. d–f) Reproduced under the terms of the CC-BY license.[223] Copyright 2019 Authors. g,h) Reproduced with permission.[228] Copyright 2020, The Royal Society of Chemistry.

Sharma et al.[105] deposited crystalline 2H-MoS$_2$ films using Mo(N^{t}Bu)$_2$(NMe$_2$)$_2$ and H$_2$S plasma and achieved a modest overpotential of 487 mV at 10 mA cm^{-2} and a Tafel slope of 99

mV dec^{-1}. The HER performance was independent of the film thickness in the range of 15–100+ nm, which was attributed to saturation of electrochemically active surface area.

An insightful study by Wu et al.[223] compared the activity of amorphous and 2H-MoS$_2$ films deposited by the Mo(N^{t}Bu)$_2$(NMe$_2$)$_2$+H$_2$S plasma process at 250 and 450 °C, respectively. 1T-MoS$_2$, which is known to be highly HER active, was produced by post-deposition lithiation treatment applied to the 2H-films. Amorphous MoS$_2$ exhibited superior activity to the 2H-MoS$_2$ and superior stability to the 1T-MoS$_2$ films (Figure 14d,e). The excellent activity of amorphous MoS$_2$ was attributed to presence of shorter Mo-Mo bonds (Figure 14f) as well as its higher electrical conductivity compared to 2H-MoS$_2$. The overpotential and Tafel slopes of 230 mV and 42 mV dec^{-1} are excellent, especially considering that the glassy carbon substrate does not have a very high surface area. Additional experiments on similar films reported in the PhD thesis of Sharma[222] also showed the improved activity of amorphous MoS$_2$ over 2H-MoS$_2$, and demonstrated that the use of high-surface area CFP substrates further improved the performance of amorphous MoS$_2$.

Cao et al.[227] deposited amorphous MoS$_2$ films on TiO$_2$ nanotubes using Mo(NMe$_2$)$_4$ and H$_2$S at 95 °C. The excellent HER performance, including a low η_{10} of 189 mV and stable operation for 36 h, was attributed to the amorphous nature of the films as well as to the large surface area of the nanotubular substrate. When using a planar TiO$_2$ substrate instead, η_{10} was observed to be much higher, approximately 450 mV.

Teich et al.[228] deposited amorphous MoS$_2$ films on graphene foam using Mo(NMe$_2$)$_4$ and H$_2$S at 80 °C. The as-deposited amorphous film showed good HER performance (η_{10} = 247 mV, Tafel slope 71 mV dec^{-1} on high-density graphene foam), which was further improved upon crystallization by annealing in a sulfur ambient at 500 °C (η_{10} = 180 mV, Tafel slope 47 mV dec^{-1}) as shown in Figure 14g,h. The films annealed at 500 °C had a rather small grain size of approximately 10 nm and appeared defective, which was deemed beneficial for high HER activity. Annealing at 300 °C was insufficient to crystallize the films and caused a smaller

improvement compared to the as-deposited films, while annealing at 800 °C resulted in a higher crystalline quality but decreased the HER performance. Thus, a highly defective crystalline MoS_2 film was in this case found to perform better than the amorphous film. In addition, high-density graphene foam was found to be a better support compared to low-density graphene foam (Figure 14g), which was attributed to the higher surface area (per geometric area) of the high-density foam.

Wang et al.[275] sulfurized MoO_3 films that were deposited on a high-surface area CFP substrate at 165 °C using $Mo(CO)_6$ and O_3. After sulfurization at 600 °C in a sulfur ambient, reasonably high HER activity with a Tafel slope of 98 mV dec^{-1} was obtained. Lithiation of the films transformed them into the 1T phase and greatly improved the HER activity ($\eta_{10} = 168$ mV, Tafel slope 44 mV dec^{-1}).

Encouragingly, the performance of ALD MoS_2 films stands in comparison to other reports on MoS_2 as well as other non-platinum metal HER catalysts. Bulk MoS_2 has poor HER activity ($\eta_{10} = 1000–1500$ mV, Tafel slope above 100 mV dec^{-1}),[344] whereas flat MoS_2 films are generally more active ($\eta_{10} \approx 400–500$ mV, Tafel slope approximately 100 mV dec^{-1}).[211,344] The best ALD catalysts are able to compete with some of the very best results of the myriad of carefully tailored MoS_2 HER catalysts on high surface area substrates (see Refs. [331,332,336,337,339] and references therein) including hydrothermally synthesized, highly defective 2H MoS_2 nanosheets on reduced graphene oxide ($\eta_{10} = 190$ mV, Tafel slope 41 mV dec^{-1}),[345] chemically exfoliated 1T MoS_2 nanosheets on graphite ($\eta_{10} = 187$ mV, Tafel slope 43 mV dec^{-1}),[346] and hydrothermally produced amorphous MoS_2 on carbon nanotubes ($\eta_{10} = 110$ mV, Tafel slope 40 mV dec^{-1}).[347] Perhaps the best results on flat substrates have been reported for amorphous powder-like MoS_x ($\eta_{10} = 145$ mV, Tafel slope 40 mV dec^{-1}),[348] and a sputtered amorphous MoS_x film ($\eta_{10} = 180$ mV, Tafel slope 45 mV dec^{-1}).[349] Despite comparable performance, none of these methods can match the conformality, reproducibility, and scalability that ALD can offer.

Some directions for further studies that could enable taking ALD MoS_2 HER catalysts toward practical applications include minimizing the catalyst loading and deposition on affordable high-surface area substrates. Amorphous films seem to be the most promising and they come with the added benefit of low deposition temperature, although also defective crystalline films can perform well. The long-term stability of both amorphous and defective crystalline MoS_2 films in the atmosphere as well as under HER conditions should be carefully studied. Rational control of the density and amount of defects in crystalline films is also likely to yield further performance improvements.

WS_2:

Good HER performance has also been demonstrated for ALD WS_2 films. Although the results published so far are not quite on par with the best ALD MoS_2 catalysts, it is likely that the HER performance of ALD WS_2 can be further enhanced. Yeo et al.[266] deposited approximately 20 nm thick, crystalline WS_2 films on porous Ni foam using $W(CO)_6$ and H_2S plasma at 350 °C. The high HER activity ($\eta_{10} = 200$ mV, Tafel slope 64 mV dec^{-1}) may be at least partially due to the large surface area and catalytic activity of the nickel foam ($\eta_{10} = 240$ mV with a high Tafel slope of 152 mV dec^{-1}.[266] Wu et al.[268] observed an η_{10} of 320 mV using WS_2 films deposited by $W(N^tBu)_2(NMe_2)_2$ and H_2S at 300 °C on carbon nanotubes (CNTs), a substrate which is also active in HER by itself in addition to having a very high surface area. Balasubramanyam et al.[269] deposited WS_2 films using $W(N^tBu)_2(NMe_2)_2$ with either H_2S plasma or H_2-diluted H_2S plasma (denoted H_2/H_2S plasma). Different morphologies were observed with the different plasmas. Relatively dense films with edges exposed on the surface were deposited using H_2S plasma. Using H_2/H_2S plasma instead, the films were rough and "flaky" but were electrochemically measured to have a smaller number of active edge sites. The denser, edge-rich films deposited using the H_2S plasma process performed better in HER with a lower η_{10} of 394 mV compared to 461 mV for the H_2/H_2S plasma process.

Table 7. Electrocatalytic HER performance of ALD grown TMDCs in acidic solution. Abbreviations: CFP = carbon fiber paper, CNT = carbon nanotubes, GC = glassy carbon, GF = graphene foam, NT = nanotubes, RHE = reversible hydrogen electrode.

Precursors	Deposition T [°C] (post-treatment T [°C], atmosphere) [a]	Thickness, crystallinity	Substrate	η_{10} [mV vs. RHE] [b]	Tafel slope [mV dec^{-1}] [b]	j_0 [μA cm^{-2}] [b]	Year [Ref.]
			MoS$_2$				
MoCl$_5$ + H$_2$S	250	~10–20 nm rough film, cryst. (1T)	Au	260	60	–	2017[191]
Mo(CO)$_6$ + MeSSMe	100	10 nm film, partly nanocryst.	CFP [c]	250	56	0.8	2016[214]
	100	9.4 nm film, amorp.	Au	280	47	0.03	2015[213]
Mo(CO)$_6$ + HSCH$_2$CH$_2$SH	155–175 (350, H$_2$S/H$_2$)	7 nm film, amorp. ? nm film, cryst.	Au	294 327	52 (as-dep.) 105 (ann.)	–	2018[211]
Mo(N^{t}Bu)$_2$(NMe$_2$)$_2$ + H$_2$S plasma	450	~15 nm rough film, cryst.	GC	487	99	1.8	2018[105]
	250 450 450 (lithiated)	? nm film, amorp. ? nm film, cryst. (2H) ? nm film, cryst (1T)	GC	~230 ~370 ~260	42 65 58	–	2019[223]
	250 450	~40 nm film, amorp. ~100 nm film, cryst (2H)	GC	281 503	54 94	–	2018[222]
	250	? nm film (200 ALD cycles), amorp.	CFP [c]	248	41	1.0	
Mo(NMe$_2$)$_4$ + H$_2$S	95	20 nm film, amorp.	TiO$_2$ NTs [c]	189	–	–	2019[227]
	80 (300, S) (500, S) (800, S)	10 nm film, amorp. ~10 nm film, cryst. ~10 nm film, cryst. ~10 nm film, cryst.	GF [c]	247 235 180 261	71 (as-dep.) 58 (ann.) 47 (ann.) 78 (ann.)	9.6 10.9 17.1 9.6	2020[228]
			MoO$_3$→MoS$_2$				
Mo(CO)$_6$ + O$_3$	165 (600, S)	~10 nm rough film, cryst.	CFP [c]	? 168	98 (as-dep.) 44 (lithiated)	100 –	2013[275]
			WS$_2$				
W(CO)$_6$ + H$_2$S plasma	350	~20 nm film, cryst.	Ni foam [c]	200	64	–	2018[266]
W(N^{t}Bu)$_2$(NMe$_2$)$_2$ + H$_2$S	300	~25 nm film, rough, cryst.	CNT [c]	320	–	–	2019[268]
W(N^{t}Bu)$_2$(NMe$_2$)$_2$ + H$_2$S plasma	300	~8 nm film, rough, cryst.	GC	394	122	–	2019[269]
W(N^{t}Bu)$_2$(NMe$_2$)$_2$ + H$_2$/H$_2$S plasma	300	~8 nm film, rough, cryst.	GC	461	129	–	2019[269]

The measurements were performed in aqueous 0.5 M H$_2$SO$_4$ solution except for 0.1 M H$_2$SO$_4$ in Ref. [223] A Pt counter electrode was used except for a graphite electrode in Refs. [211,213,214,228,275]

[a] For brevity, inert components (N$_2$, Ar) of reactive atmospheres are omitted; [b] The current densities are defined with respect to the projected (geometric) surface areas of the electrodes, i.e. they do not account for the specific surface areas of the substrate or film; [c] High-surface area substrate. Overpotentials using a low-density foam substrate with a lower surface area were higher as shown in Figure 14g.

4.2.2. Electrocatalytic Water Splitting: Oxygen Evolution Reaction

OER has been studied much less compared to the HER, perhaps because O_2 is not as desirable (valuable) a product as H_2. Nevertheless, both reactions are required for water splitting, and the four-electron OER process requires higher overpotentials compared to HER, which decreases the overall water splitting efficiency.[331,350] As such, highly active OER catalysts are desperately needed for efficient water splitting. So far, only two reports have been published about OER using ALD MoS_2 in alkaline conditions (**Table 8**). Nevertheless, these studies have shown highly promising results that are comparable to the best MoS_2 and other non-platinum metal OER catalysts reported in literature (see Refs.[190,331] and references therein), therefore motivating further studies on the subject.

Xiong et al.[207] deposited rough, crystalline MoS_2 films using the $Mo(CO)_6 + H_2S$ process at 200 °C on Co foam, which is a porous OER active substrate. The authors reported an η_{10} of 270 mV, which is 200 mV lower compared to the bare Co foam, along with an improved long-term stability. Huang et al.[190] deposited MoS_2 on carbon fiber paper at 450 °C using $MoCl_5$ and H_2S. Optimal performance, namely an η_{10} of 311 mV and a Tafel slope of 66 mV dec^{-1} was obtained using an approximately 30 nm thick MoS_2 film. A 20 second post-deposition plasma treatment (atmosphere not specified) decreased the η_{10} and Tafel slope to 273 mV and 61 mV dec^{-1}, respectively. The improvement was explained by increased hydrophilicity of the plasma-treated MoS_2, which eases the adsorption of water molecules and release of the formed oxygen bubbles in the first and last steps of the OER process, respectively.

Table 8. Electrocatalytic OER performance of ALD grown TMDCs in alkaline conditions (1 M KOH) using a Pt counter electrode. Abbreviations: CFP = carbon fiber paper.

Precursors	Deposition T [°C]	Thickness, crystallinity	Substrate	η_{10} [mV vs. RHE] a,b)	Tafel slope [mV dec^{-1}] b)	Year Ref.
		MoS$_2$				
MoCl$_5$ + H$_2$S	450	~3 nm rough film, cryst.	CFP c)	362	67	2019[190]
		~30 nm rough film, cryst.		311	66	
		~30 nm film, plasma treated		273	61	
Mo(CO)$_6$ + H$_2$S	200	? nm rough films (~5 nm)	Co foam c)	270	74	2017[207]

a) In contrast to HER, the overpotentials are positive with respect to the thermodynamic potential; b) The current densities are defined with respect to the projected (geometric) surface areas of the electrodes, i.e. they do not account for the specific surface areas of the substrate or film; c) High-surface area substrate.

4.2.3. Photoelectrocatalytic Water Splitting

The semiconducting nature and strong visible light absorption of many TMDCs can also be utilized for photoelectrocatalytic (PEC) water splitting. In the majority of studies so far, ALD TMDCs have been grown on top of other light-absorbing semiconductors in order to improve their stability as well as separation of photogenerated charge carriers (**Table 9**). The light-absorbing electrode can be set as the photoanode, where PEC OER occurs, or as the photocathode with PEC HER occurring on the surface. In many early stage studies such as those reported here, the other water splitting half reaction occurs on a platinum counter electrode. Many other device schemes can also be used, including a single electrode driving both reactions, and a tandem arrangement of two photoelectrodes with suitable energy levels, one driving HER and the other OER. In-depth discussion on PEC water splitting can be found in Refs. [351,352]

For ideal PEC water splitting, no bias is applied between the electrodes, which enables stand-alone operation with all of the energy supplied by sunlight. The main figure of merit of such a device is solar-to-hydrogen conversion efficiency, which can be considered analogous to the power conversion efficiency of solar cells. However, purely solar-driven water splitting is difficult to achieve and requires carefully chosen (tuned) band gaps, energy level alignments, charge carrier lifetimes, and so forth. Therefore, in many cases – including all of the studies discussed below – a bias is applied between the electrodes to increase the current drawn from a PEC water splitting device.

Comparison of the device performance under non-zero-bias conditions is not trivial, with several efficiency metrics proposed and used, including applied bias photon-to-current efficiency (ABPE), incident photon-to-current efficiency (IPCE, also called external quantum efficiency, EQE), and absorbed photon-to-current efficiency (APCE, also called internal quantum efficiency, IQE). A thorough discussion on these metrics can be found in Ref. [352] The different device structures and materials, measurement conditions, and performance metrics used make comparison of different studies very difficult. Therefore, we will focus on describing the roles and improvements brought by ALD TMDC photocathodes and photoanodes in different studies.

Photocathode:

Photocathodes using ALD TMDC films have been constructed on various substrates and the PEC HER measurements have been performed in different conditions. Studies that have examined coating Si with MoS_2 are perhaps the most easily compared to the electrocatalysts described in Section 4.2.1 in terms of their structures as well as measurement conditions. These studies clearly demonstrate the improved HER performance (e.g. η_{10}) obtained upon solar illumination.

Oh et al.[210] deposited MoS_2 films on Si using the $Mo(CO)_6$+H_2S plasma process at 200 °C. Although silicon absorbs light efficiently and has suitable energy levels for PEC HER, it suffers from poor stability and slow HER kinetics. With the MoS_2/p-Si photocathodes, a much more positive potential of +120 mV at 10 mA cm^{-2} was observed under simulated solar light illumination compared to the purely electrocatalytic HER (-200 to -500 mV for ALD MoS_2) or PEC HER using the bare Si substrate (-900 mV). Post-deposition annealing at 600 °C improved the PEC HER activity, as it resulted in the (002) basal planes of MoS_2 being oriented away from the Si substrate plane, exposing the catalytically active edge sites of MoS_2.

Good PEC performance of the n-MoS$_2$/p-Si structure was also demonstrated by Joe et al.[193] The high activity (η_{10} = +130 mV, Tafel slope 56 mV dec^{-1}) was attributed to the formation of a mixture of the metallic 1T and semiconducting 2H phases of MoS$_2$ using the MoCl$_5$+H$_2$S process at 250–300 °C. The optimal MoS$_2$ thickness was 25 to 35 nm. Thinner films showed limited improvement in performance over Si, whereas films thicker than 50 nm also behaved poorly due to increased light absorption in MoS$_2$ (as opposed to Si) and increased charge transfer resistance. Furthermore, the optimal devices retained a stable current for over 70 hours of operation in a 0.5 M H$_2$SO$_4$ electrolyte.

Alqahtani et al.[194] deposited a rough, approximately 20 nm thick MoS$_2$ film using MoCl$_5$ and H$_2$S at 250 °C on a TiO$_2$/GaP/Si photocathode. Although GaP is a promising photoelectrode material, it suffers from high cost and poor stability, which the authors overcame by growing GaP as an epitaxial thin film on Si and applying a protective ALD-grown TiO$_2$ layer on top, respectively. The rough ALD MoS$_2$ layer functioned as an effective and stable HER catalyst at pH = 0 operating conditions with a maximum photocurrent density of 0.95 mA cm^{-2} at –0.8 V (vs. RHE).

Hellstern et al.[283] sulfurized an ALD MoO$_3$ layer deposited onto a TiO$_2$/CdS/CuGaSe$_2$/FTO stack (FTO = fluorine-doped tin oxide) at a very low temperature of 200 °C in a H$_2$S/H$_2$ ambient. Unfortunately, no characterization of the MoS$_2$ layer was performed. The resulting structure with CuGaSe$_2$ as an absorber, CdS as a buffer layer, TiO$_2$ as an interfacial layer, and MoS$_2$ as a HER catalyst was used as a photocathode for PEC HER in a 0.5 M H$_2$SO$_4$ solution. A HER onset potential of +0.53 V was obtained, which was clearly superior to that of bare CuGaSe$_2$ (+0.02 V) or CdS/CuGaSe$_2$ (+0.12 V). An IPCE as high as 53% was obtained at –0.5 V under 450 nm illumination. The MoS$_2$ layer was stable in the operating conditions for 7 h, after which deterioration occurred. The stability was improved over the CdS/CuGaSe$_2$/FTO device, but further enhancement is needed for practical devices.

Using SnS$_2$ films deposited on FTO-coated glass, Hu et al.[249] achieved both PEC HER (photocathode) and PEC OER (photoanode) under acidic conditions (0.25 M H$_2$SO$_4$). However, the maximum current densities were relatively low, 35.1 and 51.5 μA cm^{-2} for HER and OER at −0.4 and +1.0 V, respectively. The best performance was observed using a 50 nm thick SnS$_2$ film deposited at 140 °C, which contained some SnS$_2$ nanocrystallites in an amorphous matrix.

Photanode:

Similar to the photocathodes described above, electrodes of different materials and structures have been coated with ALD TMDCs for use as photoanodes (PEC OER). Hu et al.[247] constructed nanostructured hollow inverse opal shell (IOS) structures for PEC water splitting with an aluminum-doped zinc oxide (AZO) layer sandwiched between two 40 nm thick amorphous SnS$_2$ films deposited using Sn(NMe$_2$)$_4$ and H$_2$S at 150 °C (**Figure 15**a,b). The photoanode enabled OER at a current density of 1.05 mA cm^{-2} at 1.65 V (vs. RHE) under solar illumination in a neutral 0.5 M Na$_2$SO$_4$ solution. In this structure, light was absorbed by both AZO and SnS$_2$. Based on the band alignment, it was inferred that the electrons created upon absorption of light travelled through AZO to the Pt counter electrode, where H$_2$ was produced. Holes generated in both AZO and SnS$_2$ ended up at the SnS$_2$ surface, where they took part in OER. The generated photocurrent was up to eight times higher compared to bare SnS$_2$ and 19 times higher than that of bare AZO device (Figure 15c). Hu et al.[249] also reported SnS$_2$/FTO electrodes that could be used as either photocathode or photoanode, as described in the previous section.

Ho et al.[195] deposited MoS$_2$ on top of CdS nanorods using MoCl$_5$ and H$_2$S at 250 °C in order to improve the separation of charge carriers generated in CdS as well as to overcome the poor stability of CdS. The resulting core-sheath structure was used as a photoanode in a 10 vol-% lactic acid solution (pH = 3). The MoS$_2$ layer increased the photocurrent by 46% up to 1.8 mA

cm^{-2} at 0.8 V, increased the IPCE to approximately 55% at 400 nm compared to ~20% for CdS, and improved the stability of the CdS anode.

Motola et al.[220] grew MoS_2 films on TiO_2 nanotubes at 275 °C using one to five cycles of the $Mo(N^tBu)_2(NMe_2)_2+H_2S$ process. The best performance as a photoanode in PEC in a neutral 0.1 M Na_2SO_4 solution under monochromatic illumination was achieved using two ALD cycles. The deposited MoS_2 extended the activity of the catalyst from UV to visible range, up to a wavelength of approximately 600 nm compared to 400 nm for TiO_2 (Figure 15d). In a similar manner, Ng et al.[231] used the $Mo(CO)_6+Se(SiMe_3)_2$ process to deposit films on TiO_2 nanotubes at 167 °C. The resulting films were characterized as amorphous $MoSe_xO_y$ (on surface $x \approx 0.7$, $y \approx 1.7$), which implies insufficient reactivity of the ALD precursors and possibly instability of the films in air. Ten ALD cycles resulting in an approximately 2 nm thick film yielded the best PEC performance, namely increased IPCE by factors of 2 and 40 at wavelengths of 365 and 470 nm, respectively, compared to the bare TiO_2 nanotubes. The improvement was attributed to light absorption by the $MoSe_xO_y$ layer as well as surface passivation of the TiO_2 nanotubes.

4.2.4. Photocatalysis

Motola et al.[220] studied MoS_2 films for photocatalytic liquid phase degradation of methylene blue in an aqueous solution, where reaction rates improved two and ten-fold upon illumination at 365 and 410–425 nm compared to the bare TiO_2 nanotubes (Figure 15e). For gas-phase photocatalytic conversion of hexane to CO_2, one cycle of MoS_2 performed the best, with a five-fold increase in conversion under 351 nm illumination compared to the bare TiO_2 nanotubes (Figure 15f). The amorphous $MoSe_xO_y$ films deposited by Ng et al.[231] were also used for photocatalytic degradation of methylene blue under 470 nm illumination, resulting in an increase of the rate constant by a factor of 75 compared to the bare TiO_2 nanotubes. The films in these two works were also used for PEC water splitting (Section 4.2.3)
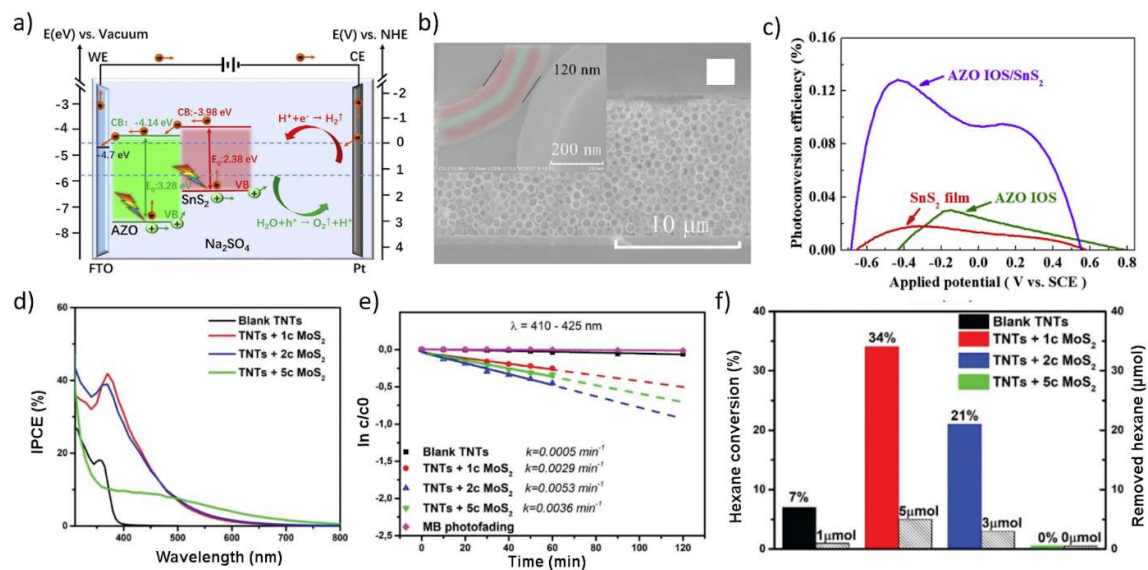
Figure 15. SnS$_2$/AZO inverse opal shell (IOS) photoanode: a) schematic diagram of energy levels and charge carrier separation, transport, and reactions (at 1.65 V vs. RHE) under illumination, b) cross-sectional SEM image of the photoanode, inset showing a single IOS (SnS$_2$ and AZO layers colored red and green, respectively), and c) ABPE as a function of applied potential under illumination (0.5 M H$_2$SO$_4$, vs. saturated calomel electrode, SCE) showing superiority of the SnS$_2$/AZO structure compared to bare SnS$_2$ and AZO. Reproduced[247] MoS$_2$/TiO$_2$ nanotube (TNT = TiO$_2$ nanotube) catalysts: d) PEC water splitting: IPCE versus wavelength (0.1 M Na$_2$SO$_4$, 1.0 V vs. RHE), e) liquid photocatalytic degradation of methylene blue (MB) and the extracted rate constants (k) under 410–425 nm illumination, and f) gas-phase photocatalytic conversion of hexane to CO$_2$ under 351 nm illumination. a–c) Reproduced with permission.[247] Copyright 2020, Elsevier. d–f) Adapted with permission.[220] Published by The Royal Society of Chemistry under CC-BY-NC license.

Table 9. PEC water splitting performance of devices using ALD grown TMDCs under solar irradiation (AM 1.5G). Abbreviations: ABPE = applied bias photon-to-current efficiency, AZO = ZnO:Al, FTO = SnO$_2$:F, IPCE = incident photon-to-current efficiency, ITO = In$_2$O$_3$:SnO$_2$, NT = nanotube.

Precursors	Deposition T [°C] (post-treatment T [°C], atmosphere) [a]	Thickness, crystallinity	Photoelectrode, structure, (solution) [b,c]	Performance metrics [d]	Year [Ref.]
			MoS$_2$		
MoCl$_5$ + H$_2$S	250–300	~25 nm rough film, cryst. (1T/2H mix)	cathode, **MoS$_2$***/Si, (0.5 M H$_2$SO$_4$)	Tafel slope 56 mV dec^{-1} η_{10} = +130 mV Improved stability (at least 70 h)	2018[193]
	250	~20 nm rough film, cryst.	cathode, **MoS$_2$***/TiO$_2$*/GaP/Si, (1 M HClO$_4$)	Max. current 0.95 mA cm^{-2} (−0.8 V) Onset potential +0.47 V IPCE 23.8% @ 400 nm (−0.8 V) Improved stability (at least 3 h)	2019[194]
	250	~7 nm rough film, cryst. (1T/2H mix)	anode, **MoS$_2$***/CdS/ITO, (10 vol-% lactic acid)	Max. current 1.8 mA cm^{-2} (0.8 V) IPCE 55% @ 400 nm (cf. CdS ~20%) Improved stability	2019[195]
Mo(CO)$_6$ + H$_2$S plasma	200 (600, H$_2$S)	~14 nm rough film, cryst.	cathode, **MoS$_2$***/Si, (0.5 M H$_2$SO$_4$)	η_{10} = +120 mV Max current 31 mA cm^{-2} (−0.3 V) η reduced by 630 mV vs. Si Improved stability	2017[210]
			MoO$_3$→MoS$_2$		
Mo(CO)$_6$ + O$_2$ plasma	165 (200, H$_2$/H$_2$S)	~5 nm film	cathode, **MoS$_2$***/TiO$_2$*/CdS/ CuGaSe$_2$/FTO, (0.5 M H$_2$SO$_4$)	Onset potential +0.53 V, η_{10} = −500 mV IPCE 44% @ 450 nm (0 V) Improved stability (up to 7 h)	2019[283]
			SnS$_2$		
Sn(NMe$_2$)$_4$ + H$_2$S	140	50 nm film, amorp.	cathode (anode), **SnS$_2$***/FTO, (0.25 M H$_2$SO$_4$)	Max. current 35.1 (51.5) μA cm^{-2} for HER (OER) at −0.4 (+1.0) V IPCE 2.2% @ 390 nm (0 V) ABPE 0.014% (0.75 V)	2019[249]
	150	40 nm film, amorp	anode, **SnS$_2$***/AZO/FTO, (0.5 M Na$_2$SO$_4$)	Max. current 1.05 mA cm^{-2} (1.65 V) IPCE 11.2% @ 380 nm (0 V) ABPE 0.12% (0.2V)	2020[247]

[a] For brevity, inert components (N$_2$, Ar) of reactive atmospheres are omitted; [b] ALD-grown layers are marked by an asterisk (*) and the TMDC layer is **bolded**; [c] A Pt counter electrode was used except for an IrO$_x$/Ir electrode in Ref. [283]; [d] All biases are reported (converted if needed) vs. RHE. Unlike the electrocatalytic water splitting, the overpotentials are written with a positive/negative sign with respect to the thermodynamic potential. See Ref. [352] for definitions of different metrics.

4.3. Energy Storage

Several studies have been devoted to the use of ALD MoS_2 and WS_2 films as an anode (negative electrode) in lithium and sodium ion batteries (LIBs and NIBs, respectively), one study has used MoS_2 as a cathode in $Li-O_2$ batteries, and a few studies have focused on supercapacitor electrodes (**Figure 16**a). Although these applications have somewhat different requirements, all of the films studied so far have been deposited at relatively low temperatures from 150 to 350 °C. Both crystalline and amorphous, in most cases tens of nanometers thick films have been examined. The excellent scalability and ability to coat high surface-area substrates makes ALD a promising method for producing coatings for many energy applications in not only for research but potentially also on industrial scale. Nevertheless, ALD also has its challenges in energy storage. For example, in many cases the substrates may be in powder form, the end products may be low cost, and rather thick films may be required. More studies are required to identify the best TMDC materials and processes for each application as well as the most promising energy storage applications for ALD TMDCs in general, both in terms of film performance and industrial viability.
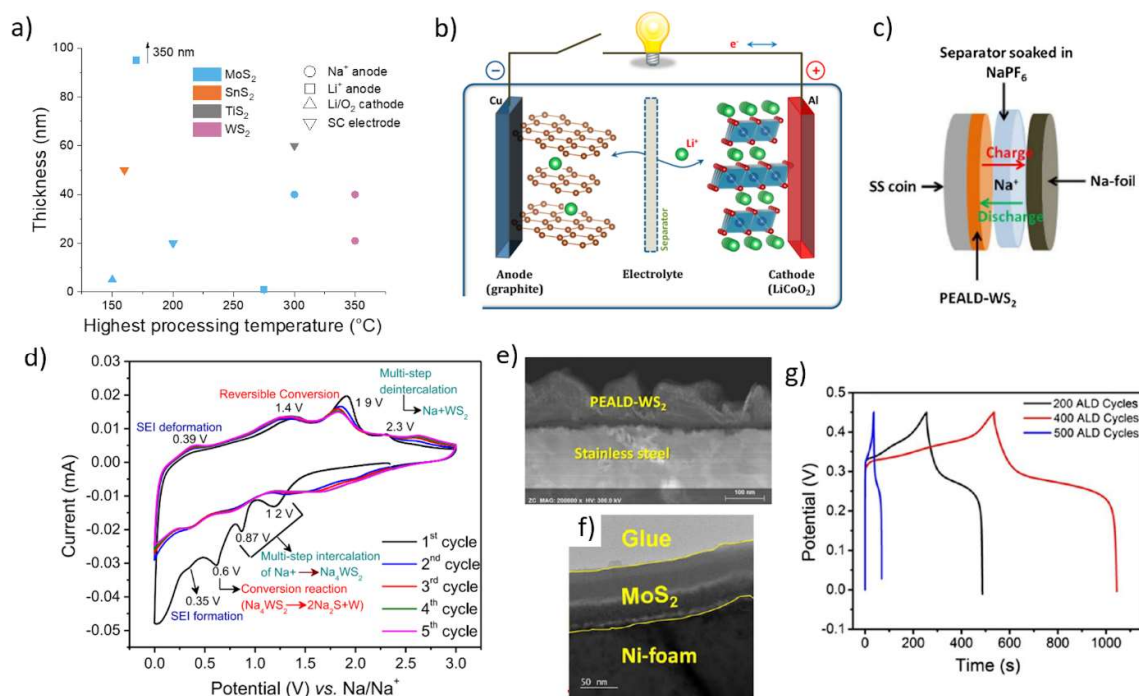
Figure 16. a) Overview of thickness and processing temperature of ALD TMDCs evaluated for energy storage applications (data from Table 2 and 3). SC = supercapacitor. b) Schematic of a typical lithium-ion battery (LIB). Sodium ion battery (NIB) using an ALD WS_2 anode: c) schematic of a NIB in a coin-type half-cell configuration (SS = stainless steel), d) cyclic voltammogram of the anode deposited by 200 ALD cycles showing different steps that occur during charging (top curves from left to right) and discharging (bottom curves from right to left), and e) cross-sectional HAADF-STEM image of a rough WS_2 anode deposited on stainless steel. ALD MoS_2/Ni foam supercapacitor: f) cross-sectional TEM image of the structure and g) charge-discharge profiles of the supercapacitors using MoS_2 films of different thicknesses at a current density of 3 mA cm^{-2}. b) Reproduced with permission.[353] Copyright 2013, American Chemical Society. c) Reproduced with permission.[266] Copyright 2018, Elsevier. d,e) Reproduced with permission.[267] Copyright 2019, Elsevier. f,g) Reproduced with permission.[209] Copyright 2017, American Chemical Society.

4.3.1. Lithium and Sodium Ion Batteries

LIBs powering devices from smartphones to laptops and electric cars are an inseparable part of our modern lives. Nevertheless, smaller, safer, and more energy-dense batteries, both improved LIBs as well as new battery concepts including NIBs and Li-O_2 batteries form an intensive area of research. A typical commercial lithium ion battery consists of an anode (usually graphite) and a cathode (typically a lithiated transition metal oxide, such as $LiCoO_2$) immersed in an electrolyte (such as $LiPF_6$ in an organic carbonate solvent), which conducts Li$^+$ ions but not electrons, and a separator that keeps the electrodes physically apart (Figure 16b).[353,354] ALD also holds great promise for thin-film batteries that use solid electrolyte layers.[355]

During the use (discharge) of a LIB, Li$^+$ ions extracted from the negative electrode (anode) flow through the electrolyte to be inserted into the positive electrode (cathode), while electrons flow in the same direction through an external circuit and can be used to do work. Rechargeable batteries can be charged using an external voltage source to reverse the flow of ions and electrons.

In early testing of individual electrodes, such as the studies described in this section, a simplified half-cell design is typically used, where lithium (sodium in NIBs) metal acts as a counter electrode (anode) to the examined electrode (Figure 16c). In such half-cells, TMDCs act as the cathode (positive electrode). Thus, in the following discussion and figures, insertion

of lithium into a TMDC is defined as the discharge reaction and extraction of lithium from the lithiated TMDC is termed the charge reaction. In full LIBs using TMDCs as the anode, the charge/discharge reactions are reversed.[356]

TMDCs such as MoS_2 can store Li^+ as well as the larger Na^+ ions via both intercalation (Equation 1) and conversion (Equation 2) reactions.[192,357] Similar reactions for Na^+ in WS_2 are illustrated in Figure 16d. The intercalation into the vdW gap of TMDCs is highly reversible but has only limited capacity, whereas the conversion reactions occurring at lower potentials versus Li/Li^+ (deep discharge in half-cells) provide increased capacity at the cost of possible material degradation and irreversibility due to large volume changes. Compared to bulk TMDCs, 2D MoS_2 sheets, such as those grown by ALD, can better accommodate the volume changes without structural damage. In practice, various ill-defined reactions, including those between the electrode and electrolyte, also commonly occur.

$$MoS_2 + xLi^+ + xe^- \leftrightarrow Li_xMoS_2 \quad (0 \leq x \leq 1),\ E^0 = 1.1\text{–}3.0 \text{ V vs. } Li/Li^+ \tag{1}$$

$$Li_xMoS_2 + (4-x)Li^+ + (4-x)e^- \leftrightarrow Mo + 2Li_2S,\ E^0 = 0.6\text{–}1.1 \text{ V vs. } Li/Li^+ \tag{2}$$
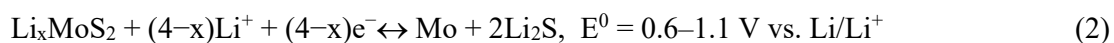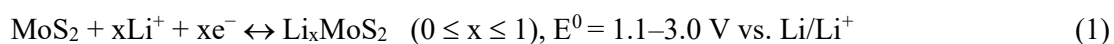
The theoretical gravimetric (specific) capacities of MoS_2 using only intercalation and both intercalation and conversion reactions are, respectively, 167 and 669 mAh g^{-1} for LIBs and 146 and 571 mAh g^{-1} for NIBs.[357] TMDCs composed of heavier elements will obviously have lower theoretical gravimetric densities, for example 433 mAh g^{-1} for WS_2 LIBs. Despite their lower capacity, NIBs are actively studied due to their possible cost advantages compared to LIBs. However, the lack of suitable anode materials has been one of the main challenges for NIBs.[358]

Due to the intermediate insertion (intercalation) voltage of approximately 2 V versus Li/Li^+ of many TMDCs (to be compared with approximately 0.2 V for graphite and 4.5 V for $LiCoO_2$), they may be applied as both the cathode and anode, though in both cases resulting in only a

modest cell voltage. Although initial LIB studies in the 1970s and 80s explored TMDCs as the cathode,[354] most of the more recent studies including the ALD studies discussed here study TMDCs as the anode for LIBs and NIBs. The possibly low cell voltage is a disadvantage as the amount of stored energy is a product of voltage and capacity, however it may be compensated by the high capacities of TMDCs. For comparison, the theoretical capacity of the graphite anodes used in commercial LIBs is 372 mAh g^{-1}.[359]

In addition to the high gravimetric/volumetric/areal capacity that is stable for hundreds to thousands of charge-discharge cycles and a low voltage versus Li/Li$^+$, an ideal LIB anode should be charged and discharged rapidly, possess high electrical and ionic conductivities, be stable and insoluble with the electrolytes used, safe, cheap, and environmentally friendly. Although we will use the gravimetric capacity as the main benchmark in the following discussion for the widespread availability of these values, attention should also be paid to other factors besides capacity, especially considering that the limited capacity of the available cathode materials (100–200 mAh g^{-1}) will restrict the achievable total cell capacity.[360]

Experimentally, very high gravimetric capacities far exceeding the theoretical ones have been obtained using TMDCs grown by ALD (Table 10) as well as by other methods (see Refs. [357,361] and references therein). Nanoscale materials are often reported to exhibit higher than expected capacities, which may be due to presence of various defects as well as contributions from double layer capacitance and pseudocapacitance (see Section 4.3.3).[357] Indeed, it has been observed that nanostructured carbon-based substrates, for example, can possess much higher capacities compared to graphite.[360] In addition, the morphology or even composition of the TMDC electrode may change irreversibly during charge-discharge cycling, which can affect the observed capacity and its cycling stability.[359] Yet another factors affecting the measured capacity are the voltage range used and the charge-discharge rates. Increasing the voltage range generally increases the capacity as well as the amount of energy stored, but may decrease the cycleability, whereas increasing the charge-discharge rate (often denoted using C rate, where 1

C corresponds to complete discharge/charge of a battery in 1 hour, 2 C in ½ hour and so forth) decreases the available capacity and may also have a detrimental effect on the cycling stability. One needs to keep in mind that the estimation of electrode mass, which is required to convert the measured areal capacity to gravimetric capacity, usually involves estimation of film thickness and density, both of which are prone to inaccuracies for ultrathin, potentially rough electrodes such as those deposited by ALD. For thin film batteries, the areal capacity is the limiting factor rather than the gravimetric capacity, but defining the areal capacity is also not without its challenges. Usually the areal capacity is determined per geometric substrate area, in which case it depends on the thickness and specific surface area of the deposited electrode. In case rough films are deposited, this increases the actual surface area above that of the substrate. Although most of the studies described below have dealt with planar electrodes, ALD has excellent potential to prepare 3D electrodes to increase the geometric areal capacity.[355,362,363] Therefore, direct comparison between the early investigations of ALD TMDCs discussed below and especially comparisons to conventional particle-based electrodes should be undertaken with caution. Finally, the capacity of a real-world battery also depends on the other battery components, including the other electrode, electrolyte, separator, and packaging.

Nevertheless, a rough comparison shows that the reported gravimetric capacities of ALD-grown TMDCs (**Table 10**) compare favorably to TMDCs produced by other methods, which gives promise for further studies toward practical batteries. For example, in LIBs, capacities of (non-ALD) MoS_2 anodes on carbon-based substrates are often found to range from 700 to 1300 mAh g^{-1} after 50–100 charge-discharge cycles, only the very best examples exceeding 1500 mAh g^{-1}.[357] In NIBs, high-performance MoS_2-based anodes have been reported to provide capacities from 200 to 400 mAh g^{-1} after 50–500 charge-discharge cycles.[357]

Sreedhara et al.[192] grew crystalline and rough, approximately 40 nm thick ALD MoS_2 anodes using $MoCl_5$ and H_2S at 300 °C. Very high gravimetric capacities were observed during the first charge-discharge cycle and even the capacities reported after 100 cycles were high: 1710

and 667 mAh g^{-1} for LIBs and NIBs. The high Li$^+$ ion capacity was attributed to the double layer capacitance due to adsorption of Li$^+$ ions on the MoS$_2$ crystal edges and basal surfaces, which both were exposed because of the rough morphology of the films. Importantly, the capacity was rather stable after the first tens of charge-discharge cycles. When the voltage range was limited to 1.2–3.0 V (vs. Li/Li$^+$ or Na/Na$^+$) as opposed to 0.2–3.0 V, mainly intercalation reactions were thought to occur, which resulted in a much lower – although again higher than theoretical – capacity of 590 mAh g^{-1} for Li$^+$.

Nandi and coworkers deposited amorphous MoS$_2$ (Ref. [205]) and WS$_2$ (Ref. [263]) anodes on stainless steel using analogous M(CO)$_6$+H$_2$S processes. Both materials exhibited high areal (estimated gravimetric) lithium-ion capacities: approximately 115 μAh cm^{-2} (850 mAh g^{-1}) and 14 μAh cm^{-2} (500 mAh g^{-1}) for 350 nm MoS$_2$ and 80 nm WS$_2$ films after 50 charge-discharge cycles. The stability of the WS$_2$ anode could be improved by using it only for the intercalation reactions in the voltage range of 1.0 to 2.5 V (vs. Li/Li$^+$), which resulted in a smaller capacity (4.5 vs. 14 μAh cm^{-2}).[263] Considering the amorphous nature of the materials, however, the claim on intercalation would need further proof. Nevertheless, in the smaller voltage range, much higher charge-disharge rates up to 17 C could be used while retaining relatively good cycleability.

Yeo et al.[266] prepared a crystalline WS$_2$ anode using the W(CO)$_6$+H$_2$S plasma process at 350 °C that had a relatively good stability with an areal capacity of 44.5 μAh cm^{-2} (after 50 charge-discharge cycles) as a NIB anode. Using the reported 21 nm film thickness, this translates to an extremely high gravimetric capacity of 2800 mAh g^{-1}. However, as noted above, such calculations for ultrathin batteries are prone to inaccuracies and may also be affected by the rough film morphology (Figure 16e). In a follow-up study by the authors, the highest NIB areal capacity of 59 μAh cm^{-2} after 50 charge-discharge cycles was achieved using an

approximately 40 nm thick WS_2 film, whereas the areal capacities of thinner and thicker films were lower presumably due to increased resistance of the thicker films.[267]

A LIB anode consisting of a discontinuous MoS_2 film on TiO_2 nanotubes was prepared by Sopha et al.[219] Using long precursor exposure times for $Mo(N^tBu)_2(NMe_2)_2$ and H_2S, approximately 1 nm thick and 10–15 nm wide MoS_2 islands were deposited using only 2 ALD cycles. Compared to a bare TiO_2 nanotube electrode, a viable LIB anode by itself, the capacity increased from 400 to 670 $\mu Ah\ cm^{-2}$, which demonstrates the advantage of using a high surface area substrate. The films were crystalline, but contained different Mo_xS_y phases in addition to MoS_2. Using the same process and deposition conditions, Tesfaye et al.[221] deposited MoS_2 islands on TiO_2 nanotubes using 15 cycles. However, the authors found that the cycling stability of the electrode was rather poor. Therefore, the MoS_2 islands were sandwiched between ultrathin Al_2O_3 layers deposited using 9 ALD cycles, which greatly improved cycleability. The sandwich electrode showed a capacity increase of 280 $\mu Ah\ cm^{-2}$ after 200 charge-discharge cycles compared to the bare nanotube electrode, whereas with the MoS_2 layer only the capacity merely increased by 65 $\mu Ah\ cm^{-2}$ over the TiO_2 electrode.

Sayed et al.[255] have studied diffusion and intercalation mechanisms of Li^+ and Na^+ ions into rough ALD TiS_2 films. The first cycle discharge capacities of both Li^+ and Na^+ ions, approximately 750 and 450 $mAh\ g^{-1}$, respectively, were lower compared to most of the and WS_2 anodes discussed here but still higher than that of graphite, for example. Cycling stability of the TiS_2 anodes needs to be investigated, however.

Table 10. LIB and NIB anode performance of ALD grown TMDCs.

Precursors	Deposition T [°C] (post-treatment T [°C], atmosphere)	Thickness, crystallinity	C-rate a)	Voltage range [V] b)	Gravimetric capacity [mAh g^{-1}]	Areal capacity [μAh cm^{-2}]	Year [Ref.]
					MoS$_2$		
MoCl$_5$ + H$_2$S	300	~40 nm rough film, cryst.	0.8	0.2–3.0	NIB: 1st cycle: 1065 100th cycle: 667	– –	2018[192]
			0.3	0.2–3.0	LIB: 1st cycle: 2726 100th cycle: 1710	– –	
			0.3	1.2–3.0	LIB: 100th cycle: 590	–	
Mo(CO)$_6$ + H$_2$S	170	350 nm film, amorp.	0.2	0.0–3.0	LIB: 1st cycle 1110 50th cycle: 851	150 115	2014[205]
Mo(N^{t}Bu)$_2$(NMe$_2$)$_2$ + H$_2$S	275	~1 nm discont. film, cryst.	1	0.0–3.0	LIB: 1st cycle 100th cycle	270 d,e) 220 d,e)	2019[219]
	275	? nm islands, cryst.?	3	0.01–3.0	LIB: 1st cycle 200th cycle	570 d,e) ~65 d,e)	2020[221]
					LIB: 200th cycle	280 d,f)	
					TiS$_2$		
TiCl$_4$ + H$_2$S	300	tens of nm thick rough films, cryst.	0.1 0.2	0.5–3.0 0.5–3.0	LIB: 1st cycle: ~750 NIB: 1st cycle ~450	– –	2019[255]
					WS$_2$		
W(CO)$_6$ + H$_2$S	?	~80 nm film, amorp.	1.4	0.1–3.0	LIB: *1st cycle: ~570 c) 50th cycle: ~460 c)*	16 14	2016[263]
			4	1–2.5	LIB: *1st cycle: ~160 c) 50th cycle: ~150 c)*	5 4.5	
			17	1–2.5	LIB: *1st cycle: ~160 c) 50th cycle: ~115 c)*	5.0 3.5	
W(CO)$_6$ + H$_2$S plasma	350	21 nm film, cryst.	?	0.0–3.0	NIB: *1st cycle: ~3900 c) 50th cycle: 2800 c)*	61.5 44.5	2018[266]
	350	~40 nm rough film, cryst.	0.8	0.0–3.0	NIB: *1st cycle: 2300 c) 50th cycle: 1600 c)*	88 59	2019[267]

The measurements were performed in half-cells with the TMDC film directly grown on a stainless steel substrate (excluding TiO$_2$ nanotube substrate in Refs.[219,221]) without any binder or additives, a Li or Na metal counter electrode and a conventional electrolyte (LiPF$_6$/NaPF$_6$ mixed with organic carbonate solvents). a) The discharge rates (C-rates) were calculated from the reported capacities and currents (1 C corresponds to a complete discharge of a battery in 1 hour, 2 C in ½ hour and so forth; b) The voltages are given vs. Li/Li$^+$ (LIBs) or Na/Na$^+$ (NIBs); c) The *italic* gravimetric capacities were calculated from the reported mass loading, areal capacity (per geometric area), and film thickness; d) The areal capacity was obtained by subtracting the capacity of the bare nanotubular TiO$_2$ substrate from the total capacity; e) MoS$_2$/TiO$_2$ nanotube structure; f) Al$_2$O$_3$/MoS$_2$/Al$_2$O$_3$/TiO$_2$ nanotube structure.

4.3.2. Lithium-Oxygen Batteries

Using the Mo(CO)$_6$+MeSSMe process, Song et al.[216] deposited an amorphous, approximately 5 nm thick MoS$_2$ layer on a graphitic carbon substrate coated with carbon nanotubes. In contrast to the aforementioned studies, the structure was utilized as a cathode in a lithium-oxygen battery.

Li-O$_2$ batteries use a Li metal anode with a cathode that acts as an electrochemical contact and catalyst between O$_2$ gas and Li$^+$ ions dissolved in electrolyte. Such a design can theoretically achieve much higher capacities than LIBs, although Li-O$_2$ batteries currently suffer from several practical challenges including poor cycleability.[364] The authors obtained an extremely high gravimetric capacity of 4844 mAh g^{-1} at 500 mA g^{-1} with a lifetime of 190 cycles when limited to 500 mAh g^{-1} that compares favorably to other Li-O$_2$ batteries, but still offers room for improvement. The amorphous structure was deemed to be the key for the good oxygen evolution reaction and oxygen reduction reaction performance that are required during charge and discharge of Li-O$_2$ batteries, respectively.

4.3.3. Supercapacitors

Supercapacitors that offer high power densities, fast charge-discharge cycling, and excellent cycling stability are often thought to bridge the gap between batteries and capacitors. In conventional supercapacitors, the primary charge storage mechanism is the electric double layer capacitance (EDLC), which refers to a layer of charged ions adsorbed on an electrode surface with the opposite charge. On redox active electrodes, an additional pseudocapacitance due to fast faradaic charge transfer occurring on the electrode surface may also be observed, which results in very high capacities at the cost of reduced charge-discharge rates. In the case of TMDCs, the pseudocapacitance contribution can also include intercalation reactions similar to those used in battery electrodes.[365,366]

Nandi et al.[209] used a polycrystalline film MoS$_2$ deposited by the Mo(CO)$_6$+H$_2$S plasma process at 200 °C as a supercapacitor electrode (Figure 16f,g). A very high areal capacitance of 3400 mF cm^{-2} that exceeded previous reports and a reasonable cycling stability (82% capacity retention after 4500 cycles) were achieved for the optimal, ~40 nm thick MoS$_2$ coating on a porous Ni foam substrate. 97% of the capacity was measured to result from faradaic reactions (pseudocapacitance) with only 3% from EDLC.

Ansari et al.[250] used Sn(NMe$_2$)$_4$ and H$_2$S at 160 °C to deposit SnS$_x$ films that predominantly contained the SnS$_2$ phase with a minor SnS contribution. A 50 nm SnS$_x$ film on porous Ni foam performed the best, resulting in an areal capacitance of 800 mF cm^{-2} and retention of more than 90% of the initial capacity after 5000 charge-discharge cycles. The authors estimated the EDLC and pseudocapacitive contributions to be approximately equal.

Zang et al.[290] deposited ALD TiN films on carbon nanotubes and partially converted the TiN to TiS$_2$ in a sulfur atmosphere at 300 °C. The high-surface area substrates coupled with the pseudocapacitive nature of TiS$_2$ enabled a very high gravimetric capacitance, and a record high energy density of 195 F g^{-1} and 60.9 Wh kg^{-1}, respectively, with over 95% capacity retention after 10 000 charge-discharge cycles. The areal capacitance increased 100-fold over the bare carbon nanotubes, although absolute values were not reported.

4.4. Other Applications

Besides electronics, catalysis, and energy storage applications, ALD TMDCs have been studied as lubricating[28,182,185–187,259,367] and plasmonic/photonic coatings[215,248,295] as well as an as absorber[254] and counter-electrode[217] in solar cells. Depending on the application, very different thicknesses from a few ML to hundreds of nanometers have been used (**Figure 17**a). The deposition and annealing temperatures also range widely from below 100 to 850 °C depending on the process and target application.

4.4.1. Lubricating Coatings

Solid lubricating TMDC coatings, particularly MoS$_2$, have been studied and used for decades.[2] ALD enables conformal coating of micro- and nanostructured surfaces, as is required for use in microelectromechanical systems (MEMS). The published studies have demonstrated low friction coefficients of ALD MoS$_2$ and WS$_2$ films, although measurements of ALD TMDCs in actual MEMS devices are still lacking. From the published ALD studies it is not clear how thick films are needed in actual applications, although it is obvious that solid lubricating films wear

during use and as such rather thick films may be required, at least if high loads are applied. So far, either ultrathin (1–10 ML) or over 100 nm thick ALD TMDC films have been used. In terms of film structure, presumably crystalline TMDC films should be preferred as lubricants as they allow individual monolayers to slide on each other. However, the effect of crystallinity and morphology of ALD TMDCs on their lubricant properties is still a somewhat open question.
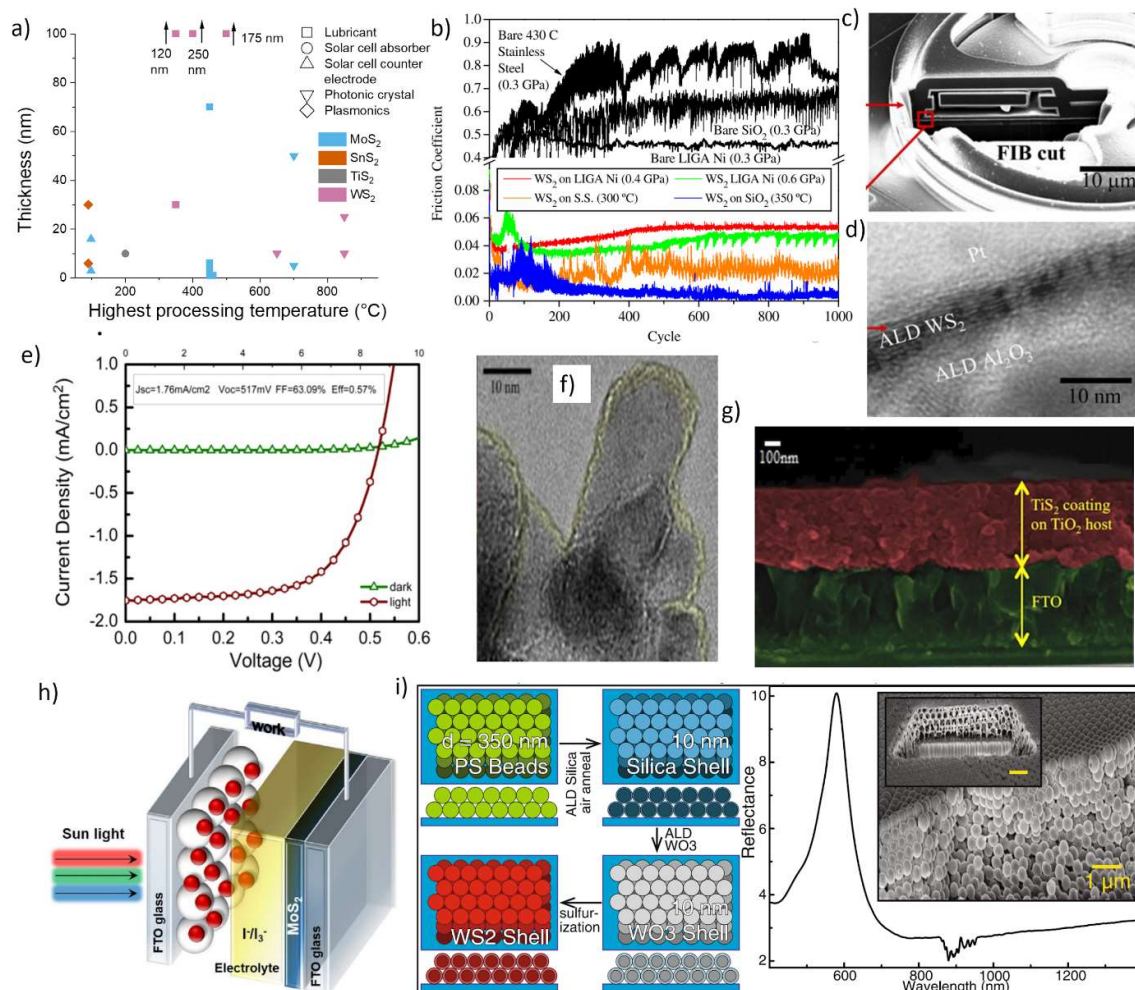
Figure 17. a) Overview of thickness and processing temperature of ALD TMDCs evaluated for other applications (data from Table 2,3). Lubricating ALD WS$_2$ films: b) Friction coefficients of WS$_2$ films on different substrates during cyclic friction testing (bare substrates are shown for reference). c) SEM image of a focused ion beam (FIB) cut of a MEMS structure coated with WS$_2$ and d) TEM image of the WS$_2$ coating inside the high-aspect ratio MEMS device. ALD TiS$_2$ solar cell absorber: e) photocurrent density versus voltage plot (under 1000 mW/cm^2 light intensity), f) cross-sectional TEM image showing the TiS$_2$ coating (colored yellow) on a TiO$_2$ host, and g) cross-sectional SEM image showing the device structure (FTO and TiS$_2$/TiO$_2$ layers artificially colored). h) Schematic of a dye-sensitized solar cell using an ALD MoS$_2$ counter electrode (front-illumination shown, in back illumination light would come from right in the figure). i) WS$_2$ inverse opal photonic crystal: process schematic on the left, reflectance

Early studies by Scharf et al.[28] confirmed that a 250 nm thick ALD WS$_2$ film deposited using WF$_6$ and H$_2$S at 300 °C exhibited a low friction coefficient of 0.09–0.15, which decreased to 0.04 after N$_2$ annealing at 500 °C. In a follow-up study,[259] low friction coefficients of 0.024 and 0.008 were measured for a 120 nm film on stainless steel and a 30 nm film on SiO$_2$, respectively, which are comparable to TMDCs prepared by other methods and much lower than those of the bare substrates (Figure 17b). Conformal coating of MEMS structures was also demonstrated using WS$_2$ layers as thin as 8 nm (Figure 17c,d). Unfortunately, the WF$_6$+H$_2$S process needs a catalytic ZnS layer or intermittent application of ZnEt$_2$ pulses, which results in incorporation of ZnS inclusions with a higher friction coefficient (0.2) in the films.

Sun et al.[367] grew 175 nm thick WS$_2$ films on ZnS and Si substrates using W(CO)$_6$ and H$_2$S at 400 °C. The friction coefficient of the films was measured to be approximately 0.05–0.10. While the friction coefficient was slightly higher for WS$_2$ on ZnS, the coatings on ZnS were also more durable with wear lives of 3600–8000 wear cycles, whereas the coatings on Si failed after 1000 to 1900 cycles.

Huang et al.[183] and Yang and Liu[185] examined the lubricating properties of MoS$_2$ films grown from MoCl$_5$ and H$_2$S at 450–460 °C. Using an atomic force microscope (AFM), the friction force was measured to decrease by 30 to 55% on 3–10 ML thick MoS$_2$ films compared to a bare silicon substrate. Interestingly, the friction force actually increased when a single ML of MoS$_2$ was deposited compared to the bare substrates. The substrate also affected the friction force: the lowest friction was measured for MoS$_2$ films on Al$_2$O$_3$, followed by SiO$_2$ and Si, which was explained by differences in the formed film/substrate interfaces. In a follow-up study, Yang et al.[186] showed that an O$_2$ plasma pre-treatment of an Al$_2$O$_3$ substrate can be used

to decrease the friction force between the AFM tip and monolayer MoS_2 by approximately one third. The decrease was correlated to changes in film morphology resulting from an increased hydroxyl group coverage caused by the plasma treatment.

Using the $MoCl_5+H_2S$ process, Xing et al.[187] deposited a rough, approximately 70 nm thick MoS_2 film on a cemented carbide substrate (WC/TiC/Co) with laser-induced ripples. The authors measured friction coefficients of 0.07–0.08, which were half of that of the bare substrate. Despite the rough morphology, the film appeared to be (quasi)-amorphous. Additionally, the hydrophobicity of the coatings was explored. The highest achieved water contact angle was 135°, which was explained by combined effects of the rippled substrate and the rough, hydrophobic MoS_2 coating.

4.4.2. Plasmonics and Photonics

A few studies have exploited the unbeatable conformality of ALD to make plasmonic and photonic structures. Hägglund et al.[248] constructed plasmonic arrays by depositing 6–30 nm thick amorphous ALD SnS_2 layers on top of Au dots on a SiO_2/Al substrate using $Sn(NMe_2)_4$ and H_2S at 90 °C. A maximum absorbance of 94.2% at 619 nm was observed using an optimized structure (16.4 nm thick SnS_2 layer on top of 7 nm high Au dots separated by 38 nm gaps). The absorption coefficient exceeded 10^7 cm^{-1}, which is one to two orders of magnitude larger compared to most solid metals, the best thin film solar cell absorbers, graphene, and the most strongly absorbing molecular dyes.

Chen et al.[295] created three different kinds of photonic crystals that benefit from the high refractive index of WS_2 (n > 4 for most of the visible and IR range) using sulfurization of ALD WO_3 films into WS_2 at 650 or 850 °C in a H_2S ambient. First, two-dimensional patterned photonic crystals consisting of a WS_2 film with 335 nm diameter holes on a flat quartz substrate were created. By changing the WS_2 film thickness (10–25 nm) and pitch (590–630 nm), the wavelengths of transmission resonances could be varied by about 200 nm. Alternatively, the

holes could be etched into the quartz substrate followed by preparation of a conformal WS$_2$ film on top, with a similar performance. The third demonstrated photonic structure was a three-dimensional inverse-opal photonic crystal. A 10 nm WS$_2$ / 10 nm SiO$_2$ stack grown onto a layer of self-assembled 350 nm poly(styrene) beads resulted in a strong stop band reflection peak at a wavelength of approximately 600 nm (Figure 17i).

Li et al.[215] prepared a similar three-dimensional TiO$_2$/MoS$_2$ core-shell inverse opal structure by ALD. Following TiO$_2$ ALD onto a self-assembled poly(styrene) opal template and its calcination, the MoS$_2$ layer was grown from Mo(CO)$_6$ and MeSSMe and crystallized by Ar annealing at 650–700 °C. Distinct stop band reflection peaks with reflectance of up to 90% were achieved. The specific wavelength was tunable by the inverse opal size and the MoS$_2$ thickness. The authors suggested such photonic crystals to be useful as absorbers in solar cells.

4.4.3. Solar Cells

Mahuli and Sarkar[254] used ALD grown TiS$_2$ as an absorber layer in a solid state sensitized solar cell. An approximately 10 nm thick nanocrystalline TiS$_2$ layer conformally deposited on a porous TiO$_2$ substrate resulted in a modest power conversion efficiency (PCE) of 0.57% (Figure 17e–g). Further studies on optimizing the device structure to improve the performance as well as using a similar approach for semiconducting TMDCs with a larger band gap as absorbers would be interesting. It is known that a single monolayer of TMDC can absorb as much as 10% of the solar spectrum,[368] which may enable solar cells with a competitive PCE especially if deposited on a nanostructured substrate.

Jeong et al.[217] used amorphous ALD MoS$_2$ films as counter electrodes in dye-sensitized solar cells (Figure 17h). Under front-illumination conditions, the thickest examined, 16 nm MoS$_2$ film resulted in the best PCE of 6.88% due to its highest conductivity. The PCE is relatively close to that achieved with the commonly used Pt electrode (7.46%). On the other hand, under back-illumination (light passing through the MoS$_2$ electrode), for which Pt is not applicable,

the thinnest 3 nm MoS_2 layer performed the best with a PCE 4.28% due to its highest transparency.

5. Conclusions and Future Outlook

Layered TMDCs are a versatile group of materials with unique physical and chemical properties. Besides the most commonly studied semiconducting sulfides and selenides of molybdenum and tungsten, there are many other semiconducting as well as (semi)metallic TMDCs. The research on TMDCs is thriving and new advances in their physical and chemical properties and applications alike are uncovered at an ever increasing pace. However, synthesis of TMDCs at reasonable cost for real-world applications is still a challenge and requires deposition methods that are scalable, repeatable, and integrable into production lines. The TMDC crystallinity and thickness need to be tuned for different applications and for some applications there may be stringent restrictions on the temperatures used.

ALD is an advanced industrially used thin film deposition method that offers excellent control over film deposition and produces uniform and conformal films at comparably mild conditions. These perks of ALD are difficult to match by other techniques used to deposit TMDCs, and the number of publications using ALD to deposit TMDCs has increased rapidly. Most of the ALD studies have focused on MoS_2 with several reports published also on SnS_2 and WS_2, and to a lower degree $MoSe_2$, TiS_2, WS_2, and WSe_2. The recent new processes for HfS_2, ZrS_2, and ReS_2 are noteworthy, as these TMDCs have been scarcely studied by the TMDC community. Unfortunately, though, ALD characteristics of many of the reported processes have not yet been examined and some of the processes are hardly ideal in terms of their growth characteristics or the high deposition and post-deposition annealing temperatures required. Thus, new ALD processes for all of the materials studied should still be sought for.

Comparison of the list of ALD TMDCs deposited (9 binary materials) to the list of layered TMDCs (~30–40 materials) shows that there is plenty of room to expand the material selection.

In particular, most of the ALD TMDCs deposited to date are semiconductors (excluding TiS_2 and metastable 1T MoS_2), while many of the potential applications, such as electrocatalysis, LIBs, NIBs, and supercapacitors, do not require semiconductors and benefit from high electrical conductivity. Therefore, ALD processes for metallic TMDCs, such as those of group 5 metals, should be looked for. Furthermore, although sulfide TMDCs are easier to work on regarding their deposition as well as stability in the atmosphere, it is hoped that more attention will be put on deposition of selenide and telluride TMDCs. Considering the facile deposition of ternary, quaternary, and even more complex materials by ALD, it seems reasonable to expect studies demonstrating tuning of the material properties by alloying. Heterostructures also offer fascinating possibilities, and further studies on their preparation and characterization would be of interest.

ALD TMDCs are increasingly evaluated for various applications, each of which pose their own requirements for film crystallinity, thickness, and deposition conditions. The published studies along with the enormous body of TMDC literature have revealed general trends between physicochemical properties of TMDCs and their performance in different applications, which couples closely to the understanding and tuning of these properties through the ALD growth processes. This interplay of ALD process and precursor development, film characterization, and evaluation of performance in different applications, is crucial for bringing ALD TMDCs toward practical applications. Thus, also in-depth studies on issues such as nucleation, grain size tuning, and evolution of morphology using a range of ALD processes and deposition conditions are needed.

Nearly half of the published application oriented ALD TMDC papers have focused on electronic and optoelectronic applications, in particular FETs. FETs pose some of the highest film quality requirements out of the commonly studied TMDC applications, and smooth and highly crystalline films from one to about ten ML thick seem to perform the best. Although achieving this usually requires the use of high deposition or post-deposition annealing

temperatures, it is promising that there are also a few examples of good FET performance of ALD MoS_2, WS_2, and WSe_2 films processed under mild conditions (<500 °C). Besides these, well crystallized SnS_2 FETs have been produced at temperatures as low as 250 °C, and the most recent studies have reported performance enhancements up to a level that could be suitable for flexible electronics, for example. Furthermore, there seems to be room for optimization of ALD processes as well as device structures for improved FET performance. Examples of the latter include deposition of metallic TMDCs as contacts to semiconducting FET channels as well as gate dielectric deposition by ALD, which is an application where ALD is known to excel in. Successful demonstrations of other devices that could be integrated onto CMOS platforms and beyond, including photodetectors, gas sensors, and biosensors also underline the applicability of ALD TMDCs in electronics.

Electrocatalysis, photocatalysis, and photoelectrocatalysis make up approximately one fifth of ALD TMDC application studies. In these applications, crystalline films with a rough morphology and defective nature or even amorphous films have performed the best. Deposition on high surface area substrates, which is very natural for ALD, is an effective approach to improve the catalyst performance. A large portion of the catalyst studies have focused on electrocatalytic water splitting, especially HER. The HER performance of the best ALD TMDC catalysts is comparable to some of the best results reported in literature, which should motivate more detailed studies on the density and type of active sites present on the ALD TMDC films. The few studies on OER have demonstrated good performance, which warrants testing more films for this reaction, too. Considering the cost of practical catalysts, studies should also explore minimizing the amount of ALD TMDC catalyst deposited as well as other strategies for cost reduction. ALD TMDCs have also shown promise in initial studies for photoelectrocalytic water splitting in combination with various semiconductors, as well as solution and gas-phase photocatalysis.

In energy storage, ALD TMDCs have been tested as anodes for LIBs and NIBs and as supercapacitor electrodes. In the battery applications, rather thick films from tens of nm upward deposited at relatively low temperatures have been used. High gravimetric capacities and reasonably good charge-discharge cycling stabilities of anodes prepared on planar substrates have been published. Deposition on 3D structures and using the ALD TMDC anodes with solid electrolytes may be useful routes for making practical thin film batteries, at least for some niche applications. In supercapacitors, the pseudocapacitive component of TMDCs along with the conformality of ALD on 3D substrates have been shown to enable high capacitance densities.

Other applications that ALD TMDCs have been studied for include lubricating coatings for demanding MEMS structures, photonic crystals and plasmonic arrays on complicated 3D templates, and absorber layers in solar cells with a porous architecture. All of these greatly benefit from the excellent conformality of ALD. It seems likely that ALD TMDCs could also be successfully used for many other applications where conformal TMDC coatings are required.

The aim of this review is not only compiling the studies and processes of ALD grown TMDCs, but also placing ALD with its pros and cons in context with other TMDC deposition methods and identifying some of the challenges and opportunities in TMDC ALD. Above all, we have focused on an early assessment of the potential of ALD toward different applications. We believe that rational selection of factors such as ALD processes, depositions conditions, film thicknesses, and substrates will help in further improving the performance of ALD TMDCs in various applications.

References

[1]   R. G. Dickinson, L. Pauling, *J. Am. Chem. Soc.* **1923**, *45*, 1466.

[2]   J. P. G. Farr, *Wear* **1975**, *35*, 1.

[3]   W. O. Winer, *Wear* **1967**, *10*, 422.

[4]   J. V. Lauritsen, F. Besenbacher, *J. Catal.* **2015**, *328*, 49.

[5]   J. A. Wilson, A. D. Yoffe, *Adv. Phys.* **1969**, *18*, 193.

[6]   F. Hulliger, in *Structure and Bonding*, Vol. 4 (Eds.: C. K. Jørgensen, J. B. Neilands, R. S. Nyholm, D. Reinen, R. J. P. Williams), Springer-Verlag, Berlin, Germany **1968**, Ch. 3.

[7]   M. S. Whittingham, *Science* **1976**, *192*, 1126.

[8]   P. Joensen, R. F. Frindt, S. R. Morrison, *Mater. Res. Bull.* **1986**, *21*, 457.

[9]   A. Klein, S. Tiefenbacher, V. Eyert, C. Pettenkofer, W. Jaegermann, *Thin Solid Films* **2000**, *380*, 221.

[10]   K. S. Novoselov, D. Jiang, F. Schedin, T. J. Booth, V. V. Khotkevich, S. V. Morozov, A. K. Geim, *Proc. Natl. Acad. Sci. U. S. A.* **2005**, *102*, 10451.

[11]   K. S. Novoselov, A. K. Geim, S. V. Morozov, D. Jiang, Y. Zhang, S. V. Dubonos, I. V. Grigorieva, A. A. Firsov, *Science* **2004**, *306*, 666.

[12]   A. K. Geim, *Science* **2009**, *324*, 1530.

[13]   Graphene Flagship, http://graphene-flagship.eu/, accessed: May, 2020.

[14]   C. Backes, A. M. Abdelkader, C. Alonso, A. Andrieux-Ledier, R. Arenal, J. Azpeitia, N. Balakrishnan, L. Banszerus, J. Barjon, R. Bartali, S. Bellani, C. Berger, R. Berger, M. M. B. Ortega, C. Bernard, P. H. Beton, A. Beyer, A. Bianco, P. Bøggild, F. Bonaccorso, G. B. Barin, C. Botas, R. A. Bueno, D. Carriazo, A. Castellanos-Gomez, M. Christian, A. Ciesielski, T. Ciuk, M. T. Cole, J. Coleman, C. Coletti, L. Crema, H. Cun, D. Dasler, D. De Fazio, N. Díez, S. Drieschner, G. S. Duesberg, R. Fasel, X. Feng, A. Fina, S. Forti, C. Galiotis, G. Garberoglio, J. M. García, J. A. Garrido, M. Gibertini, A. Gölzhäuser, J. Gómez,

T. Greber, F. Hauke, A. Hemmi, I. Hernandez-Rodriguez, A. Hirsch, S. A. Hodge, Y. Huttel, P. U. Jepsen, I. Jimenez, U. Kaiser, T. Kaplas, H. Kim, A. Kis, K. Papagelis, K. Kostarelos, A. Krajewska, K. Lee, C. Li, H. Lipsanen, A. Liscio, M. R. Lohe, A. Loiseau, L. Lombardi, M. Francisca López, O. Martin, C. Martín, L. Martínez, J. A. Martin-Gago, J. Ignacio Martínez, N. Marzari, Á. Mayoral, J. McManus, M. Melucci, J. Méndez, C. Merino, P. Merino, A. P. Meyer, E. Miniussi, V. Miseikis, N. Mishra, V. Morandi, C. Munuera, R. Muñoz, H. Nolan, L. Ortolani, A. K. Ott, I. Palacio, V. Palermo, J. Parthenios, I. Pasternak, A. Patane, M. Prato, H. Prevost, V. Prudkovskiy, N. Pugno, T. Rojo, A. Rossi, P. Ruffieux, P. Samorì, L. Schué, E. Setijadi, T. Seyller, G. Speranza, C. Stampfer, I. Stenger, W. Strupinski, Y. Svirko, S. Taioli, K. B. K. Teo, M. Testi, F. Tomarchio, M. Tortello, E. Treossi, A. Turchanin, E. Vazquez, E. Villaro, P. R. Whelan, Z. Xia, R. Yakimova, S. Yang, G. R. Yazdi, C. Yim, D. Yoon, X. Zhang, X. Zhuang, L. Colombo, A. C. Ferrari, M. Garcia-Hernandez, *2D Mater.* **2020**, *7*, 022001.

[15]   A. Kuc, N. Zibouche, T. Heine, *Phys. Rev. B* **2011**, *83*, 245213.

[16]   K. F. Mak, C. Lee, J. Hone, J. Shan, T. F. Heinz, *Phys. Rev. Lett.* **2010**, *105*, 136805.

[17]   Y.-H. Lee, X.-Q. Zhang, W. Zhang, M.-T. Chang, C.-T. Lin, K.-D. Chang, Y.-C. Yu, J. T.-W. Wang, C.-S. Chang, L.-J. Li, T.-W. Lin, *Adv. Mater.* **2012**, *24*, 2320.

[18]   Y. Zhan, Z. Liu, S. Najmaei, P. M. Ajayan, J. Lou, *Small* **2012**, *8*, 966.

[19]   B. Radisavljevic, A. Radenovic, J. Brivio, V. Giacometti, A. Kis, *Nat. Nanotechnol.* **2011**, *6*, 147.

[20]   O. Lopez-Sanchez, D. Lembke, M. Kayci, A. Radenovic, A. Kis, *Nat. Nanotechnol.* **2013**, *8*, 497.

[21]   H. Li, Z. Yin, Q. He, H. Li, X. Huang, G. Lu, D. W. H. Fam, A. I. Y. Tok, Q. Zhang, H. Zhang, *Small* **2012**, *8*, 63.

[22]   J. Zhou, J. Lin, X. Huang, Y. Zhou, Y. Chen, J. Xia, H. Wang, Y. Xie, H. Yu, J. Lei,

D. Wu, F. Liu, Q. Fu, Q. Zeng, C.-H. Hsu, C. Yang, L. Lu, T. Yu, Z. Shen, H. Lin, B. I.

Yakobson, Q. Liu, K. Suenaga, G. Liu, Z. Liu, *Nature* **2018**, *556*, 355.

[23]   L. J. Li, E. C. T. O'Farrell, K. P. Loh, G. Eda, B. Özyilmaz, A. H. Castro Neto, *Nature*

2016, *529*, 185.

[24]   A. Kogar, M. S. Rak, S. Vig, A. A. Husain, F. Flicker, Y. Il Joe, L. Venema, G. J.

MacDougall, T. C. Chiang, E. Fradkin, J. van Wezel, P. Abbamonte, *Science* **2017**, *358*, 1314.

[25]   S. Manzeli, D. Ovchinnikov, D. Pasquier, O. V. Yazyev, A. Kis, *Nat. Rev. Mater.*

2017, *2*, 17033.

[26]   M. Samadi, N. Sarikhani, M. Zirak, H. Zhang, H.-L. Zhang, A. Z. Moshfegh,

Nanoscale Horizons **2018**, *3*, 90.

[27]   B. Hinnemann, P. G. Moses, J. Bonde, K. P. Jørgensen, J. H. Nielsen, S. Horch, I.

Chorkendorff, J. K. Nørskov, *J. Am. Chem. Soc.* **2005**, *127*, 5308.

[28]   T. W. Scharf, S. V. Prasad, T. M. Mayer, R. S. Goeke, M. T. Dugger, *J. Mater. Res.*

2004, *19*, 3443.

[29]   L. K. Tan, B. Liu, J. H. Teng, S. Guo, H. Y. Low, K. P. Loh, *Nanoscale* **2014**, *6*,

10584.

[30]   Y. Gong, J. Lin, X. Wang, G. Shi, S. Lei, Z. Lin, X. Zou, G. Ye, R. Vajtai, B.

Yakobson, H. Terrones, M. Terrones, B. K. Tay, J. Lou, S. T. Pantelides, Z. Liu, W. Zhou, P.

M. Ajayan, *Nat. Mater.* **2014**, *13*, 1135.

[31]   C. Liu, Y. Xiao, X. Song, S. Ding, D. W. Zhang, P. Zhou, *Nat. Nanotechnol.* **2018**, *13*,

404.

[32]   V. K. Sangwan, H.-S. Lee, H. Bergeron, I. Balla, M. E. Beck, K.-S. Chen, M. C.

Hersam, *Nature* **2018**, *554*, 500.

[33]   C. Zhu, Z. Zeng, H. Li, F. Li, C. Fan, H. Zhang, *J. Am. Chem. Soc.* **2013**, *135*, 5998.

[34] M. Chhowalla, H. S. Shin, G. Eda, L.-J. Li, K. P. Loh, H. Zhang, *Nat. Chem.* **2013**, *5*, 263.

[35] H. Yang, S. W. Kim, M. Chhowalla, Y. H. Lee, *Nat. Phys.* **2017**, *13*, 931.

[36] M. Hossain, Z. Zhao, W. Wen, X. Wang, J. Wu, L. Xie, *Crystals* **2017**, *7*, 298.

[37] K. Kang, S. Xie, L. Huang, Y. Han, P. Y. Huang, K. F. Mak, C.-J. Kim, D. Muller, J. Park, *Nature* **2015**, *520*, 656.

[38] Y.-C. Lin, B. Jariwala, B. M. Bersch, K. Xu, Y. Nie, B. Wang, S. M. Eichfeld, X. Zhang, T. H. Choudhury, Y. Pan, R. Addou, C. M. Smyth, J. Li, K. Zhang, M. A. Haque, S. Fölsch, R. M. Feenstra, R. M. Wallace, K. Cho, S. K. Fullerton-Shirey, J. M. Redwing, J. A. Robinson, *ACS Nano* **2018**, *12*, 965.

[39] P. K. Sahoo, S. Memaran, Y. Xin, L. Balicas, H. R. Gutiérrez, *Nature* **2018**, *553*, 63.

[40] M. Ritala, M. Leskelä, in *Handbook of Thin Film Materials* (Ed.: H. S. Nalwa), Academic, San Diego, USA **2002**, Ch. 2.

[41] M. Ritala, J. Niinistö, in *Chemical Vapour Deposition: Precursors, Processes and Applications* (Eds.: A. C. Jones, M. L. Hitchman), Royal Society Of Chemistry, Cambridge, UK **2009**, Ch. 4.

[42] R. L. Puurunen, *J. Appl. Phys.* **2005**, *97*, 121301.

[43] S. M. George, *Chem. Rev.* **2010**, *110*, 111.

[44] M. Leskelä, J. Niinistö, M. Ritala, in *Comprehensive Materials Processing*, Vol. 4 (Eds.: S. Hashmi, D. Cameron), Elsevier, Amsterdam, The Netherlands **2014**, Ch. 4.05.

[45] M. Ritala, J. Niinistö, *ECS Trans.* **2009**, *25*, (8), 641.

[46] I. J. Raaijmakers, *ECS Trans.* **2011**, *41*, (2), 3.

[47] M. Leskelä, M. Mattinen, M. Ritala, *J. Vac. Sci. Technol. B* **2019**, *37*, 030801.

[48] W. Hao, C. Marichy, C. Journet, *2D Mater.* **2019**, *6*, 012001.

[49] Y. Huang, L. Liu, *Sci. China Mater.* **2019**, *62*, 913.

[50] J. Cai, X. Han, X. Wang, X. Meng, *Matter* **2020**, *2*, 587.

[51]   K. Momma, F. Izumi, *J. Appl. Crystallogr.* **2011**, *44*, 1272.

[52]   International crystal structure database (ICSD), https://icsd.fiz-

karlsruhe.de/index.xhtml, accessed: August, 2019.

[53]   S. Jobic, R. Brec, J. Rouxel, *J. Solid State Chem.* **1992**, *96*, 169.

[54]   F. Grønvold, E. Røst, *Acta Crystallogr.* **1957**, *10*, 329.

[55]   S. Jobic, P. Deniard, R. Brec, J. Rouxel, M. G. B. Drew, W. I. F. David, *J. Solid State

Chem.* **1990**, *89*, 315.

[56]   C. Yan, C. Gong, P. Wangyang, J. Chu, K. Hu, C. Li, X. Wang, X. Du, T. Zhai, Y. Li,

J. Xiong, *Adv. Funct. Mater.* **2018**, *28*, 1803305.

[57]   M. Abdulsalam, D. P. Joubert, *Phys. Status Solidi B* **2016**, *253*, 705.

[58]   A. Stoliaroff, S. Jobic, C. Latouche, *Inorg. Chem.* **2019**, *58*, 1949.

[59]   S. Jiang, Z. Zhang, M. Hong, P. Yang, Y. Zhang, G. Zhao, J. Shi, *Nanotechnology*

2019, *30*, 182002.

[60]   G. H. Han, D. L. Duong, D. H. Keum, S. J. Yun, Y. H. Lee, *Chem. Rev.* **2018**, *118*,

6297.

[61]   J. Li, B. Zhao, P. Chen, R. Wu, B. Li, Q. Xia, G. Guo, J. Luo, K. Zang, Z. Zhang, H.

Ma, G. Sun, X. Duan, X. Duan, *Adv. Mater.* **2018**, *30*, 1801043.

[62]   G. Wang, A. Chernikov, M. M. Glazov, T. F. Heinz, X. Marie, T. Amand, B.

Urbaszek, *Rev. Mod. Phys.* **2018**, *90*, 021001.

[63]   Y. Fang, J. Pan, J. He, R. Luo, D. Wang, X. Che, K. Bu, W. Zhao, P. Liu, G. Mu, H.

Zhang, T. Lin, F. Huang, *Angew. Chem., Int. Ed.* **2018**, *57*, 1232.

[64]   H. Xu, D. Han, Y. Bao, F. Cheng, Z. Ding, S. J. R. Tan, K. P. Loh, *Nano Lett.* **2018**,

18, 5085.

[65]   P. Li, Y. Wen, X. He, Q. Zhang, C. Xia, Z.-M. Yu, S. A. Yang, Z. Zhu, H. N.

Alshareef, X.-X. Zhang, *Nat. Commun.* **2017**, *8*, 2150.

[66] D. A. Chenet, O. B. Aslan, P. Y. Huang, C. Fan, A. M. van der Zande, T. F. Heinz, J. C. Hone, *Nano Lett.* **2015**, *15*, 5667.

[67] J. C. Wildervanck, F. Jellinek, *J. Less-Common Met.* **1971**, *24*, 73.

[68] X. Zhou, Q. Zhang, L. Gan, H. Li, J. Xiong, T. Zhai, *Adv. Sci.* **2016**, *3*, 1600177.

[69] J. Shi, Y. Huan, M. Hong, R. Xu, P. Yang, Z. Zhang, X. Zou, Y. Zhang, *ACS Nano* **2019**, *13*, 842.

[70] M. Mattinen, *PhD Thesis*, University of Helsinki, Finland, April, **2020**. Available at https://helda.helsinki.fi/handle/10138/313094

[71] S. Tongay, H. Sahin, C. Ko, A. Luce, W. Fan, K. Liu, J. Zhou, Y.-S. Huang, C.-H. Ho, J. Yan, D. F. Ogletree, S. Aloni, J. Ji, S. Li, J. Li, F. M. Peeters, J. Wu, *Nat. Commun.* **2014**, *5*, 3252.

[72] Y. Zhao, J. Qiao, P. Yu, Z. Hu, Z. Lin, S. P. Lau, Z. Liu, W. Ji, Y. Chai, *Adv. Mater.* **2016**, *28*, 2399.

[73] D. H. Keum, S. Cho, J. H. Kim, D.-H. Choe, H.-J. Sung, M. Kan, H. Kang, J.-Y. Hwang, S. W. Kim, H. Yang, K. J. Chang, Y. H. Lee, *Nat. Phys.* **2015**, *11*, 482.

[74] S. Dissanayake, C. Duan, J. Yang, J. Liu, M. Matsuda, C. Yue, J. A. Schneeloch, J. C. Y. Teo, D. Louca, *npj Quantum Mater.* **2019**, *4*, 45.

[75] X. Wang, Z. Song, W. Wen, H. Liu, J. Wu, C. Dang, M. Hossain, M. A. Iqbal, L. Xie, *Adv. Mater.* **2018**, *31*, *1804682*.

[76] M. S. Sokolikova, C. Mattevi, *Chem. Soc. Rev.* **2020**, *49*, 3952.

[77] S. Susarla, A. Kutana, J. A. Hachtel, V. Kochat, A. Apte, R. Vajtai, J. C. Idrobo, B. I. Yakobson, C. S. Tiwary, P. M. Ajayan, *Adv. Mater.* **2017**, *29*, 1702457.

[78] K. Kang, K.-H. Lee, Y. Han, H. Gao, S. Xie, D. A. Muller, J. Park, *Nature* **2017**, *550*, 229.

[79]   N. Finney, A. Antony, T. Schiros, T. Klarr, A. Mazzoni, M. Chin, Y. Chiu, W. Zheng, R. M. Osgood, D. W. Paley, A. M. Lindenberg, P. Y. Huang, A. N. Pasupathy, M. Dubey, J. Hone, L. Balicas, *Nano Lett.* **2017**, *17*, 1616.

[80]   A. Rai, H. Movva, A. Roy, D. Taneja, S. Chowdhury, S. Banerjee, *Crystals* **2018**, *8*, 316.

[81]   M. W. Iqbal, E. Elahi, A. Amin, G. Hussain, S. Aftab, *Superlattices Microstruct.* **2020**, *137*, 106350.

[82]   Q. Zeng, Z. Liu, *Adv. Electron. Mater.* **2018**, *4*, 1700335.

[83]   K. S. Novoselov, A. Mishchenko, A. Carvalho, A. H. Castro Neto, *Science* **2016**, *353*, aac9439.

[84]   R. Dong, I. Kuljanishvili, *J. Vac. Sci. Technol. B* **2017**, *35*, 030803.

[85]   T. Zhang, L. Fu, *Chem* **2018**, *4*, 671.

[86]   H. Qi, L. Wang, J. Sun, Y. Long, P. Hu, F. Liu, X. He, *Crystals* **2018**, *8*, 35.

[87]   Y. Sun, R. Wang, K. Liu, *Appl. Phys. Rev.* **2017**, *4*, 011301.

[88]   J. Liu, G. M. Choi, D. G. Cahill, *J. Appl. Phys.* **2014**, *116*, 233107.

[89]   A. M. Hermann, R. Somoano, V. Hadek, A. Rembaum, *Solid State Commun.* **1973**, *13*, 1065.

[90]   R. C. Longo, R. Addou, K. C. Santosh, J. Y. Noh, C. M. Smyth, D. Barrera, C. Zhang, J. W. P. Hsu, R. M. Wallace, K. Cho, *2D Mater.* **2017**, *4*, 025050.

[91]   A. Dabral, A. K. A. Lu, D. Chiappe, M. Houssa, G. Pourtois, *Phys. Chem. Chem. Phys.* **2019**, *21*, 1089.

[92]   Z. Lin, A. McCreary, N. Briggs, S. Subramanian, K. Zhang, Y. Sun, X. Li, N. J. Borys, H. Yuan, S. K. Fullerton-Shirey, A. Chernikov, H. Zhao, S. McDonnell, A. M. Lindenberg, K. Xiao, B. J. LeRoy, M. Drndić, J. C. M. Hwang, J. Park, M. Chhowalla, R. E. Schaak, A. Javey, M. C. Hersam, J. Robinson, M. Terrones, *2D Mater.* **2016**, *3*, 042001.

[93]   Q. Li, Q. Zhou, L. Shi, Q. Chen, J. Wang, *J. Mater. Chem. A* **2019**, *7*, 4291.

[94]   H. Şar, A. Özden, İ. Demiroğlu, C. Sevik, N. K. Perkgoz, F. Ay, *Phys. Status Solidi RRL* **2019**, *13*, 1800687.

[95]   G. Mirabelli, C. McGeough, M. Schmidt, E. K. McCarthy, S. Monaghan, I. M. Povey, M. McCarthy, F. Gity, R. Nagle, G. Hughes, A. Cafolla, P. K. Hurley, R. Duffy, *J. Appl. Phys.* **2016**, *120*, 125102.

[96]   J. Shi, M. Hong, Z. Zhang, Q. Ji, Y. Zhang, *Coord. Chem. Rev.* **2018**, *376*, 1.

[97]   M. J. Mleczko, C. Zhang, H. R. Lee, H.-H. Kuo, B. Magyari-Köpe, R. G. Moore, Z.-X. Shen, I. R. Fisher, Y. Nishi, E. Pop, *Sci. Adv.* **2017**, *3*, e1700481.

[98]   R. Zhao, B. Grisafe, R. K. Ghosh, S. Holoviak, B. Wang, K. Wang, N. Briggs, A. Haque, S. Datta, J. Robinson, *2D Mater.* **2018**, *5*, 025001.

[99]   M. Mattinen, P. J. King, L. Khriachtchev, K. Meinander, J. T. Gibbon, V. R. Dhanak, J. Räisänen, M. Ritala, M. Leskelä, *Small* **2018**, *14*, 1800547.

[100]   B. Groven, M. Heyne, A. N. Mehta, H. Bender, T. Nuytten, J. Meersschaut, T. Conard, P. Verdonck, S. van Elshocht, W. Vandervorst, S. de Gendt, M. Heyns, I. Radu, M. Caymax, A. Delabie, *Chem. Mater.* **2017**, *29*, 2927.

[101]   V. Miikkulainen, M. Leskelä, M. Ritala, R. L. Puurunen, *J. Appl. Phys.* **2013**, *113*, 021301.

[102]   A. L. Johnson, J. D. Parish, in *Organometallic Chemistry,* Vol. 42 (Eds.: N. J. Patmore, P. I. Elliott), Royal Society of Chemistry, Cambridge, UK **2018**, Ch. 1.

[103]   ALD Database, https://www.atomiclimits.com/alddatabase/, accessed: May, 2020.

[104]   V. Pore, T. Hatanpää, M. Ritala, M. Leskelä, *J. Am. Chem. Soc.* **2009**, *131*, 3478.

[105]   A. Sharma, M. A. Verheijen, L. Wu, S. Karwal, V. Vandalon, H. C. M. Knoops, R. S. Sundaram, J. P. Hofmann, W. M. M. Kessels, A. A. Bol, *Nanoscale* **2018**, *10*, 8615.

[106]   Z. Guo, X. Wang, *Angew. Chem.: Int. Ed.* **2018**, *57*, 5898.

[107]   S. Balasubramanyam, M. A. Bloodgood, M. van Ommeren, T. Faraz, V. Vandalon, W. M. M. Kessels, M. A. Verheijen, A. A. Bol, *ACS Appl. Mater. Interfaces* **2020**, *12*, 3873.

WILEY-VCH

[108]   R. L. Puurunen, W. Vandervorst, *J. Appl. Phys.* **2004**, *96*, 7686.

[109]   T. Park, H. Kim, M. Leem, W. Ahn, S. Choi, J. Kim, J. Uh, K. Kwon, S.-J. Jeong, S. Park, Y. Kim, H. Kim, *RSC Adv.* **2017**, *7*, 884.

[110]   F. Grillo, H. van Bui, J. A. Moulijn, M. T. Kreutzer, J. R. van Ommen, *J. Phys. Chem. Lett.* **2017**, *8*, 975.

[111]   B. Groven, A. Nalin Mehta, H. Bender, J. Meersschaut, T. Nuytten, P. Verdonck, T. Conard, Q. Smets, T. Schram, B. Schoenaers, A. Stesmans, V. Afanasiev, W. Vandervorst, M. Heyns, M. Caymax, I. Radu, A. Delabie, *Chem. Mater.* **2018**, *30*, 7648.

[112]   J. A. Venables, *Surf. Sci.* **1994**, *299/300*, 798.

[113]   P. B. Barna, M. Adamik, *Thin Solid Films* **1998**, *317*, 27.

[114]   CRC Handbook of Chemistry and Physics online, http://www.hbcpnetbase.com/, accessed: May, 2020.

[115]   T. Wu, X. Zhang, Q. Yuan, J. Xue, G. Lu, Z. Liu, H. Wang, H. Wang, F. Ding, Q. Yu, X. Xie, M. Jiang, *Nat. Mater.* **2016**, *15*, 43.

[116]   J. Yang, P. Hu, G. Yu, *2D Mater.* **2019**, *6*, 042003.

[117]   Y. Zhang, Y. Yao, M. G. Sendeku, L. Yin, X. Zhan, F. Wang, Z. Wang, J. He, *Adv. Mater.* **2019**, *31*, 1901694.

[118]   W. Jeon, Y. Cho, S. Jo, J.-H. Ahn, S.-J. Jeong, *Adv. Mater.* **2017**, *29*, 1703031.

[119]   J. Yang, L. Liu, *ACS Appl. Mater. Interfaces* **2019**, *11*, 36270.

[120]   A. J. M. Mackus, M. J. M. Merkx, W. M. M. Kessels, *Chem. Mater.* **2019**, *31*, 2.

[121]   S. Balasubramanyam, M. J. M. Merkx, M. A. Verheijen, W. M. M. Kessels, A. J. M. Mackus, A. A. Bol, *ACS Mater. Lett.* **2020**, *2*, 511.

[122]   C. Yue, Y. Wang, H. Liu, L. Chen, H. Zhu, Q. Sun, *J. Cryst. Growth* **2020**, *541*, 125683.

[123]   M. Mattinen, T. Hatanpää, T. Sarnet, K. Mizohata, K. Meinander, P. J. King, L. Khriachtchev, J. Räisänen, M. Ritala, M. Leskelä, *Adv. Mater. Interfaces* **2017**, *4*, 1700213.

[124] B. Groven, *PhD Thesis*, KU Leuven, Belgium, December, **2018**. Availale at

https://lirias.kuleuven.be/retrieve/524443

[125] A. Sharma, R. Mahlouji, L. Wu, M. A. Verheijen, V. Vandalon, S. Balasubramanyam,

J. P. Hofmann, W. M. M. Kessels, A. A. Bol, *Nanotechnology* **2020**, *31*, 255603.

[126] M. Mattinen, P. J. King, G. Popov, J. Hämäläinen, M. J. Heikkilä, M. Leskelä, M.

Ritala, *2D Mater.* **2020**, *7*, 011003.

[127] A. J. Mughal, T. N. Walter, K. A. Cooley, A. Bertuch, S. E. Mohney, *J. Vac. Sci.

Technol. A* **2019**, *37*, 010907.

[128] B. Groven, A. N. Mehta, H. Bender, Q. Smets, J. Meersschaut, A. Franquet, T.

Conard, T. Nuytten, P. Verdonck, W. Vandervorst, M. Heyns, I. Radu, M. Caymax, A.

Delabie, *J. Vac. Sci. Technol. A* **2018**, *36*, 01A105.

[129] A. Koma, *Thin Solid Films* **1992**, *216*, 72.

[130] L. A. Walsh, C. L. Hinkle, *Appl. Mater. Today* **2017**, *9*, 504.

[131] M. Mattinen, P. J. King, P. Brüner, M. Leskelä, M. Ritala, *Adv. Mater. Interfaces*

2020, *7*, 2001046.

[132] M. Shirazi, W. M. M. Kessels, A. A. Bol, *Phys. Chem. Chem. Phys.* **2018**, *20*, 16861.

[133] M. Shirazi, W. M. M. Kessels, A. A. Bol, *APL Mater.* **2018**, *6*, 111107.

[134] M. Mattinen, T. Hatanpää, P. J. King, K. Meinander, K. Mizohata, P. Jalkanen, J.

Räisänen, M. Ritala, M. Leskelä, *J. Vac. Sci. Technol. A* **2019**, *37*, 020921.

[135] G. Ham, S. Shin, J. Park, J. Lee, H. Choi, S. Lee, H. Jeon, *RSC Adv.* **2016**, *6*, 54069.

[136] D. Neumaier, S. Pindl, M. C. Lemme, *Nat. Mater.* **2019**, *18*, 525.

[137] L. Lin, H. Peng, Z. Liu, *Nat. Mater.* **2019**, *18*, 520.

[138] C. Backes, T. M. Higgins, A. Kelly, C. Boland, A. Harvey, D. Hanlon, J. N. Coleman,

Chem. Mater. **2017**, *29*, 243.

[139] H. Schmidt, S. Wang, L. Chu, M. Toh, R. Kumar, W. Zhao, A. H. Castro Neto, J.

Martin, S. Adam, B. Özyilmaz, G. Eda, *Nano Lett.* **2014**, *14*, 1909.

[140] R. Gatensby, T. Hallam, K. Lee, N. McEvoy, G. S. Duesberg, *Solid-State. Electron.* **2016**, *125*, 39.

[141] K. Onomitsu, A. Krajewska, R. A. E. Neufeld, F. Maeda, K. Kumakura, H. Yamamoto, *Appl. Phys. Express* **2016**, *9*, 115501.

[142] M. I. Serna, S. H. Yoo, S. Moreno, Y. Xi, J. P. Oviedo, H. Choi, H. N. Alshareef, M. J. Kim, M. Minary-Jolandan, M. A. Quevedo-Lopez, *ACS Nano* **2016**, *10*, 6054.

[143] C. Muratore, J. J. Hu, B. Wang, M. A. Haque, J. E. Bultman, M. L. Jespersen, P. J. Shamberger, M. E. McConney, R. D. Naguy, A. A. Voevodin, *Appl. Phys. Lett.* **2014**, *104*, 261604.

[144] J. A. Miwa, M. Dendzik, S. S. Grønborg, M. Bianchi, J. V Lauritsen, P. Hofmann, S. Ulstrup, *ACS Nano* **2015**, *9*, 6502.

[145] S. G. Sørensen, H. G. Füchtbauer, A. K. Tuxen, A. S. Walton, J. V. Lauritsen, *ACS Nano* **2014**, *8*, 6788.

[146] H. Bana, E. Travaglia, L. Bignardi, P. Lacovig, C. E. Sanders, M. Dendzik, M. Michiardi, M. Bianchi, D. Lizzit, F. Presel, D. De Angelis, N. Apostol, P. K. Das, J. Fujii, I. Vobornik, R. Larciprete, A. Baraldi, P. Hofmann, S. Lizzit, *2D Mater.* **2018**, *5*, 035012.

[147] S. Wu, C. Huang, G. Aivazian, J. S. Ross, D. H. Cobden, X. Xu, *ACS Nano* **2013**, *7*, 2768.

[148] X. Duan, C. Wang, J. C. Shaw, R. Cheng, Y. Chen, H. Li, X. Wu, Y. Tang, Q. Zhang, A. Pan, J. Jiang, R. Yu, Y. Huang, X. Duan, *Nat. Nanotechnol.* **2014**, *9*, 1024.

[149] J. Zhang, F. Wang, V. B. Shenoy, M. Tang, J. Lou, *Mater. Today*, DOI: 10.1016/j.mattod.2020.06.012.

[150] A. Ambrosi, M. Pumera, *Chem. Soc. Rev.* **2018**, *47*, 7213.

[151] X. Cai, Y. Luo, B. Liu, H.-M. Cheng, *Chem. Soc. Rev.* **2018**, *47*, 6224.

[152] A. K. Geim, I. V Grigorieva, *Nature* **2013**, *499*, 419.

[153] Z. Cai, B. Liu, X. Zou, H.-M. Cheng, *Chem. Rev.* **2018**, *118*, 6091.

[154]   M. Bosi, *RSC Adv.* **2015**, *8*, 75500.

[155]   Q. Ji, Y. Zhang, Y. Zhang, Z. Liu, *Chem. Soc. Rev.* **2015**, *44*, 2587.

[156]   F. Reale, K. Sharda, C. Mattevi, *Appl. Mater. Today* **2016**, *3*, 11.

[157]   S. M. Eichfeld, L. Hossain, Y. Lin, A. F. Piasecki, B. Kupp, A. G. Birdwell, R. A. Burke, N. Lu, X. Peng, J. Li, A. Azcatl, S. McDonnell, R. M. Wallace, M. J. Kim, T. S. Mayer, J. M. Redwing, J. A. Robinson, *ACS Nano* **2015**, *9*, 2080.

[158]   T. Kim, J. Mun, H. Park, D. Joung, M. Diware, C. Won, J. Park, S.-H. Jeong, S.-W. Kang, *Nanotechnology* **2017**, *28*, 18LT01.

[159]   Y. Zhao, J. G. Song, G. H. Ryu, K. Y. Ko, W. J. Woo, Y. Kim, D. Kim, J. H. Lim, S. Lee, Z. Lee, J. Park, H. Kim, *Nanoscale* **2018**, *10*, 9338.

[160]   J. Mun, H. Park, J. Park, D. Joung, S.-K. Lee, J. Leem, J.-M. Myoung, J. Park, S.-H. Jeong, W. Chegal, S. Nam, S.-W. Kang, *ACS Appl. Electron. Mater.* **2019**, *1*, 608.

[161]   J. Cho, H.-R. Fuh, C. Ó. Coileáin, C.-R. Chang, X. Han, D. Zhang, H. Fei, H.-C. Wu, L. Zhang, M. Choi, D. Chen, H.-P. Huang, J. Feng, Y. Chen, H. Xu, *ACS Appl. Mater. Interfaces* **2019**, *11*, 8202.

[162]   Y. Wang, L. Li, W. Yao, S. Song, J. T. Sun, J. Pan, X. Ren, C. Li, E. Okunishi, Y.-Q. Wang, E. Wang, Y. Shao, Y. Y. Zhang, H. Yang, E. F. Schwier, H. Iwasawa, K. Shimada, M. Taniguchi, Z. Cheng, S. Zhou, S. Du, S. J. Pennycook, S. T. Pantelides, H.-J. Gao, *Nano Lett.* **2015**, *15*, 4013.

[163]   X. Duan, C. Wang, A. Pan, R. Yu, X. Duan, *Chem. Soc. Rev.* **2015**, *44*, 8859.

[164]   M. Gao, M. Zhang, W. Niu, Y. Chen, M. Gu, H. Wang, F. Song, P. Wang, S. Yan, F. Wang, X. Wang, X. Wang, Y. Xu, R. Zhang, *Appl. Phys. Lett.* **2017**, *111*, 031906.

[165]   A. Mohammed, H. Nakamura, P. Wochner, S. Ibrahimkutty, A. Schulz, K. Müller, U. Starke, B. Stuhlhofer, G. Cristiani, G. Logvenov, H. Takagi, *Appl. Phys. Lett.* **2017**, *111*, 073101.

[166]   J. Tao, J. Chai, X. Lu, L. M. Wong, T. I. Wong, J. Pan, Q. Xiong, D. Chi, S. Wang, *Nanoscale* **2015**, *7*, 2497.

[167]   J. H. Huang, K. Y. Deng, P. S. Liu, C. T. Wu, C. T. Chou, W. H. Chang, Y. J. Lee, T. H. Hou, *Adv. Mater. Interfaces* **2017**, *4*, 1700157.

[168]   S. Hussain, J. Singh, D. Vikraman, A. K. Singh, M. Z. Iqbal, M. F. Khan, P. Kumar, D. C. Choi, W. Song, K.-S. An, J. Eom, W.-G. Lee, J. Jung, *Sci. Rep.* **2016**, *6*, 30791.

[169]   M. Hamada, K. Matsuura, T. Sakamoto, I. Muneta, T. Hoshii, K. Kakushima, K. Tsutsui, H. Wakabayashi, *IEEE J. Electron Devices Soc.* **2019**, *7*, 1258.

[170]   M. Kumar, D. Y. Park, R. Singh, M. S. Jeong, T. Som, J. Kim, *ACS Appl. Mater. Interfaces* **2019**, *11*, 35845.

[171]   L. A. Walsh, R. Addou, R. M. Wallace, C. L. Hinkle, in *Molecular Beam Epitaxy* (Ed.: M. Henini), Elsevier, Amsterdam, Netherlands, **2018**, Ch. 22.

[172]   S. Vishwanath, P. Dang, H. G. Xing, in *Molecular Beam Epitaxy* (Ed.: M. Henini), Elsevier, Amsterdam, Netherlands, **2018**, Ch. 20.

[173]   E. A. Gulbransen, K. F. Andrew, F. A. Brassart, *J. Electrochem. Soc.* **1963**, *110*, 952.

[174]   M. Mattinen, G. Popov, M. Vehkamäki, P. J. King, K. Mizohata, P. Jalkanen, J. Räisänen, M. Leskelä, M. Ritala, *Chem. Mater.* **2019**, *31*, 5713.

[175]   A. Chang, Y. Mao, Z. Huang, H. Hong, J. Xu, W. Huang, S. Chen, C. Li, *Chinese Phys. B* **2020**, *29*, 038102.

[176]   R. Browning, P. Padigi, R. Solanki, D. J. Tweet, P. Schuele, D. Evans, *Mater. Res. Express* **2015**, *2*, 035006.

[177]   Y. Kim, J.-G. Song, Y. J. Park, G. H. Ryu, S. J. Lee, J. S. Kim, P. J. Jeon, C. W. Lee, W. J. Woo, T. Choi, H. Jung, H.-B.-R. Lee, J.-M. Myoung, S. Im, Z. Lee, J.-H. Ahn, J. Park, H. Kim, *Sci. Rep.* **2016**, *6*, 18754.

[178]   Y. Kim, D. Choi, W. J. Woo, J. B. Lee, G. H. Ryu, J. H. Lim, S. Lee, Z. Lee, S. Im, J.-H. Ahn, W.-H. Kim, J. Park, H. Kim, *Appl. Surf. Sci.* **2019**, *494*, 591.

[179] A. Valdivia, D. J. Tweet, J. F. Conley Jr, *J. Vac. Sci. Technol. A* **2016**, *34*, 021515.

[180] L. Liu, Y. Huang, J. Sha, Y. Chen, *Nanotechnology* **2017**, *28*, 195605.

[181] Y. Huang, L. Liu, W. Zhao, Y. Chen, *Thin Solid Films* **2017**, *624*, 101.

[182] Y. Huang, L. Liu, J. Sha, Y. Chen, *Appl. Phys. Lett.* **2017**, *111*, 063902.

[183] Y. Huang, L. Liu, J. Lv, J. Yang, J. Sha, Y. Chen, *AIP Adv.* **2018**, *8*, 045216.

[184] Y. Huang, L. Liu, J. Yang, Y. Chen, *Langmuir* **2019**, *35*, 3651.

[185] J. Yang, L. Liu, *Appl. Surf. Sci.* **2020**, *502*, 144402.

[186] J. Yang, X. Xu, L. Liu, *Nanotechnology* **2020**, *31*, 395711.

[187] Y. Xing, Z. Wu, J. Yang, X. Wang, L. Liu, *Surf. Coatings Technol.* **2020**, *385*, 125396.

[188] S. Jiao, L. Liu, J. Wang, K. Ma, J. Lv, *Small* **2020**, *16*, 2001223.

[189] L. Liu, K. Ma, X. Xu, C. Shangguan, J. Lv, S. Zhu, S. Jiao, J. Wang, *ACS Appl. Mater. Interfaces* **2020**, *12*, 29074.

[190] Y. Huang, L. Liu, X. Liu, *Nanotechnology* **2019**, *30*, 095402.

[191] T. A. Ho, C. Bae, S. Lee, M. Kim, J. M. Montero-Moreno, J. H. Park, H. Shin, *Chem. Mater.* **2017**, *29*, 7604.

[192] M. B. Sreedhara, S. Gope, B. Vishal, R. Datta, A. J. Bhattacharyya, C. N. R. Rao, *J. Mater. Chem. A* **2018**, *6*, 2302.

[193] J. Joe, C. Bae, E. Kim, T. A. Ho, H. Yang, J. Hyeo, *Catalysts* **2018**, *8*, 580.

[194] M. Alqahtani, S. Sathasivam, F. Cui, L. Steier, X. Xia, C. Blackman, E. Kim, H. Shin, M. Benamara, Y. I. Mazur, G. J. Salamo, I. P. Parkin, H. Liu, J. Wu, *J. Mater. Chem. A* **2019**, *7*, 8550.

[195] T. A. Ho, C. Bae, J. Joe, H. Yang, S. Kim, J. H. Park, H. Shin, *ACS Appl. Mater. Interfaces* **2019**, *11*, 37586.

[196] W. Ahn, H. Lee, Y. Cho, K. Byun, H. Kim, M. Leem, H. Lee, T. Park, E. Lee, H. Shin, H. Kim, *Phys. Status Solidi* **2020**, *217*, 1901042.

[197]   Y. Wang, Z.-H. Gu, H. Liu, L. Chen, X. Liu, L. Min, Z. Li, H. Zhu, Q.-Q. Sun, *ACS Appl. Electron. Mater.* **2019**, *1*, 1418.

[198]   T. Zhang, H. Liu, Y. Wang, H. Zhu, L. Chen, Q. Sun, D. W. Zhang, *Phys. Status Solidi RRL* **2019**, *13*, 1900018.

[199]   D. Zhao, Z. Tian, H. Liu, Z. Gu, H. Zhu, L. Chen, Q. Sun, D. W. Zhang, *ACS Appl. Mater. Interfaces* **2020**, *12*, 14308.

[200]   Y. Wang, T. Chen, T. Zhang, H. Zhu, L. Chen, Q. Sun, D. W. Zhang, *J. Mater. Sci. Mater. Electron.* **2019**, *30*, 4085.

[201]   Z. Tian, D. Zhao, H. Liu, H. Zhu, L. Chen, Q. Sun, D. W. Zhang, *ACS Appl. Nano Mater.* **2019**, *2*, 7810.

[202]   H. Liu, L. Chen, H. Zhu, Q. Sun, S. Ding, P. Zhou, D. W. Zhang, *Nano Res.* **2020**, *13*, 1644.

[203]   A. U. Mane, S. Letourneau, D. J. Mandia, J. A. Libera, Y. Lei, Q. Peng, E. Graugnard, J. W. Elam, *J. Vac. Sci. Technol. A* **2018**, *36*, 01A125.

[204]   S. Letourneau, M. J. Young, N. M. Bedford, Y. Ren, A. Yanguas-Gil, A. U. Mane, J. W. Elam, E. Graugnard, *ACS Appl. Nano Mater.* **2018**, *1*, 4028.

[205]   D. K. Nandi, U. K. Sen, D. Choudhury, S. Mitra, S. K. Sarkar, *Electrochim. Acta* **2014**, *146*, 706.

[206]   J. J. Pyeon, S. H. Kim, D. S. Jeong, S.-H. Baek, C.-Y. Kang, J.-S. Kim, S. K. Kim, *Nanoscale* **2016**, *8*, 10792.

[207]   D. Xiong, Q. Zhang, W. Li, J. Li, X. Fu, M. F. Cerqueira, P. Alpuim, L. Liu, *Nanoscale* **2017**, *9*, 2711.

[208]   Y. Jang, S. Yeo, H.-B.-R. Lee, H. Kim, S.-H. Kim, *Appl. Surf. Sci.* **2016**, *365*, 160.

[209]   D. K. Nandi, S. Sahoo, S. Sinha, S. Yeo, H. Kim, R. N. Bulakhe, J. Heo, J.-J. Shim, S.-H. Kim, *ACS Appl. Mater. Interfaces* **2017**, *9*, 40252.

[210]   S. Oh, J. B. Kim, J. T. Song, J. Oh, S.-H. Kim, *J. Mater. Chem. A* **2017**, *5*, 3304.

[211]   C. MacIsaac, J. R. Schneider, R. G. Closser, T. R. Hellstern, D. S. Bergsman, J. Park, Y. Liu, R. Sinclair, S. F. Bent, *Adv. Funct. Mater.* **2018**, *28*, 1800852.

[212]   Z. Jin, S. Shin, D. H. Kwon, S.-J. Han, Y.-S. Min, *Nanoscale* **2014**, *6*, 14453.

[213]   S. Shin, Z. Jin, D. H. Kwon, R. Bose, Y.-S. Min, *Langmuir* **2015**, *31*, 1196.

[214]   D. H. Kwon, Z. Jin, S. Shin, W.-S. Lee, Y.-S. Min, *Nanoscale* **2016**, *8*, 7180.

[215]   X. Li, M. Puttaswamy, Z. Wang, C. K. Tan, A. C. Grimsdale, N. P. Kherani, A. I. Y. Tok, *Appl. Surf. Sci.* **2017**, *422*, 536.

[216]   M. Song, H. Tan, X. Li, A. I. Y. Tok, P. Liang, D. Chao, H. J. Fan, *Small Methods* **2019**, *4*, 1900274.

[217]   T. Jeong, S.-Y. Ham, B. Koo, P. Lee, Y.-S. Min, J.-Y. Kim, M. J. Ko, *J. Ind. Eng. Chem.* **2019**, *80*, 106.

[218]   T. Zhang, Y. Wang, J. Xu, L. Chen, H. Zhu, Q. Sun, S. Ding, D. W. Zhang, *2D Mater.* **2018**, *5*, 015028.

[219]   H. Sopha, A. T. Tesfaye, R. Zazpe, J. Michalicka, F. Dvorak, L. Hromadko, M. Krbal, J. Prikryl, T. Djenizian, J. M. Macak, *FlatChem* **2019**, *17*, 100130.

[220]   M. Motola, M. Baudys, R. Zazpe, M. Krbal, J. Michalicka, J. Rodriguez-Pereira, D. Pavlinak, J. Prikryl, L. Hromadko, H. Sopha, J. Krysa, J. M. Macak, *Nanoscale* **2019**, *11*, 23126.

[221]   A. T. Tesfaye, H. Sopha, A. Ayobi, R. Zazpe, J. Rodriguez-Pereira, J. Michalicka, L. Hromadko, S. Ng, Z. Spoz, J. Prikryl, J. M. Macak, T. Djenizian, *Nanomaterials* **2020**, *10*, 953.

[222]   A. Sharma, *PhD Thesis*, Eindhoven University of Technology, The Netherlands, December, **2018**. Available at https://tue-staging.elsevierpure.com/en/publications/atomic-layer-deposition-for-2-d-materials-beyond-graphene

[223]   L. Wu, A. Longo, N. Y. Dzade, A. Sharma, M. M. R. M. Hendrix, A. A. Bol, N. H. de Leeuw, E. J. M. Hensen, J. P. Hofmann, *ChemSusChem* **2019**, *12*, 4383.

[224]   V. Vandalon, B. Schrode, A. Sharma, A. Perrotta, B. Schrode, M. A. Verheijen, A. A. Bol, *Nanoscale* **2019**, *11*, 22860.

[225]   B. Kalanyan, R. Beams, M. B. Katz, A. V. Davydov, J. E. Maslar, R. K. Kanjolia, *J. Vac. Sci. Technol. A* **2019**, *37*, 010901.

[226]   T. Jurca, M. J. Moody, A. Henning, J. D. Emery, B. Wang, J. M. Tan, T. L. Lohr, L. J. Lauhon, T. J. Marks, *Angew. Chem. - Int. Ed.* **2017**, *56*, 4991.

[227]   Y. Cao, Y. Wu, C. Badie, S. Cadot, C. Camp, E. A. Quadrelli, J. Bachmann, *ACS Omega* **2019**, *4*, 8816.

[228]   J. Teich, R. Dvir, A. Henning, E. R. Hamo, M. J. Moody, T. Jurca, H. Cohen, T. J. Marks, B. A. Rosen, L. J. Jauhon, A. Ismach, *Nanoscale* **2020**, *12*, 2715.

[229]   S. Cadot, O. Renault, M. Frégnaux, D. Rouchon, E. Nolot, K. Szeto, C. Thieuleux, L. Veyre, H. Okuno, F. Martin, E. A. Quadrelli, *Nanoscale* **2017**, *9*, 538.

[230]   M. Krbal, J. Prikryl, R. Zazpe, F. Dvorak, F. Bures, J. M. Macak, *Phys. Status Solidi RRL* **2018**, *12*, 1800023.

[231]   S. Ng, M. Krbal, R. Zazpe, J. Prikryl, J. Charvot, F. Dvořák, L. Strizik, S. Slang, H. Sopha, Y. Kosto, V. Matolin, F. K. Yam, F. Bures, J. M. Macak, *Adv. Mater. Interfaces* **2018**, *5*, 1701146.

[232]   R. Zazpe, J. Charvot, R. Krumpolec, L. Hromadko, F. Dvorak, P. Knotek, J. Michalicka, J. Prikryl, V. Jelínková, F. Bureš, J. M. Macak, *FlatChem* **2020**, *21*, 100166.

[233]   J. Charvot, D. Pokorný, R. Zazpe, R. Krumpolec, D. Pavliňák, L. Hromádko, J. Přikryl, J. Rodriguez-Pereira, M. Klikar, V. Jelínková, J. M. Macak, F. Bures, *ChemPlusChem* **2020**, 576.

[234]   J. Hämäläinen, M. Mattinen, K. Mizohata, K. Meinander, M. Vehkamäki, J. Räisänen, M. Ritala, M. Leskelä, *Adv. Mater.* **2018**, *30*, 1703622.

[235]   J. Lv, L. Liu, *Nanotechnology* **2020**, *31*, 055602.

[236]   E. Thimsen, S. C. Riha, S. V Baryshev, A. B. F. Martinson, J. W. Elam, M. J. Pellin, *Chem. Mater.* **2012**, *24*, 3188.

[237]   E. Thimsen, S. V. Baryshev, A. B. F. Martinson, J. W. Elam, I. V. Veryovkin, M. J. Pellin, *Chem. Mater.* **2013**, *25*, 313.

[238]   G. Ham, S. Shin, J. Park, H. Choi, J. Kim, Y.-A. Lee, H. Seo, H. Jeon, *ACS Appl. Mater. Interfaces* **2013**, *5*, 8889.

[239]   W. Seo, S. Shin, G. Ham, J. Lee, S. Lee, H. Choi, H. Jeon, *Jpn. J. Appl. Phys.* **2017**, *56*, 031201.

[240]   S. Lee, S. Shin, G. Ham, J. Lee, H. Choi, H. Park, H. Jeon, *AIP Adv.* **2017**, *7*, 045307.

[241]   J. Lee, J. Lee, G. Ham, S. Shin, J. Park, H. Choi, S. Lee, J. Kim, O. Sul, S. Lee, H. Jeon, *AIP Adv.* **2017**, *7*, 025311.

[242]   N. Lee, G. Lee, H. Choi, H. Park, Y. Choi, H. Seo, H. Ju, S. Kim, O. Sul, J. Lee, S.-B. Lee, H. Jeon, *Nanotechnology* **2019**, *30*, 405707.

[243]   N. Lee, G. Lee, H. Choi, H. Park, Y. Choi, K. Kim, Y. Choi, J.-W. Kim, H. Yuk, O. Sul, S.-B. Lee, H. Jeon, *Appl. Surf. Sci.* **2019**, *496*, 143689.

[244]   N. Lee, H. Choi, H. Parj, Y. Choi, H. Yuk, J. Lee, H. Jeon, *Nanotechnology* **2020**, *31*, 265604.

[245]   S. Kim, J. H. Bang, M. S. Choi, W. Oum, A. Mirzaei, N. Lee, H.-C. Kwon, D. Lee, H. Jeong, S. S. Kim, H. W. Kim, *Met. Mater. Int.* **2019**, *25*, 805.

[246]   N. Lee, H. Choi, H. Park, Y. Choi, H. Yuk, J. Lee, S. G. Lee, E. G. Lee, H. Jeon, *Nanotechnology* **2020**, *31*, 355702.

[247]   W. Hu, N. D. Quang, S. Majumder, E. Park, D. Kim, H. S. Choi, H. S. Chang, *J. Alloys Compd.* **2020**, *819*, 153349.

[248]   C. Hägglund, G. Zeltzer, R. Ruiz, I. Thomann, H.-B.-R. Lee, M. L. Brongersma, S. F. Bent, *Nano Lett.* **2013**, *13*, 3352.

[249]   W. Hu, T. T. Hien, D. Kim, H. S. Chang, *Nanomaterials* **2019**, *9*, 1083.

[250]   M. Z. Ansari, N. Parveen, D. K. Nandi, R. Ramesh, S. A. Ansari, T. Cheon, S.-H. Kim, *Sci. Rep.* **2019**, *9*, 10225.

[251]   J. J. Pyeon, I. Baek, W. C. Lee, H. Lee, S. O. Won, G. Lee, T. Chung, J. H. Han, S. Baek, J. Kim, J. Choi, C. Kang, S. K. Kim, *ACS Appl. Mater. Interfaces* **2020**, *12*, 2679.

[252]   J. J. Pyeon, I.-H. Baek, Y. G. Song, G. S. Kim, A. Cho, G. Lee, J. H. Han, T. Chung, C. S. Hwang, C. Kang, S. K. Kim, *J. Mater. Chem. C* **2020**, *8*, 11874.

[253]   V. Pore, M. Ritala, M. Leskelä, *Chem. Vap. Depos.* **2007**, *13*, 163.

[254]   N. Mahuli, S. K. Sarkar, *J. Vac. Sci. Technol. A* **2015**, *33*, 01A150.

[255]   F. N. Sayed, M. B. Sreedhara, A. Soni, U. Bhat, R. Datta, A. J. Bhattacharyya, C. N. R. Rao, *Mater. Res. Express* **2019**, *6*, 115549.

[256]   H. Nam, H. Yang, E. Kim, C. Bae, H. Shin, *J. Vac. Sci. Technol. A* **2019**, *37*, 020916.

[257]   S. B. Basuvalingam, Y. Zhang, M. A. Bloodgood, R. H. Godiksen, A. G. Curto, J. P. Hofmann, M. A. Verheijen, W. M. M. Kessels, A. A. Bol, *Chem. Mater.* **2019**, *31*, 9354.

[258]   R. Browning, P. Plachinda, P. Padigi, R. Solanki, S. Rouvimov, *Nanoscale* **2015**, *8*, 2143.

[259]   T. W. Scharf, S. V. Prasad, M. T. Dugger, P. G. Kotula, R. S. Goeke, R. K. Grubbs, *Acta Mater.* **2006**, *54*, 4731.

[260]   T. W. Scharf, D. R. Diercks, B. P. Gorman, S. V. Prasad, M. T. Dugger, *Tribol. Trans.* **2009**, *52*, 284.

[261]   A. Delabie, M. Caymax, B. Groven, M. Heyne, K. Haesevoets, J. Meersschaut, T. Nuytten, H. Bender, T. Conard, P. Verdonck, S. van Elshocht, S. de Gendt, M. Heyns, K. Barla, I. Radu, A. Thean, *Chem. Commun.* **2015**, *51*, 15692.

[262]   T. Schram, Q. Smets, B. Groven, M. H. Heyne, E. Kunnen, A. Thiam, K. Devriendt, A. Delabie, D. Lin, D. Chiappe, I. Asselberghs, S. Brus, C. Huyghebaert, S. Sayan, A. Juncker, M. Caymax, I. P. Radu, in *Proceedings of the 47th European Conference on Solid-State Device Research*, **2017**, pp. 212–215.

[263] D. K. Nandi, U. K. Sen, A. Dhara, S. Mitra, S. K. Sarkar, *RSC Adv.* **2016**, *6*, 38024.

[264] M. Shi, J. Xu, Y. Dai, Q. Cao, L. Chen, Q. Sun, P. Zhou, in *Proceedings of the 13th IEEE International. Conference on Solid-State and Integrated Circuit Technology (ICSICT),* **2016**, pp. 6–8.

[265] Y. Sun, Z. Chai, X. Lu, J. Lu, *Tribol. Int.* **2017**, *114*, 478.

[266] S. Yeo, D. K. Nandi, R. Rahul, T. H. Kim, B. Shong, Y. Jang, J.-S. Bae, J. W. Han, S.-H. Kim, H. Kim, *Appl. Surf. Sci.* **2018**, *459*, 596.

[267] D. K. Nandi, S. Yeo, M. Zahid, S. Sinha, T. Cheon, J. Kwon, H. Kim, J. Heo, T. Song, S. Kim, *Electrochim. Acta* **2019**, *322*, 134766.

[268] Y. Wu, M. H. Raza, Y.-C. Chen, P. Amsalem, S. Wahl, K. Skrodczky, X. Xu, K. S. Lokare, M. Zhukush, P. Gaval, N. Koch, E. A. Quadrelli, N. Pinna, *Chem. Mater.* **2019**, *31*, 1881.

[269] S. Balasubramanyam, M. Shirazi, M. A. Bloodgood, L. Wu, M. A. Verheijen, V. Vandalon, W. M. M. Kessels, J. P. Hofmann, A. A. Bol, *Chem. Mater.* **2019**, *31*, 5104.

[270] R. Browning, N. Kuperman, R. Solanki, V. Kanzyuba, S. Rouvimov, *Semicond. Sci. Technol.* **2016**, *31*, 095002.

[271] R. Browning, P. Plachinda, R. Solanki, *Semicond. Sci. Technol.* **2018**, *33*, 105005.

[272] K. Park, Y. Kim, J.-G. Song, S. J. Kim, C. W. Lee, G. H. Ryu, Z. Lee, J. Park, H. Kim, *2D Mater.* **2016**, *3*, 014004.

[273] K. Y. Ko, K. Park, S. Lee, Y. Kim, W. J. Woo, D. Kim, J.-G. Song, J. Park, H. Kim, *ACS Appl. Mater. Interfaces* **2018**, *10*, 23910.

[274] M. S. Diware, S. P. Ganorkar, K. Park, W. Chegal, H. M. Cho, Y. J. Cho, Y. D. Kim, H. Kim, *J. Phys. Condens. Matter* **2018**, *30*, 235701.

[275] H. Wang, Z. Lu, S. Xu, D. Kong, J. J. Cha, G. Zheng, P.-C. Hsu, K. Yan, D. Bradshaw, F. B. Prinz, Y. Cui, *Proc. Natl. Acad. Sci. U. S. A.* **2013**, *110*, 19701.

[276]   C. Martella, P. Melloni, E. Cinquanta, E. Cianci, M. Alia, M. Longo, A. Lamperti, S. Vangelista, M. Fanciulli, A. Molle, *Adv. Electron. Mater.* **2016**, 1600330.

[277]   C. Martella, L. Ortolani, E. Cianci, A. Lamperti, V. Morandi, A. Molle, *Nano Res.* **2019**, *12*, 1851.

[278]   J.-G. Song, G. H. Ryu, S. J. Lee, S. Sim, C. W. Lee, T. Choi, H. Jung, Y. Kim, Z. Lee, J.-M. Myoung, C. Dussarrat, C. Lansalot-Matras, J. Park, H. Choi, H. Kim, *Nat. Commun.* **2015**, *6*, 7817.

[279]   I.-K. Oh, W.-H. Kim, L. Zeng, J. Singh, D. Bae, A. J. M. Mackus, J.-G. Song, S. Seo, B. Shong, H. Kim, S. F. Bent, *ACS Nano* **2020**, *14*, 1757.

[280]   R. Romanov, M. Kozodaev, D. Myakota, A. Chernikova, S. Novikov, V. Volkov, A. Slavich, S. Zarubin, P. S. Chizhov, R. R. Khakimov, A. A. Chouprik, C. S. Hwang, A. M. Markeev, *ACS Appl. Nano Mater.* **2019**, *2*, 7521.

[281]   M.-L. Shi, L. Chen, T.-B. Zhang, J. Xu, H. Zhu, Q.-Q. Sun, D. W. Zhang, *Small* **2017**, *35*, 1603157.

[282]   T. Chen, Y. Wang, T. Zhang, H. Zhu, L. Chen, Q. Sun, *J. Mater. Sci. Mater. Electron.* **2020**, *31*, 5485.

[283]   T. R. Hellstern, D. W. Palm, J. Carter, A. Deangelis, K. Horsley, L. Weinhardt, W. Yang, M. Blum, N. Gaillard, C. Heske, T. F. Jaramillo, *ACS Appl. Energy Mater.* **2019**, *2*, 1060.

[284]   B. D. Keller, A. Bertuch, J. Provine, G. Sundaram, N. Ferralis, J. C. Grossman, *Chem. Mater.* **2017**, *29*, 2024.

[285]   T.-J. Dai, X.-D. Fan, Y.-X. Ren, S. Hou, Y.-Y. Zhang, L.-X. Qian, Y.-R. Li, X.-Z. Liu, *J. Mater. Sci.* **2018**, *53*, 8436.

[286]   T. Dai, Y. Liu, X. Liu, D. Xie, Y. Li, *J. Alloys Compd.* **2019**, *785*, 951.

[287]   T. Dai, Y. Liu, X. Fan, X. Liu, D. Xie, Y. Li, *Nanophotonics* **2018**, *7*, 1959.

[288]   J. J. Pyeon, I.-H. Baek, W. C. Lim, K. H. Chae, S. H. Han, G. Y. Lee, S.-H. Baek, J.-S. Kim, J.-W. Choi, T.-M. Chung, J. H. Han, C.-Y. Kang, S. K. Kim, *Nanoscale* **2018**, *10*, 17712.

[289]   H. Choi, J. Lee, S. Shin, J. Lee, S. Lee, H. Park, S. Kwon, N. Lee, M. Bang, S.-B. Lee, H. Jeon, *Nanotechnology* **2018**, *29*, 215201.

[290]   X. Zang, C. Shen, E. Kao, R. Warren, R. Zhang, K. S. Teh, J. Zhong, M. Wei, B. Li, Y. Chu, M. Sanghadasa, A. Schwartzberg, L. Lin, *Adv. Mater.* **2017**, *30*, 1704754.

[291]   J.-G. Song, J. Park, W. Lee, T. Choi, H. Jung, C. W. Lee, S.-H. Hwang, J. M. Myoung, J.-H. Jung, S.-H. Kim, C. Lansalot-Matras, H. Kim, *ACS Nano* **2013**, *7*, 11333.

[292]   K. Y. Ko, J.-G. Song, Y. Kim, T. Choi, S. Shin, C. W. Lee, K. Lee, J. Koo, H. Lee, J. Kim, T. Lee, J. Park, H. Kim, *ACS Nano* **2016**, *10*, 9287.

[293]   N. Li, L. Feng, J. Su, W. Zeng, Z. Liu, *RSC Adv.* **2016**, *6*, 64879.

[294]   W. Zeng, L.-P. Feng, J. Su, H.-X. Pan, Z.-T. Liu, *J. Alloys Compd.* **2018**, *745*, 834.

[295]   C. Chen, J. Pedrini, E. A. Gaulding, C. Kastl, G. Calafiore, S. D. Dhuey, T. Kuykendall, S. Cabrini, F. M. Toma, S. Aloni, A. Schwartzberg, *Sci. Rep.* **2018**, *9*, 2768.

[296]   D. Akinwande, C. Huyghebaert, C. H. Wang, M. I. Serna, S. Goossens, L. J. Li, H. S. P. Wong, F. H. L. Koppens, *Nature* **2019**, *573*, 507.

[297]   J. Yao, G. Yang, *J. Appl. Phys.* **2020**, *127*, 030902.

[298]   G. W. Shim, W. Hong, J. Cha, J. H. Park, K. J. Lee, S.-Y. Choi, *Adv. Mater.* **2020**, *32*, 1907166.

[299]   W. A. MacDonald, M. K. Looney, D. MacKerron, R. Eveson, R. Adam, K. Hashimoto, K. Rakos, *J. Soc. Inf. Disp.* **2015**, *15*, 1075.

[300]   H. Kum, D. Lee, W. Kong, H. Kim, Y. Park, Y. Kim, Y. Baek, S. H. Bae, K. Lee, J. Kim, *Nat. Electron.* **2019**, *2*, 439.

[301]   S. Fan, Q. A. Vu, M. D. Tran, S. Adhikari, Y. H. Lee, *2D Mater.* **2020,** *7*, 022005.

[302]   F. Schwierz, J. Pezoldt, R. Granzner, *Nanoscale* **2015**, *7*, 8261.

[303]   Y. Liu, X. Duan, Y. Huang, X. Duan, *Chem. Soc. Rev.* **2018**, *47*, 6388.

[304]   X. Jing, Y. Illarionov, E. Yalon, P. Zhou, T. Grasser, Y. Shi, M. Lanza, *Adv. Funct. Mater.* **2019**, *30,* 1901971.

[305]   S. Thiele, W. Kinberger, R. Granzner, G. Fiori, F. Schwierz, *Solid State Electron.* **2018**, *143*, 2.

[306]   B. Liu, A. Abbas, C. Zhou, *Adv. Electron. Mater.* **2017**, *3*, 1700045.

[307]   V. K. Sangwan, M. C. Hersam, *Annu. Rev. Phys. Chem.* **2018**, *69*, 299.

[308]   H. Schmidt, F. Giustiniano, G. Eda, *Chem. Soc. Rev.* **2015**, *44*, 7715.

[309]   Y. Xu, C. Cheng, S. Du, J. Yang, B. Yu, J. Luo, W. Yin, E. Li, S. Dong, P. Ye, X. Duan, *ACS Nano* **2016**, *10*, 4895.

[310]   B. Radisavljevic, A. Kis, *Nat. Mater.* **2013**, *12*, 815.

[311]   J. Y. Shang, M. J. Moody, J. Chen, S. Krylyuk, A. V Davydov, T. J. Marks, L. J. Lauhon, *ACS Appl. Electron. Mater.* **2020**, *2*, 1273.

[312]   K. H. Gu, H.-B.-R. Lee, *Chem. Mater.* **2017**, *29*, 3809**.**

[313]   T. Nam, S. Seo, H. Kim, *J. Vac. Sci. Technol. A* **2020**, *38*, 030803.

[314]   Z. Dai, Z. Wang, X. He, X.-X. Zhang, H. N. Alshareef, *Adv. Funct. Mater.* **2017**, *27*, 1703119.

[315]   Y. Huang, E. Sutter, J. T. Sadowski, M. Cotlet, O. L. A. Monti, D. A. Racke, M. R. Neupane, D. Wickramaratne, R. K. Lake, B. A. Parkinson, P. Sutter, *ACS Nano* **2014**, *8*, 10743.

[316]   I.-H. Baek, J. J. Pyeon, G.-Y. Lee, Y. G. Song, H. Lee, S. O. Won, J. H. Han, C.-Y. Kang, T.-M. Chung, C. S. Hwang, S. K. Kim, *Chem. Mater.* **2020**, *32*, 2313.

[317]   B. Jang, S. Yeo, H. Kim, B. Shin, S.-H. Kim, *J. Vac. Sci. Technol. A* **2017**, *35*, 031506.

[318]   X. Liu, J. Hu, C. Yue, N. Della Fera, Y. Ling, Z. Mao, J. Wei, *ACS Nano* **2014**, *8*, 10396.

[319]   F. Reale, P. Palczynski, I. Amit, G. F. Jones, J. D. Mehew, A. Bacon, N. Ni, P. C. Sherrell, S. Agnoli, M. F. Craciun, S. Russo, C. Mattevi, *Sci. Rep.* **2017**, *7*, 14911.

[320]   N. R. Pradhan, D. Rhodes, S. Memaran, J. M. Poumirol, D. Smirnov, S. Talapatra, S. Feng, N. Perea-Lopez, A. L. Elias, M. Terrones, P. M. Ajayan, L. Balicas, *Sci. Rep.* **2015**, *5*, 8979.

[321]   N. Huo, G. Konstantatos, *Adv. Mater.* **2018**, *30*, 1801134.

[322]   C. Xie, C. Mak, X. Tao, F. Yan, *Adv. Funct. Mater.* **2017**, *27*, 1603886.

[323]   H. Fang, W. Hu, *Adv. Sci.* **2017**, *4*, 1700323.

[324]   K. Thakar, B. Mukherjee, S. Grover, N. Kaushik, M. Deshmukh, S. Lodha, *ACS Appl. Mater. Interfaces* **2018**, *10*, 36512.

[325]   F. Wang, Z. Wang, L. Yin, R. Cheng, J. Wang, Y. Wen, T. A. Shifa, F. Wang, Y. Zhang, X. Zhan, J. He, *Chem. Soc. Rev.* **2018**, *47*, 6296.

[326]   S. Kumar, V. Pavelyev, P. Mishra, N. Tripathi, P. Sharma, F. Calle, *Mater. Sci. Semicond. Process.* **2020**, *107*, 104865.

[327]   S.-J. Choi, I.-D. Kim, *Electron. Mater. Lett.* **2018**, *14*, 221.

[328]   S. Barua, H. S. Dutta, S. Gogoi, R. Devi, R. Khan, *ACS Appl. Nano Mater.* **2018**, *1*, 2.

[329]   K. Kalantar-zadeh, J. Z. Ou, *ACS Sensors* **2015**, *1*, 5.

[330]   B. You, Y. Sun, *Acc. Chem. Res.* **2018**, *51*, 1571.

[331]   C. G. Morales-Guio, L.-A. Stern, X. Hu, *Chem. Soc. Rev.* **2014**, *43*, 6555.

[332]   L. Lin, P. Sherrell, Y. Liu, W. Lei, S. Zhang, H. Zhang, G. G. Wallace, J. Chen, *Adv. Energy Mater.* **2020**, *10*, 1903870.

[333]   P. C. K. Vesborg, B. Seger, I. Chorkendorff, *J. Phys. Chem. Lett.* **2015**, *6*, 951.

[334]   Y. P. Zhu, C. Guo, Y. Zheng, S. Z. Qiao, *Acc. Chem. Res.* **2017**, *50*, 915.

[335]   Hydrogen production, Office of Energy Efficiency and Renewable Energy, U.S. Department of Energy, https://www.energy.gov/eere/fuelcells/hydrogen-production, accessed: May, 2020.

[336]   J. D. Benck, T. R. Hellstern, J. Kibsgaard, P. Chakthranont, T. F. Jaramillo, *ACS Catal.* **2014**, *4*, 3957.

[337]   L. Yang, P. Liu, J. Li, B. Xiang, *Catalysts* **2017**, *7*, 285.

[338]   T. F. Jaramillo, K. P. Jørgensen, J. Bonde, J. H. Nielsen, S. Horch, I. Chorkendorff, *Science* **2007**, *317*, 100.

[339]   A. Eftekhari, *Int. J. Hydrogen Energy* **2017**, *42*, 11053.

[340]   Y. Huan, J. Shi, G. Zhao, X. Yan, Y. Zhang, *Energy Technol.* **2019**, *7*, 1801025.

[341]   Y. Liu, J. Wu, K. P. Hackenberg, J. Zhang, Y. M. Wang, Y. Yang, K. Keyshar, J. Gu, T. Ogitsu, R. Vajtai, J. Lou, P. M. Ajayan, B. C. Wood, B. I. Yakobson, *Nat. Energy* **2017**, *2*, 17127.

[342]   J. Shi, X. Wang, S. Zhang, L. Xiao, Y. Huan, Y. Gong, Z. Zhang, Y. Li, X. Zhou, M. Hong, Q. Fang, Q. Zhang, X. Liu, L. Gu, Z. Liu, Y. Zhang, *Nat. Commun.* **2017**, *8*, 958.

[343]   D. Merki, X. Hu, *Energy Environ. Sci.* **2011**, *4*, 3878.

[344]   J. D. Wiensch, J. John, J. M. Velazquez, D. A. Torelli, A. P. Pieterick, M. T. McDowell, K. Sun, X. Zhao, B. S. Brunschwig, N. S. Lewis, *ACS Energy Lett.* **2017**, *2*, 2234.

[345]   J. Zhang, L. Zhao, A. Liu, X. Li, H. Wu, C. Lu, *Electrochim. Acta* **2015**, *182*, 652.

[346]   M. A. Lukowski, A. S. Daniel, F. Meng, A. Forticaux, L. Li, S. Jin, *J. Am. Chem. Soc.* **2013**, *135*, 10274.

[347]   D. J. Li, U. N. Maiti, J. Lim, D. S. Choi, W. J. Lee, Y. Oh, G. Y. Lee, S. O. Kim, *Nano Lett.* **2014**, *14*, 1228.

[348]   B. Li, L. Jiang, X. Li, Z. Cheng, P. Ran, P. Zuo, L. Qu, J. Zhang, Y. Lu, *Adv. Funct. Mater.* **2019**, *29*, 1806229.

[349]   F. Xi, P. Bogdanoff, K. Harbauer, P. Plate, C. Höhn, J. Rappich, B. Wang, X. Han, R. van de Krol, S. Fiechter, *ACS Catal.* **2019**, *9*, 2368.

[350]   Y. Jiao, Y. Zheng, M. Jaroniec, S. Z. Qiao, *Chem. Soc. Rev.* **2015**, *44*, 2060.

[351]   M. G. Walter, E. L. Warren, J. R. McKone, S. W. Boettcher, Q. Mi, E. A. Santori, N. S. Lewis, *Chem. Rev.* **2010**, *110*, 6446.

[352]   Z. Chen, H. N. Dinh, E. Miller, Eds., *Photoelectrochemical Water Splitting: Standards, Experimental Methods, and Protocols*, Springer, New York, USA, **2013**.

[353]   J. B. Goodenough, K. S. Park, *J. Am. Chem. Soc.* **2013**, *135*, 1167.

[354]   M. Winter, B. Barnett, K. Xu, *Chem. Rev.* **2018**, *118*, 11433.

[355]   J. Liu, H. Zhu, M. H. A. Shiraz, *Front. Energy Res.* **2018**, *6*, 10.

[356]   M. V. Reddy, G. V. Subba Rao, B. V. R. Chowdari, *Chem. Rev.* **2013**, *113*, 5364.

[357]   X. Wang, Q. Weng, Y. Yang, Y. Bando, D. Golberg, *Chem. Soc. Rev.* **2016**, *45*, 4042.

[358]   H. Kang, Y. Liu, K. Cao, Y. Zhao, L. Jiao, Y. Wang, H. Yuan, *J. Mater. Chem. A* **2015**, *3*, 17899.

[359]   T. Stephenson, Z. Li, B. Olsen, D. Mitlin, *Energy Environ. Sci.* **2014**, *7*, 209.

[360]   C. Julien, A. Mauger, A. Vijh, K. Zaghib, in *Lithium Batteries: Science and Technol*ogy, Springer International, Cham, Switzerland, **2016**, Ch. 10.

[361]   S. Wu, Y. Du, S. Sun, *Chem. Eng. J.* **2017**, *307*, 189.

[362]   H. C. M. Knoops, M. E. Donders, M. C. M. van de Sanden, P. H. L. Notten, W. M. M. Kessels, *J. Vac. Sci. Technol. A* **2012**, *30*, 010801.

[363]   M. Mäntymäki, M. Ritala, M. Leskelä, *Coatings* **2018**, *8*, 277.

[364]   W. J. Kwak, Rosy, D. Sharon, C. Xia, H. Kim, L. R. Johnson, P. G. Bruce, L. F. Nazar, Y. K. Sun, A. A. Frimer, M. Noked, S. A. Freunberger, D. Aurbach, *Chem. Rev.* **2020**, *120*, 6626.

[365]   M. Winter, R. J. Brodd, *Chem. Rev.* **2004**, *104*, 4245.

[366]   S. Yuan, S.-Y. Pang, J. Hao, *Appl. Phys. Rev.* **2020**, *7*, 021304.

[367]   Y. Sun, Z. Chai, X. Lu, D. He, *Sci. China Technol. Ser.* **2016**, *60*, 51.

[368]   M. Bernardi, M. Palummo, J. C. Grossman, *Nano Lett.* **2013**, *13*, 3664.

Miika Mattinen is currently a postdoctoral research in University of Helsinki, moving to a postdoctoral position in Eindhoven University of Technology in the beginning of 2021. He obtained his BSc in Chemistry in 2013 and MSc (2015) and PhD (2020) degrees in Inorganic chemistry from University of Helsinki under supervision of professors Mikko Ritala and Markku Leskelä. His doctoral thesis focused on atomic layer deposition of two-dimensional metal dichalcogenide thin films, their characterization, and evaluation for electronic and energy applications. He continues research on ALD 2D materials during his postdoc.

Markku Leskelä, professor emeritus, received both M.Sc. (1974) and PhD (1980) degrees from Helsinki University of Technology. During 1982–1986 he worked at University of Oulu as an associate professor, during 1986–1990 at University of Turku as a professor and during 1990–2018 at University of Helsinki as a professor of inorganic chemistry. Between 2004–2009 he held an Academy professor position. His main research interest focuses on development of chemistry for Atomic Layer Deposition of thin films. His other research topics include metal compound mediated activation of small molecules and luminescent materials.

Mikko Ritala received his M.Sc. degree in 1991 from University of Turku and Ph.D. in 1994 from University of Helsinki, both in inorganic chemistry. During 1995–2003 he worked at University of Helsinki, first as a postdoctoral researcher and then as an academy research fellow, both posts granted by Academy of Finland. In 2003 he was nominated as a professor of

inorganic materials chemistry at University of Helsinki. His main research interest is in Atomic Layer Deposition (ALD) of thin films for microelectronics and other applications. Reaction mechanism studies form an important part of this research.

Atomic layer deposition is one of the most promising methods for producing two-dimensional transition metal dichalcogenides for various applications from electronics to catalysis, energy storage, and beyond. In this review, the potential and challenges of ALD for these applications are systematically evaluated and compared to each other as well as to other deposition methods.

M. Mattinen, M. Leskelä, M. Ritala*

Atomic Layer Deposition of Two-Dimensional Metal Dichalcogenides for Electronics, Catalysis, Energy Storage, and Beyond